Advancing Antimony Selenide Nanostructures for Electrocatalysis, Desalination and Nonlinear Optical Applications

Thesis submitted for the degree of

Doctor of Philosophy (Science)

By

Nabanita Sen

Department of Physics

Jadavpur University

Kolkata -700032

India

February, 2025

CERTIFICATE FROM THE SUPERVISOR

This is to certify that the thesis entitled "Advancing antimony selenide nanostructures for electrocatalysis, desalination and nonlinear optical applications" Submitted by Smt. Nabanita Sen who got her name registered on 22.11.2021 for the award of Ph. D. (Science) Degree of Jadavpur University, is absolutely based upon her own work under the supervision of Prof. Kalyan Kumar Chattopadhyay and that neither this thesis nor any part of it has been submitted for either any degree / diploma or any other academic award anywhere before.

5.2.2025

.....

Dr. K. K. Chattopadhyay
Professor
Department of Physics
Jadavpur University
Kolkata-700 032

.....

(Signature of the Supervisor(s) date with official seal)

Dedicated to my darling Kali, and to my cherished parents, beloved Kalyan Kumar Chattopadhyay and precious Baby. This is also lovingly dedicated to all my dearest pets—Simon, Kuttus, Mini, Jack, Golla, and Kalia—who, though now residing in another realm, remain ever-present in my heart and thoughts.

Acknowledgements

First and foremost, I would like to express my heartfelt gratitude to my home country, my strongest developing India, for its unwavering support, as well as to the government body UGC-CSIR for providing me with the opportunity and financial assistance throughout my five-year research journey. India, I will never forget the contributions you've made to my journey, and I promise to give my best in the future as a researcher, striving to make you even brighter and more prosperous. I am deeply grateful to the Department of Physics and the department of Nanoscience at Jadavpur University for providing me with excellent research facilities and a supportive, conducive research environment since I joined the research centre.

I would like to express my sincere respect, deep appreciation, and heartfelt thanks to my PhD supervisor, Professor Kalyan Kumar Chattopadhyay, for granting me the freedom to pursue my research. His invaluable guidance and insightful discussions have consistently provided me with new perspectives to address challenges in my research. He has offered immense academic support and presented numerous wonderful opportunities throughout my journey. I distinctly remember the day when I first met him, and he was initially reluctant to take me on as a researcher under his guidance because of my worst interview. However, despite this, he eventually gave me the opportunity to join his lab as a junior researcher, and for that, I am truly grateful. Thank you for believing in me and this opportunity.

I would like to express my particular gratitude to Professor Sourav Sarkar for being my well-wisher and rendering continuous support during my thesis work.

I am deeply grateful to my seniors – Nirmalya da, Biswajit da, Supratim da, Diptonil da, Anup da, Madhupriya di, Shrabani di, Dimitra di, Bikram da, Subhasis da, Dipanwita di, Rituparna di, Rimpa di, Sayantani di, and Suvra di – for their unwavering support, kindness, and guidance.

I would like to extend my gratitude to my lab-mates Arnab, Anibrata, Pulak Das, and Souvik Bhattacharya, and my juniors Manas Thakur, Md Najes Riaz, Ritadhwaj,

Amrita, Arnab, Kaustav, Sagnik, Arpan, and Ankita for their help and encouragement throughout the course of our work.

I also thank my lovely sisters and brothers Hati (Sudipta Sen), Hia (Jayeta Sen), Sourav Sen, Suvojit Swar, Jaya Swar, Poppy, Tithi, and Puchi for their unconditional support at home, and my travel partners Mama Bholanath Swar and Mami Mnra Rani Guha.

Nabanita Sen

List of publications related to thesis work

1. Sen, Nabanita, Arnab Das, Supratim Maity, Shrabani Ghosh, Madhupriya Samanta, and Kalyan Kumar Chattopadhyay. "Tailoring the Sb_2Se_3/rGO heterointerfaces for modulation of electrocatalytic hydrogen evolution performances in acidic media." ***ACS Applied Energy Materials*, 6**, 2022, 58-67.

2. Sen, Nabanita, Nabamita Chakraborty, Biswajit Das, and Kalyan Kumar Chattopadhyay. "Strong non-linear optical response of Sb_2Se_3 nanorods in a liquid suspension based on spatial self-phase modulation and their all-optical photonic device applications." ***Nanoscale*, 15**, 2023,19671-19680.

3. Sen, Nabanita, Anup Debnath, Souvik Bhattacharjee, Bikram Kumar Das, Manas Thakur, Arnab Kumar Saha, and Kalyan Kumar Chattopadhyay. "Efficient Light to Heat Conversion in Sb_2Se_3 Nanorods and the Role of Macro-channel Imprinted Sb_2Se_3 Loaded Hybrid Membrane for Superior Desalination Performance." ***Small*,** 2024,2408293. (**https://doi.org/10.1002/smll.202408293**)

List of publications apart from thesis work

4. Debnath, Anup, Nabanita Sen, Arnab Das, Souvik Bhattacharjee, Suman Dey, Biswarup Satpati, and Kalyan Kumar Chattopadhyay. "Facile synthesis of stable 1T'-WSe2 for HER application." ***Applied Physics Letters,* 125,** 2024.

5. Dhariwal, A., D. Banerjee, N. Sen, N. Chakraborty, and K. K. Chattopadhyay. "Synergistic Effect of Adsorption and Photo-catalysis in Removal of Various Textile Dyes: Excellent Efficacy of Molybdenum Disulfide-Zinc Oxide Hybrids." ***Catalysis Today***, 2024, 115116.

6. Parashar, M., P. Kumar, K. Chauhan, N. Chakraborty, N. Sen, A. Ghoari, A. Adalder, U. K. Ghorai, K. K. Chattopadhyay, and D. Banerjee. "A comparative cyclic voltammetry study of amorphous carbon-transition metal oxide hybrid system: Selection for the best capacitor." ***Journal of Alloys and Compounds*, 975,** 2024, 172922.

7. Parashar, M., D. Banerjee, K. Chauhan, A. Adalder, U. K. Ghorai, N. Sen, and K. K. Chattopadhyay. "Efficacy of nickel doped graphitic carbon nitride as energy storage material." ***Physica Scripta*, 100**, 2024, 015930.

8. Dhariwal, A., D. Banerjee, N. Sen, K. Mitra, S. Bhowmick, and K. K. Chattopadhyay. "Two Steps Hydrothermal Synthesis of MoS_2-ZnO Hybrid for the Enhancement in Electrocatalytic Hydrogen Evolution Reaction." ***Journal of Physics and Chemistry of Solids***, 2025, 112588.

Contents

Abstract:

This work explores the untapped potential of antimony selenide (Sb_2Se_3) in emerging fields such as the hydrogen evolution reaction (HER), desalination, and nonlinear optics. This investigation is significant, as Sb_2Se_3 has primarily been recognized for its applications in solar cells due to its advantageous properties, including an optimal band gap (direct: 1.17 eV, indirect: 1.03 eV) for efficient solar light absorption, a high absorption coefficient of 10^5 cm^{-1} at shorter wavelengths, and a favourable crystal structure (space group Pbnm(62)). Its ribbon-like structure is held together by weak van der Waals forces, while strong covalent bonds exist within the ribbons. The absence of dangling bonds along the covalent bonds, along with concentrated electron density in these regions, contributes to excellent electrical conductivity along the [001] direction. Additionally, crystalline Sb_2Se_3 exhibits a high dielectric constant (~19), which reduces exciton binding energy and facilitates efficient separation of photogenerated carriers. Beyond its role in photovoltaics, Sb_2Se_3 is also valued for its thermoelectric properties, owing to its high Seebeck coefficient, as well as its potential applications in photoelectrochemical processes.

The motivation behind this thesis is to harness the full potential of Sb_2Se_3 by improving its weaker properties while also utilizing its inherent beneficial characteristics. A brief overview of the thesis is provided below.

The global shift toward clean hydrogen energy necessitates earth-abundant, noble-metal-free hydrogen evolution electrocatalysts. In this work, Chapter 4 presents a straightforward solvothermal strategy for designing Sb_2Se_3/rGO heterointerfaces to enhance electrocatalytic hydrogen evolution performance. The resulting hybrid demonstrates an improved onset potential of -0.32 V and a two-fold reduction in the Tafel slope compared to pure Sb_2Se_3.Experimental findings confirm that heterointerface engineering significantly enhances interfacial electron transport, leading to better HER performance. Density functional theory (DFT) calculations reveal that the heterointerfacial interaction lowers hydrogen adsorption energy on the (001) and (230) planes. Essentially, rGO facilitates charge redistribution at the

Sb_2Se_3/rGO interface, increasing H^+ adsorption at selective sites and thereby optimizing electrocatalytic HER activity.

The field of nonlinear optics continues to evolve, driven by the discovery of new materials with unique optical properties. In this work, chapter 5 presents, spatial self-phase modulation (SSPM) experiments using the anisotropic, layered Sb_2Se_3 material in a liquid suspension for all-optical diode and switching applications. Through a 671 nm laser beam, we determined the third-order broadband nonlinear optical susceptibility ($\chi(3)$single layer ~10^{-9} e.s.u) and nonlinear refractive index (n_2 ~10^{-6} cm^2/W) of Sb_2Se_3. These findings can be attributed to the material's anisotropic hole mobility, which plays a key role in the formation of diffraction patterns through nonlocal hole coherence, as evidenced by the linear relationship between $\chi(3)$ and carrier mobility. The time evolution of the diffraction rings aligns with the "Wind-Chime" model.

Furthermore, we demonstrate a novel photonic diode based on Sb_2Se_3/SnS_2, leveraging the nonreciprocal propagation of light. Using the self-phase modulation (SPM) technique with varying laser wavelengths and intensities, we successfully implement all-optical logic gates, particularly the OR logic gate. This exploration of Sb_2Se_3's nonlinear optical properties open new opportunities for optical information processing and communication.

Chapter 6 presents a theoretical and experimental validation of Sb_2Se_3 nanorods (NRs) as a promising candidate for solar thermal heat generation. Through customized water droplet experiments, the light-to-heat conversion efficiencies of Sb_2Se_3 were determined to be approximately 57.8% and 58% for red (671 nm) and green (532 nm) lasers, respectively. Building on this, we developed PVDF(M)/Sb_2Se_3 NRs hybrid membranes for solar desalination, which achieved a temperature of ~59°C within 15 minutes of illumination. The primary mechanism driving heat generation is electron/hole-acoustic phonon scattering.

Despite the superior visible-NIR absorption and heat localization of Sb_2Se_3 NRs, the hybrid membranes exhibited a limited evaporation rate of 1.72 kg m^{-2} h^{-1}, even with increased mass loading. This limitation arises from the hydrophobic nature of the

Sb_2Se_3 NRs layer, which restricts uniform water diffusion to hot zones, thereby reducing solar evaporation efficiency. To overcome this challenge, we introduced a novel mechanical imprinting strategy to create macro-channels in the hybrid membranes. These macro-channels significantly enhance water transport to hot zones, leading to an improved mass loss rate of ~2.37 kg m^{-2} h^{-1} and a solar evaporation efficiency of 148% under a mercury vapor lamp with an intensity of 1000 W m^{-2}.

Furthermore, outdoor sunlight experiments demonstrated a commendable solar evaporation efficiency of ~108%. The steam generated through this solar thermal process effectively removes heavy metal ions, ensuring compliance with the World Health Organization (WHO) standards for potable water. This study highlights macro-channel imprinting as a viable strategy for improving desalination efficiency in hydrophobic materials, with potential applicability to other similar systems.

This thesis highlights the potential benefits of using Sb_2Se_3 in research areas such as HER, desalination and nonlinear optics. It is believed that further opportunities remain in these fields with continued exploration of Sb_2Se_3.

Nabanita Sen
Signature of the candidate

Date: 05.02.2025

Signature of the supervisor

Date: 5.2.2025

Dr. K. K. Chattopadhyay
Professor
Department of Physics
Jadavpur University
Kolkata-700 032

Chapter 1 Introduction

This chapter is motivated by the need to harness Sb_2Se_3 nanorods in the relatively untapped areas of hydrogen evolution reaction, nonlinear optics and desalination. It also provides a discussion on the fundamental scientific concepts related to these applications and reviews previous research in these fields.

1.1 Preamble

A significant amount of research has been conducted globally on Sb_2Se_3 as an absorber material for solar cells [1] and thermoelectric applications [2]. Sb_2Se_3 nanostructures are becoming increasingly popular in various fields, including solar cells,[1] photoelectrochemical applications,[3] thermoelectric devices,[2] photodetectors,[4] and energy storage systems.[5] This material is an excellent example of a solar cell material due to its optimum band gap (1.0 eV-1.2 eV) and its high absorption coefficient of 10^5 cm^{-1} at shorter wavelengths. [1] The Shockley-Queisser limit represents the maximum theoretical efficiency that a solar cell with a single p-n junction can achieve, with the peak efficiency being 30% at a band gap of 1.1 eV. This material also exhibits a high Seebeck coefficient, making it well-suited for thermoelectric applications. To date, substantial effort has been dedicated to advancing the fields of solar cells, thermoelectric applications, photodiodes and other technologies using Sb_2Se_3 nanomaterials. However, there are still potential application areas where the use of Sb_2Se_3 nanomaterials remains unexplored.

Today, the hydrogen economy is an emerging field, with green hydrogen playing a crucial role in sustainable energy storage, chemical production and transportation. [6] By reducing reliance on fossil fuels, the use of green hydrogen helps mitigate the greenhouse effect, acid rain and high ozone levels. The production of sustainable hydrogen through low-energy electrochemical reactions requires advanced catalysts. India has committed ₹17,400 crore to its Green Hydrogen Mission and set a goal to produce 5 million tons of hydrogen annually by 2030.[7] Furthermore, the global population is experiencing a severe water crisis driven by increasing demand for freshwater, pollution, depletion of water resources and rising needs in industrial and agricultural sectors. Desalination offers an effective solution to address this challenge. Solar desalination specifically harnesses solar energy to heat absorber materials, which is then used to transform seawater into freshwater.[8] Furthermore, modern computing demands swift signal processing and fast communication, which rely on high-speed logic within the processor. Achieving this level of performance necessitates integrating additional electronic components into the processor to

support these advanced logic operations. In sharp contrast, optical signal processing presents several advantages, such as ultra-high bit rates, extensive bandwidth and extremely low crosstalk. To implement an all-optical system in modern computer processors, optical diodes and all-optical logic gates are required. These components process optical signals by manipulating their intensity, phase and polarization through light-matter interactions. An emerging technique in optical nonlinearity is Spatial Self-Phase Modulation (SSPM), where the phase of light is spatially modulated through nonlinear light-matter interactions.[9]

This dissertation demonstrates that Sb_2Se_3 plays a significant role in the three areas discussed: electrochemical hydrogen evolution reaction, desalination and spatial self-phase modulation.

1.2 Importance of Sb_2Se_3

The beneficial and profitable applications of a material largely depend on its fundamental and unique properties. While this perspective may seem oversimplified, it provides a general sense of the material's potential. However, it overlooks aspects such as synergistic interactions or the effects of doping. This section classifies Sb_2Se_3 into two groups, as depicted in figure 1.1: properties that are intrinsically advantageous and those that require enhancement.

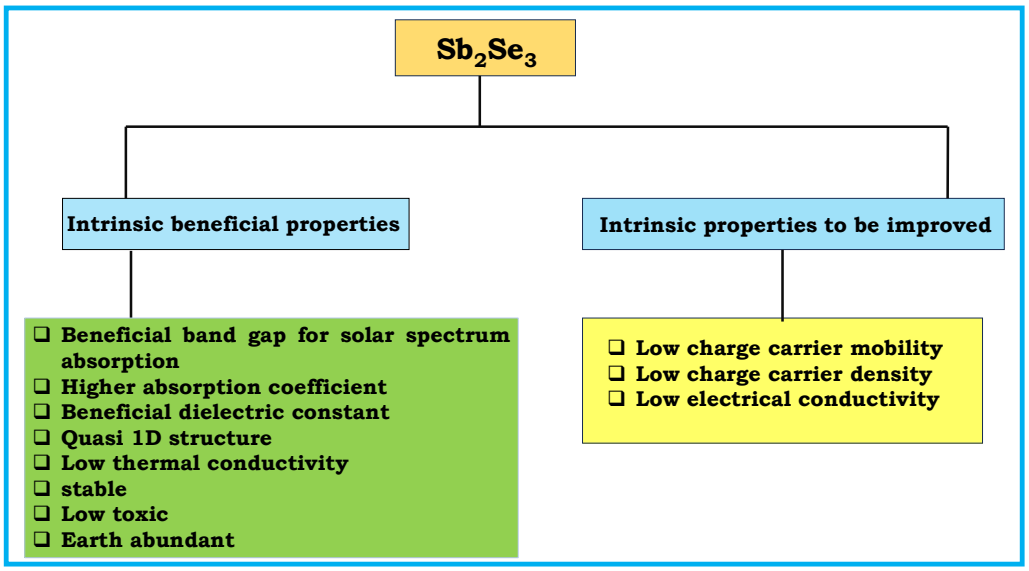

Figure 1.1: *Properties of Sb_2Se_3*

1.2.1 Crystal structure of Sb_2Se_3

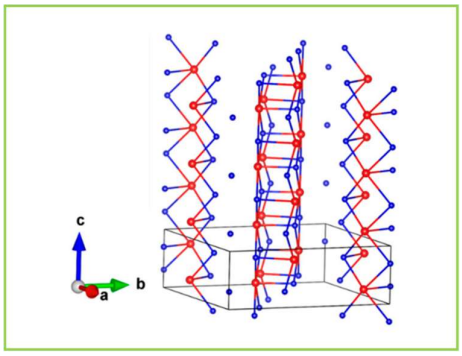

Figure 1.2: *Pbnm space group of Sb_2Se_3*

Sb_2Se_3 is a binary chalcogenide material belonging to the V-VI group. However, discrepancies in the reported space groups (Pbnm and Pnma) for Sb_2Se_3 have caused some confusion in the literature. For the Pbnm space group represents in figure 1.2, the lattice parameters are a = 11.62 A˚, b = 11.77 A˚, c = 3.962 A˚, While for the Pnma space group, they are a = 11.7938 A˚, b = 3.9858 A˚, c = 11.6478 A˚.[10] Despite these differences, both space groups describe the same orthorhombic crystal structure, differing only in the permutation of the axes. In this context, all spatial directions of Sb_2Se_3 are analyzed based on the Pbnm space group. Sb_2Se_3 consists of $(Sb_4Se_6)_n$ ribbons aligned along the c-axis, giving it a quasi-1D structure. The ribbons are held together by weak van der Waals forces (Se-Se interactions) oriented along the (010) planes, with a relatively large interatomic distance of 2.98 Å between them. Within each ribbon, the atoms are connected by strong covalent bonds, resulting in significant anisotropy across different orientations of Sb_2Se_3.[10]

Disadvantage of this crystal structure

The weak van der Waals bonds between the ribbons and the grain boundaries aligned with these bonds restrict the carrier mobility between the ribbons.

Advantage of this crystal structure

Electron density is concentrated along the covalent bonds within the ribbon, with grain boundaries running parallel to the ribbons. As a result, there are no dangling bonds along the covalent bond orientation. Consequently, Sb_2Se_3 demonstrates excellent electrical properties in the [001] direction. It demonstrates high electron and hole mobility along this direction, making it advantageous for applications in photovoltaics (PV), photodetectors and photoelectrochemical (PEC) systems, as highlighted in the review of past work. Therefore, the orientation of the crystal plane plays a vital role in modulating its electrical properties and expanding the potential applications of Sb_2Se_3.

1.2.2 Optical properties and band structure of Sb_2Se_3

For solar cells, the absorber material should possess the following characteristics:

- A high absorption coefficient in the relevant spectral range
- An appropriate band gap
- Efficient charge carrier transport properties to capture photogenerated carriers before recombination
- A uniform electric field across the p-n junction, as dangling bonds and crystal defects can disrupt field uniformity
- High charge carrier mobility
- Long charge carrier lifetime
- A large dielectric constant and low excitation energy

Sb_2Se_3 has a suitable band gap for solar cell applications, featuring both a direct band gap of 1.17 eV and an indirect band gap of 1.03 eV. It exhibits a high absorption coefficient of $10^5\,cm^{-1}$ in the shorter wavelength region.[10] As a result, an Sb_2Se_3 layer only 800 nm thick is sufficient to absorb photons within the 400–1000 nm wavelength range. In contrast, silicon solar cells have a lower absorption coefficient that varies with wavelength. To achieve effective optical absorption, silicon solar

cells require a thickness exceeding 100 µm. That's why Sb_2Se_3 holds significant importance in photovoltaics, with over many research studies available on Sb_2Se_3 solar cells. A select few of these are discussed in the review of previous work.

1.2.3 Dielectric constant of Sb_2Se_3

In crystalline Sb_2Se_3, the dielectric constant is relatively high (≈19) along the ribbon direction, surpassing that of amorphous Sb_2Se_3 (≈16).[10] This high dielectric constant reduces the exciton binding energy, facilitating the efficient separation of photogenerated carriers, which is advantageous for photovoltaic (PV) applications. Additionally, the dielectric tensor in crystalline Sb_2Se_3 exhibits anisotropy, with the highest value, ϵ_{zz} = 15.46, occurring in the ribbon direction. [10] Therefore, selecting an appropriate crystal plane orientation is crucial to achieve a higher dielectric constant.

1.2.4 Electronic properties of Sb_2Se_3

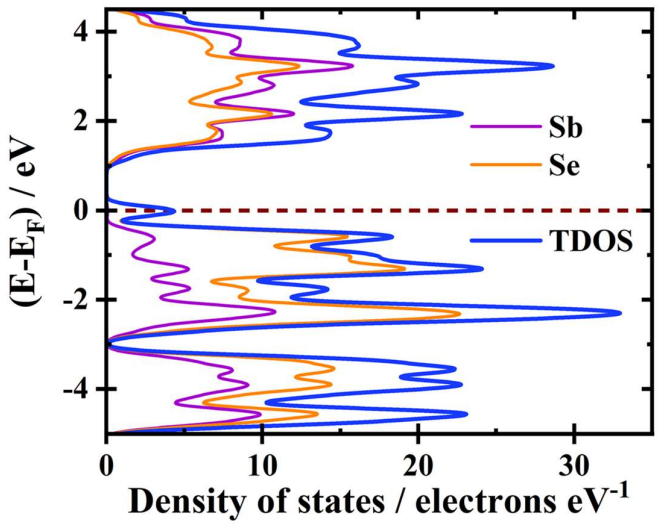

Figure 1.3: *partial and total electron density of states of Sb_2Se_3*

The figure 1.3 above illustrates the partial and total electron density of states (DOS) of Sb_2Se_3. In the DOS, the highest occupied valence band (VB), ranging from -5.5 eV to 0 eV, is primarily dominated by Se 4p states and Sb 5p states. In the valence band region, the Sb 5p density is lower compared to the Se 4p density. However, in the conduction band (CB), the Sb 5p states contribute more significantly than the Se 4p

states. Overall, the formation of the Sb_2Se_3 band structure is primarily influenced by the 5s and 5p orbitals of Sb atoms, rather than the 4s and 4p orbitals of Se atoms. [10] Typically, Sb_2Se_3 exhibits p-type conductivity, but it shows n-type conductivity when doped with elements like Te or Bi. Moreover, an increased Sb content also results in n-type conductivity. [10]

Disadvantage of this electronic structure

The free charge carrier density in Sb_2Se_3 is lower (10^{13} cm^{-3}) than the optimal value of 10^{16} cm^{-3} required for solar cells. This is due to the presence of deep traps in Sb_2Se_3, which contribute to a higher defect density. To improve the performance of Sb_2Se_3, it is essential to reduce these deep traps.[10]

Advantage of this electronic structure

Sb_2Se_3 is typically used as an absorber material in solar cells for its p-type conductivity. When oriented in the optimal crystal direction, it demonstrates high hole mobility (22 $cm^2.V^{-1}.s^{-1}$). [10]

Given the properties mentioned above, Sb_2Se_3 is utilized in applications such as photovoltaics (PV), photoelectrochemical (PEC) cells and photodetectors. However, its potential in areas like the hydrogen evolution reaction (HER), desalination and nonlinear optics remains underexplored. The key aspects of these applications are presented below.

1.3 Water Electrolysis

Water electrolysis is a method in which electricity is used to separate water (H_2O) into its basic components—hydrogen (H_2) and oxygen (O_2).[11] This is done by running an electric current through water, often with an electrolyte added to improve conductivity.

Water electrolysis involves two half-reactions at two electrodes represents in figure 1.4:

1. **Cathode (Reduction Reaction)**: At the cathode, water molecules gain electrons (reduction), producing hydrogen gas (H_2) and hydroxide ions (OH^-).
    - Reaction: $2H_2O + 2e^- \rightarrow H_2 + 2OH^-$
2. **Anode (Oxidation Reaction)**: At the anode, water molecules lose electrons (oxidation), producing oxygen gas (O_2) and hydrogen ions (H^+).
    - Reaction: $2H_2O \rightarrow O_2 + 4H^+ + 4e^-$

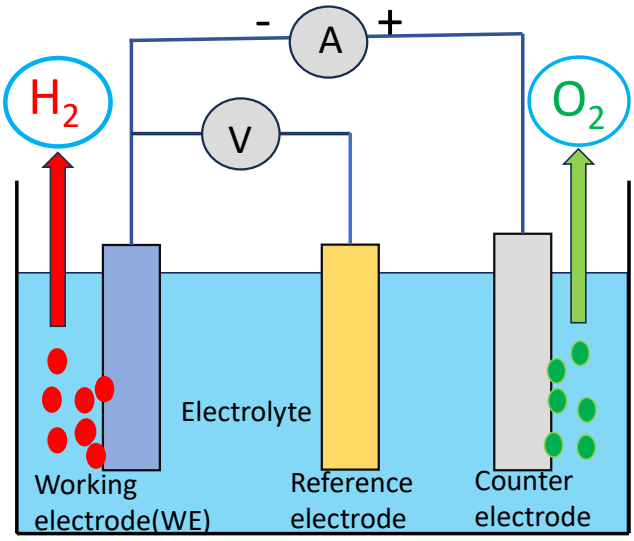

Figure 1.4: *Schematic representation of the conventional three electrodes water electrolysis cell under working condition*

The hydrogen produced can be used as a clean fuel, making water electrolysis a key technology in renewable energy and hydrogen production. This process is especially valuable in green hydrogen production when powered by renewable energy sources like solar or wind.

1.3.1 Thermodynamic potential for water electrolysis

At standard temperature and pressure, water electrolysis is not thermodynamically favourable. This reaction requires external energy to proceed.[11] Therefore, the

thermodynamic potential for the reactions at the cathode and anode under these conditions is provided below.

At 25 °C and pH 0 ([H+] =1.0 M) condition

Cathode (reduction): $2H^+ + 2e^- \rightarrow \ 2H_2$; $E^0_{red} = 0.000\ V\ vs.NHE$

Anode (oxidation):$2H_2O \ \rightarrow 4H^+ + 4e^- + O_2$; $E^0_{red} = 1.229\ V\ vs.NHE$

So the standard potential for the water electrolysis cell

$E^0_{cell} = \ E^0_{caho} \ - E^0_{anode}$ = (0-1.229) =-1.229 V

The overall cell potential remains unchanged under different pH conditions, as demonstrated by the Pourbaix diagram of water represents in figure 1.5.

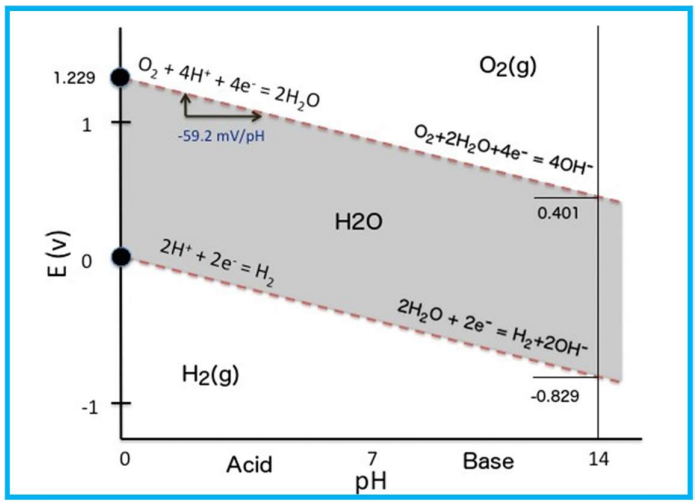

Figure 1.5: *Pourbaix or potential-pH diagram for water at standard temperature and pressure (STP)*

The Gibbs free energy change for this reaction is calculated using the following equation:

$$\Delta G^0 = \ -nF.\Delta E^0$$

Here, ΔG^0 is the Gibbs free energy change and ΔE^0 is the cell potential of the reaction, F is the Faraday constant 96,485 C/mol, n= 2 for one water molecule electrolysed. Since this is an endothermic process, it requires an input of energy

equivalent to +237 kJ/mol (under standard temperature and pressure) for water to be split.

1.3.2 Onset potential and Overpotential of Hydrogen Evolution Reaction

In theory, all reactions in water electrolysis occur at a specific thermodynamic potential. However, in real-world systems, additional potential beyond the thermodynamic value is needed to complete the water electrolysis process. This is because the process is controlled by kinetics and factors such as activation energy barriers, ion mobility and concentration, wire resistance and bubble formation on the electrode surface create challenges that require a higher potential to overcome. This extra potential is known as overpotential and is represented by the symbol η

$$\eta_{HER} = \text{Experimentally obtained potential (V)} - 0\text{(V)}$$

In electrochemical reactions, the onset potential is the potential at which the current begins to increase.

1.3.3 Role of catalyst in hydrogen evolution reaction

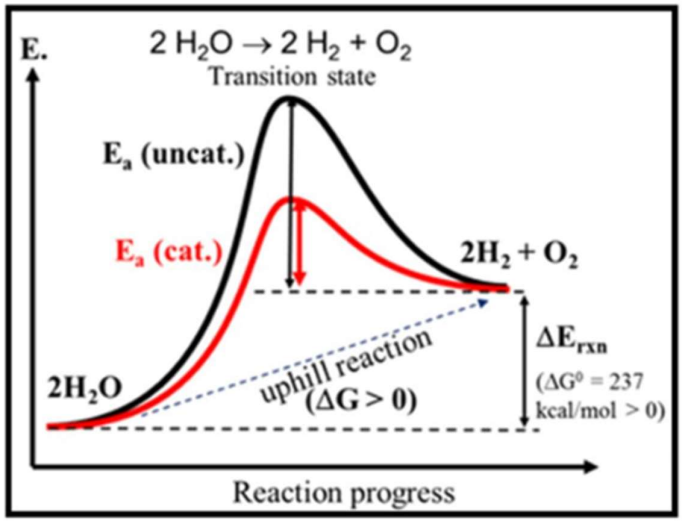

Figure 1.6: *Reaction progresses vs. activation energy for water electrolysis. [12]*

In a typical chemical reaction, a catalyst is used to accelerate the reaction rate while remaining unchanged at the end of the process. In the case of hydrogen evolution reactions, catalysts are essential for reducing the activation energy barriers represents in figure 1.6, which are much higher than the theoretical limit of 1.23 V. By lowering these energy barriers, catalysts enhance the speed at which the reaction proceeds.[12]

In hydrogen evolution reactions, a catalyst should possess certain key properties strong proton adsorption, efficient electron transport with high conductivity, easy desorption of hydrogen molecules and long-term durability under industrial-scale current densities (>500 mA/cm^2).

1.3.4 Sabatier principle

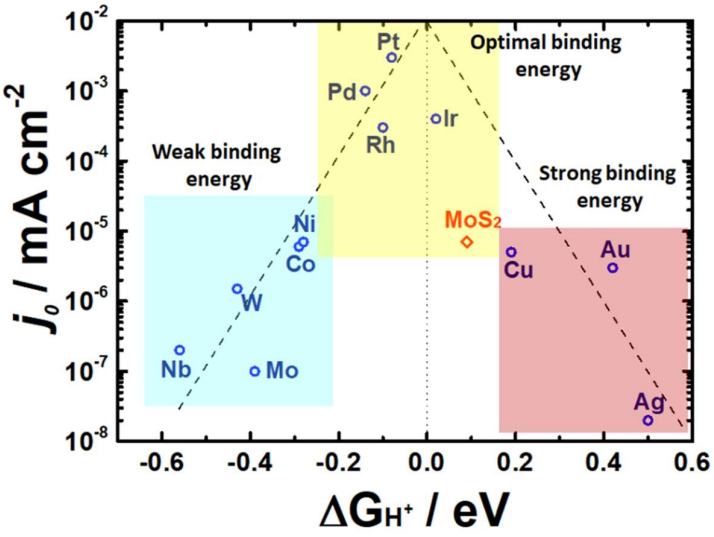

Figure 1.7: *Volcano plot of different materials in hydrogen evolution reaction*

The previous section's discussion on the interaction between the catalyst and reactants may seem a bit unclear. The catalyst needs to strongly adsorb protons, yet at the same time, it must also facilitate the easy desorption of H_2 molecules. The Sabatier principle provides guidance in balancing these competing demands, ensuring optimal interaction between the catalyst and the reactants.

The Sabatier principle suggests that the interaction between the catalyst and reactants should be balanced—not too strong or too weak.[13] If the adsorption is

too strong, fewer H_2 molecules are released, leading to sluggish kinetics during the hydrogen evolution reaction (HER). Conversely, if the adsorption is too weak, the reactants may not activate properly, and the reaction will not occur.

The Sabatier principle is commonly applied in heterogeneous catalysis and is often illustrated using volcano plots. In figure 1.7 plots, the x-axis represents the binding strength between the catalyst and reactants, while the y-axis indicates catalytic activity. The optimal activity is found at the peak of the volcano, where the Gibbs free energy (ΔG_H) is zero. The left side of the plot corresponds to strong binding (ΔG_H is negative), while the right side represents weak binding (ΔG_H is positive).

Figure 1.7 show volcano representation of the Sabatier principle and illustrates its application in the hydrogen evolution reaction (HER). Platinum (Pt) is positioned at the peak of the volcano plot, making it one of the most effective catalysts for HER.

1.3.5 Current -Voltage relationship in electrode-electrolyte interface (Butler- Volmer equation)

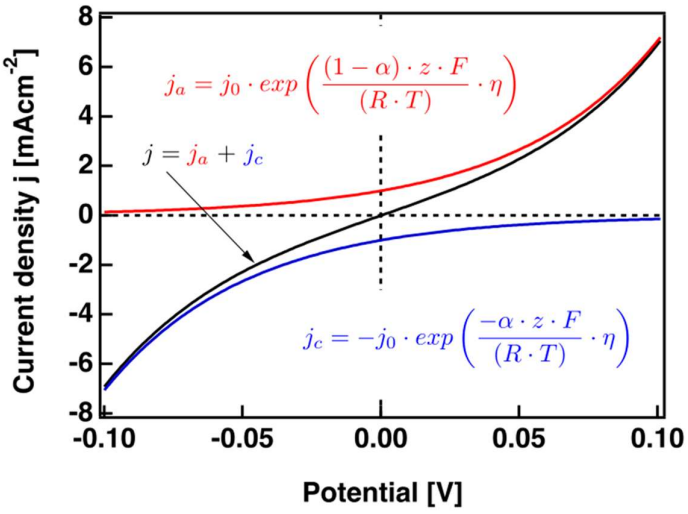

Figure 1.8: *Current density as function of overpotential (Butler-Volmer equation) [14]*

For an electrochemical reaction, the forward (anodic) and backward (cathodic) reactions can be expressed as: $O_x + e^- \leftrightarrow R_x$ where O_x is the oxidized species and R_x is the reduced species.

The net current density j is the difference between the anodic current density j_a and the cathodic current density j_c

$$j = j_a - j_c$$

The anodic and cathodic current densities are proportional to the rates of the forward and backward reactions:

$$j_a = nFAk_a[O_x]$$

$$j_c = nFAk_c[R_x]$$

where n is the number of electrons transferred, F is Faraday's constant, A is the electrode area, and k_a and k_c are the rate constants for the anodic and cathodic reactions, respectively.

The rate constants k_a and k_c are dependent on the overpotential η. The rate constants can be expressed as:

$$k_c = k_0 exp\ (-\alpha nF\eta/RT)$$

$$k_a = k_0 exp\ ((1-\alpha)nF\eta/RT)$$

where k_0 is the standard rate constant, α is the transfer coefficient, R is the gas constant, and T is the temperature.

Substituting the expressions for j_a and j_c, the total current density is:

$$j = nFAk_0[O_x]\ exp\ ((1-\alpha)nF\eta/RT) - nFAk_0[R_x]exp\ (-\alpha nF\eta/RT)$$

At equilibrium, η=0 and the equilibrium current densities are equal:

$$j_0 = nFAk_0[O_x]_{eq} = nFAk_0[R_x]_{eq}$$

Therefore, we can express the equilibrium concentrations in terms of the exchange current density j_0,

Figure 1.8 shows current – voltage relationship of electrode -electrolyte interface and final form of Butler-Volmer equation,[15]

$$j = -j_0\{exp\,(-\alpha nF\eta/RT) - exp\,((1-\alpha)nF\eta/RT)\}$$

j_0: Exchange current density, which is the current density at equilibrium (no overpotential).

η: Overpotential, the difference between the applied potential and the equilibrium potential.

α: Transfer coefficient, typically between 0 and 1, which indicates the symmetry of the energy barrier.

Two limiting cases

- ✓ **If** η is small exp(x) can be approximated by a Taylor Maclaurin series expansion as 1+x ….

  $$j = j_0 nF\eta$$

  For small η means η < 30 mV
- ✓ **If** η is large then Butler-Volmer equation turns into Tafel equation which is

  $$\eta = \pm \boldsymbol{b} log_{10}\frac{j}{j_0} + C$$

  b is Tafel slope, C is constant

1.3.6 Reaction steps and kinetics during the Hydrogen Evolution Reaction

In an acidic environment

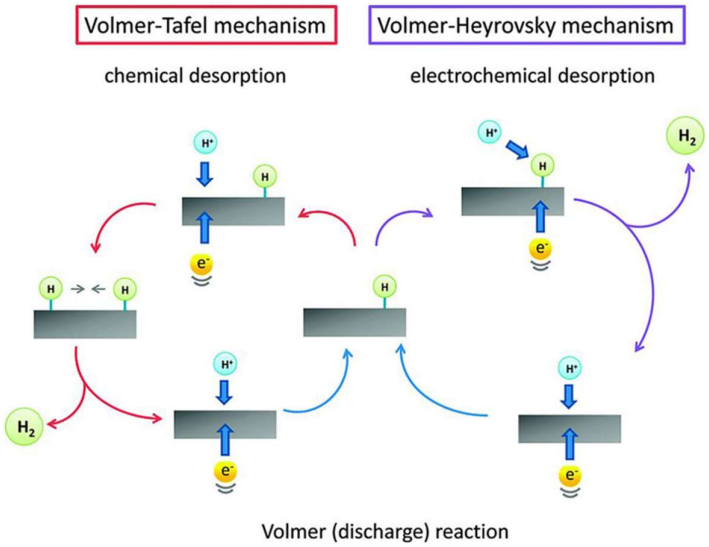

Figure 1.9: *Multiple steps of HER in acidic medium [16]*

The overall hydrogen evolution reaction in an acidic environment is represented as follows.

$$2H^+ + 2e^- \rightarrow H_2$$

However, this process consists of multiple steps represents in figure 1.9 leading to the final stage.

Volmer step $* + H^+ + e^- \leftrightarrow * H_{ad}$

Heyrovsky step $* H_{ad} + e^- + H^+ \rightarrow H_2 + *$

Tafel step $2 * H_{ad} \rightarrow H_2 + 2 *$

Where * denotes the surface-active side of the electrode.

The Volmer step is the crucial initial stage where a hydrogen atom adsorbs onto the electrode surface. This stage is an indispensable part of the hydrogen evolution reaction and cannot be omitted.

The Hydrogen Evolution Reaction (HER) can proceed via either the Volmer-Heyrovsky or Volmer-Tafel mechanisms. The dominant mechanism throughout the reaction is determined by the Tafel slopes, which are 120, 40 and 30 mV dec^{-1} for the Volmer, Heyrovsky and Tafel steps, respectively.[16] If the catalytic sites are close together, the Tafel step is more likely to occur, whereas if the catalytic sites are spaced farther apart, the Heyrovsky step becomes more favourable.

In alkaline medium

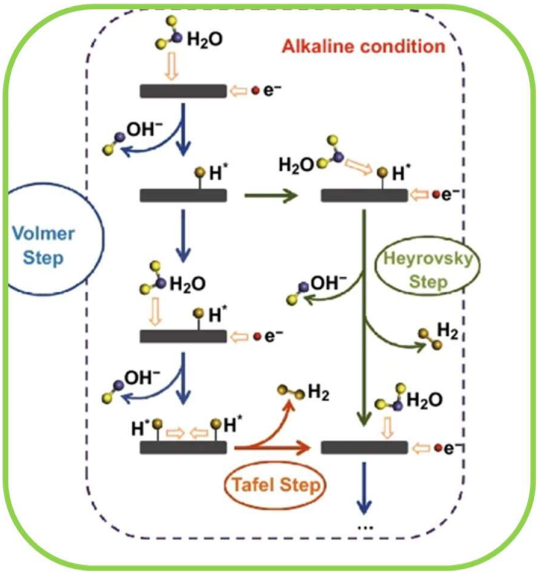

Figure 1.10: *Multiple steps of HER in alkaline medium [17]*

In an alkaline environment, the number of available protons (H+) is almost zero. Therefore, an additional step is required to produce protons by dissociating water, which slows down the hydrogen evolution reaction (HER). As a result, the kinetics of hydrogen production in alkaline conditions are sluggish.

In sharp contrast to acidic conditions, in an alkaline medium, the Volmer step relies on an additional water dissociation step. Therefore, the hydrogen evolution reaction

(HER) in alkaline environments involves multiple steps, represents in figure 1.10 [17] which are as follows:

Volmer step- water dissociation: $H_2O + e^- \rightarrow H^* + OH^-$

Tafel step : $H^* + H^* \rightarrow H_2$

Heyrovsky step- water dissociation: $H^* + H_2O + e^- \rightarrow H_2 + OH^-$

In this case, an additional water dissociation step occurs, which is why a Tafel slope of 120 mV per decade is commonly observed.

1.3.7 Electrochemically Active Surface Area of a Catalyst in Hydrogen Evolution Reaction

The Electrochemical Active Surface Area (ECSA) is a key factor in assessing the catalytic performance of a catalyst in hydrogen evolution reactions. A larger ECSA provides more active electrochemical sites, leading to enhanced catalytic activity and improved hydrogen evolution efficiency.[18]

The Electrochemical Active Surface Area (ECSA) is determined based on the electrochemical double-layer capacitance and can be represented by the following equation.

$$ECSA = \frac{C_{dl}}{C_s}$$

Here, C_{dl} represents the electrochemical double-layer capacitance, while Cs refers to the standard capacitance, with its value depending on the specific electrolyte used.

1.3.8 Electrochemical double layer capacitance

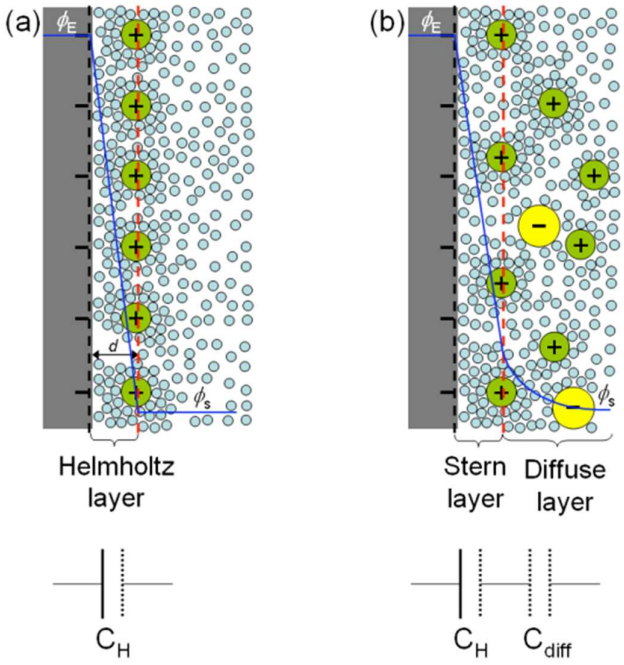

Figure 1.11: *Electrochemical double layer models (a)Helmholtz model (b)Gouy -Chapman-Stern model [19]*

Various electrochemical double layer models represent in figure 1.11. In 1879, Helmholtz discovered that when an electrode is immersed in an electrolyte and a potential is applied, counter charges accumulate on the electrolyte side. This setup functions similarly to a parallel plate capacitor. The compact layer of charges that forms on the electrolyte side is known as the Helmholtz layer,[19] and the system's capacitance is

$$C_H = \frac{A\epsilon_r\epsilon_0}{d}$$

ϵ_r is the dielectric constant of the electric double layer, ϵ_0 is the vacuum permittivity, A is the surface area of the electrode and d is the separation between the surface charge layer of the electrode and the counter-ion layer. (i.e. the compact layer thickness)

There is uncertainty in the values of two key parameters in the Helmholtz model: the dielectric constant and the distance (d). The distance is influenced by how the

counter-ions are adsorbed onto the electrode. If the bare ions are adsorbed, the distance is determined by the size of the bare ion. However, if the ions are surrounded by water molecule, the distance is based on the size of the solvated ion. Additionally, the dielectric constant of water in the compact layer differs from that in bulk water. Near a charged surface, the dielectric constant is around 6, which is significantly lower than the bulk water value of 78. To address these variations, a revised Helmholtz model was introduced, dividing the compact charge layer on the electrolyte side into two parts: the inner Helmholtz layer and the outer Helmholtz layer.

The Helmholtz model is modified on electrode surfaces that are not fully screened by counter-ion charges in the compact layer. Due to thermal motion, the counter-ions can disperse into a diffuse layer that lies next to the compact layer. Therefore, the electrochemical double layer capacitance is composed of two parts connected in series: a compact layer, often referred to as the Stern layer or inner Helmholtz layer, and a diffuse layer known as the outer Helmholtz layer. This configuration of the electrochemical double layer is described by the Gouy-Chapman-Stern model.

In the Gouy-Chapman-Stern (GCS) model[19] for monovalent electrolytes, the distribution of the electric potential within the diffuse layer is determined by the Poisson-Boltzmann equation.

$$\Delta(\Delta\Phi\epsilon_r\epsilon_0) = 2eC_0 \sinh\left(\frac{e\Phi}{K_B T}\right)$$

Where Φ is the electric potential, C_0 is the bulk electrolyte concentration, e is the electron charge, KB is the Boltzmann constant, T is the absolute temperature. By solving the Poisson-Boltzmann equation,[19] the capacitance of the diffuse layer is obtained as

$$C_{diff} = \frac{\epsilon_r\epsilon_{0A}}{\lambda_D}\cosh\left(\frac{e\Phi_{diff}}{2k_B T}\right)$$

Where $\Phi_{\text{diff is}}$ the potential drop across the diffuse layer and λ_D is the characteristic Debye length.

So, electrochemical double layer capacitance highly depends on Debye length and concentration of the electrolyte.

1.3.9 Measurement procedure of EDLC

To measure the electrochemical surface area (ECSA), the double layer capacitance (C_{dl}) is first determined using cyclic voltammetry (CV) analysis. CV scans of the electrocatalyst are performed at various scan rates within a non-Faradaic potential region. The difference between the anodic and cathodic currents is measured in this non-Faradaic potential region and then plotted against the different scan rates. The slope of the resulting linear plot, divided by two, represents the double layer capacitance (C_{dl}).

1.4 Nonlinear Optics (Spatial self-phase modulation)

1.4.1 Preamble:

Since ancient times, light has fascinated humanity with its captivating properties and invaluable utility. The study of light has drawn human interest through the exploration of its fascinating properties. The discovery of more intriguing properties of light could unlock its full potential. This progress may take humanity beyond the classical study of optics, where wave aspects of light explain phenomena such as interference and diffraction. Moving beyond classical optics leads to the realm of quantum phenomena, where light is understood as discrete packets of energy known as photons. The interaction between photons and electrons has given rise to an exciting new field called photonics. Day by day, new and intriguing aspects of light-matter interactions are being discovered, deepening our understanding of light. These interactions have also driven a technological revolution in communication systems, enabling the transmission of information over long distances using light.

Optical communication remained a distant dream until Maiman's invention of the laser in 1960. The development of a coherent, high-intensity beam of light opened up new fields such as nonlinear optics,[20] fiber optics,[21] and advanced forms of spectroscopy.

We currently live in the age of electronics, where the world thrives on advanced electronic technologies. However, these technologies are now approaching their physical limits. According to Moore's law,[22] the number of transistors on computer chips doubles roughly every two years. To achieve higher-speed logic, an increasing number of transistors is required.

To address these limitations, optoelectronics[23] and electro-optics[24] have emerged as promising solutions and an evolving field. In electronic circuits, electrons can regulate or influence the behaviour of other electrons. For instance, in a transistor, the base current controls the emitter-collector current, leading to the development of electronic amplifiers, oscillators and more.

In contrast to electrons, a propagating beam of light cannot directly control or influence another beam of light traveling through the same medium simultaneously. However, optical nonlinearity enables such interactions, allowing energy exchange between light beams propagating together in suitable media, provided the light intensity is sufficiently high.

Based on nonlinear light-matter interactions, devices such as all-optical diodes and all-optical logic gates have been developed. These devices enable logic functions by manipulating the intensity, phase, polarization, or wavelength of optical signals through interactions with light.

1.4.2 Origin of optical nonlinearity in material

When an atom is exposed to an electromagnetic field, the field interacts with both the positive and negative charge canters, causing the electron cloud to deform. This deformation can be quantified. The distance between the positive and negative charge centres is known as the induced electric dipole moment $\vec{p}$, which results from the influence of the electric field on the atom.

$$\vec{p} = q_i \vec{r}_i$$

Where q_i is the electric charge located at the point denoted by the position vector $\vec{r}_i$.

The induced dipole moment $\vec{p}$, is related to electric field strength according to

$$\vec{p} = \alpha\vec{E}$$

Where α is the electronic polarizability of the atom.

Due to induced dipole moment the overall induced macroscopic polarization $(\overrightarrow{P})$over volume V of the atom is defined as

$$\vec{P} = \frac{\Sigma\vec{p}_i}{V}$$

In linear optics the relationship between polarization and the strength of the electric field $\vec{E}$ is $\vec{P} = \epsilon_0\chi^{(1)}\vec{E}$

However, when electric field is large enough in case of laser, when intensity I is large and $I \propto E^2$

Then the optical response of a material may be expressed in a series expansion of the polarization in powers of the electric field [25]

$$\vec{P} = \epsilon_0\left[\chi^{(1)}\,\vec{E} + \chi^{(2)}\,\vec{E}\vec{E} + \chi^{(3)}\,\vec{E}\vec{E}\vec{E} + \cdots\right]$$

The various electric susceptibilities $\chi^{(n)}$, n =2, 3…. correspond to nonlinear optical polarization of the material. In nonlinear optics, a significant electric field is required, and it equally depends on the material's susceptibility. Now we can look at nonlinear optical susceptibilities in the next section to determine their physical manifestations.

1.4.3 Optical Kerr effect

For centrosymmetric system

$$\chi^{(2)} = 0$$

$$P_{NL}^{(3)} = \epsilon_0\chi^{(3)}\,\vec{E}\vec{E}\vec{E}$$

$$\vec{E} = \frac{1}{2}\left[E_0 e^{i(kz-\omega t)} + c.c\right]$$

$$P_{NL}^{(3)} = P_{NL}^{(3\omega)} + P_{NL}^{(\omega)}$$

$P_{NL}^{(3\omega)} = \frac{\epsilon_0\chi^3}{8}\left[E_0^3 e^{3i(kz-\omega t)} + c.c\right]$ 3rd harmonic generation (3HG)

$$P_{NL}^{(\omega)} = \frac{\epsilon_0 \chi^3}{8}\left[3E_0|E_0^2|e^{i(kz-\omega t)} + c.c\right]\text{-} \quad \omega \text{ generation}$$

Now,

$$\vec{P}_{Total} = \vec{P}_L + \vec{P}_{NL}$$

$$\vec{P}_{Total} = \epsilon_0\left(\chi^{(1)} + \frac{3}{4}\chi^{(3)}|E_0|^2\right)\vec{E}$$

$$\vec{P} = \epsilon_0 \chi_{eff}^{(3)} \vec{E}$$

$$\chi_{eff}^{(3)} = \left(\chi^{(1)} + \frac{3}{4}\chi^{(3)}|E_0|^2\right)$$

$$n^2 = \left(1 + \chi_{eff}^{(3)}\right) = 1 + \chi^1 + \frac{3}{4}\chi^{(3)}|E_0|^2$$

n is the total refractive index of the material.

$$n^2 = n_0^2 + \frac{3}{4}\chi^{(3)}|E_0|^2$$

Where, $n_0^2 = 1 + \chi^1$

$$n^2 = n_0^2\left(1 + \frac{3}{4n_0^2}\chi^{(3)}|E_0|^2\right)$$

$$n = n_0\sqrt{\left(1 + \frac{3}{4n_0^2}\chi^{(3)}|E_0|^2\right)}$$

$$n \approx n_0\left(1 + \frac{3}{8n_0^2}\chi^{(3)}|E_0|^2\right)$$

$n = n_0 + n_2 \text{I}$ where $I = \frac{1}{2}\epsilon_0 n_0 c|E_0|^2$

n_0 is the linear refractive index and n_2 is the nonlinear refractive index

$$\text{Where, } n_2 = \frac{3\chi^{(3)}}{4\epsilon_0 n^2 c}$$

When the refractive index of a material changes under the influence of a strong electric field or high-intensity laser light, the phenomenon is known as the optical Kerr effect.[25] This change in refractive index leads to various nonlinear optical responses,

including self-focusing, spatial self-phase modulation and modulational stability, among others.

1.4.4 Spatial -self phase modulation (SSPM)

Spatial self-phase modulation (SSPM) [26] is a nonlinear optical phenomenon that occurs when a high-intensity laser beam propagates through a nonlinear medium, causing spatial variations in the refractive index due to the optical Kerr effect. These variations arise because the refractive index of the medium changes proportionally to the intensity of the laser light. As a result, the phase of the light wave becomes spatially modulated, leading to changes in the beam profile.

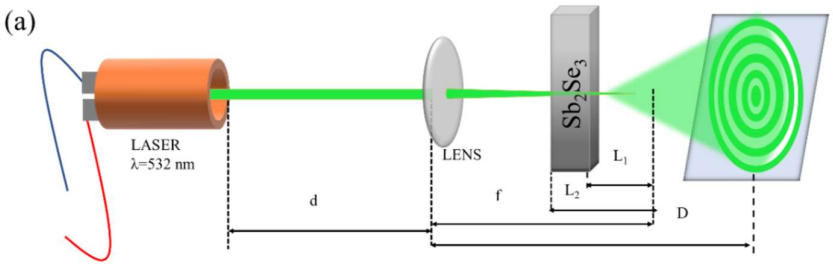

Figure 1.12 *Schematic of instrumental set up of SSPM technique*

According to the optical Kerr effect, the refractive index (n) of the materials has a strong dependence on the intensity (I) of the incident laser light and the relation between them has been presented as $n = n_0 + n_2 I$; where n_0 and n_2 are the linear and nonlinear refractive index of the material, respectively.

Schematic representation of instrumental set up of SSPM represents in figure 1.12. When the phenomenon of SSPM is excited in the nonlinear medium, a phase shift occurs. This happens because the Gaussian light beam experiences varying phase shifts in the radial direction due to differences in the intensity distribution (I). As a result, light waves at two distinct positions with the same wave vector can interfere with each other. The phase shift spectrum reveals two points, r_1 and r_2, with identical slopes (Figure 1.13), satisfying the described relationship.

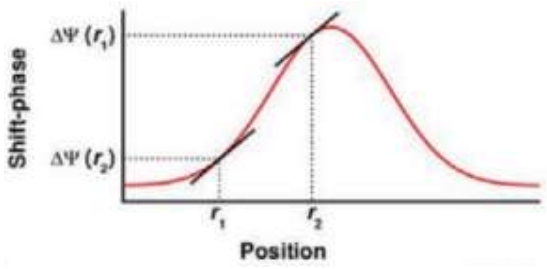

Figure1.13: *Phase shift of gaussian beam with radial coordinate due to the interaction with nonlinear medium*

The phase shift (Δψ(r)) of the incident gaussian laser beam (ψ(r)) has strong dependence upon the n_2 of the material in the SSPM experiment, and it can be expressed by,

$$\Delta\psi(r) = \frac{2\pi n_0}{\lambda}\int_0^{L_{eff}} n_2\, I(r,z)dz$$

Where, r ∈ [0, ∞) is the radial co-ordinate, λ is the wavelength of the incident laser beam and L_{eff} is the effective propagation path passing through the nonlinear medium dispersion. For a Gaussian light beam, the central light intensity (I (0, z)) is twice the value of average light intensity(I). This phase modulation of the output beam is proportional to the incident intensity (I(r,z)) of the laser beam. The diffraction ring number (N) can be expressed as.

$$\Delta\psi(r_1) - \Delta\psi(r_2) = M\pi$$

$$\Delta\psi(0) - \Delta\psi(\infty) = 2\pi N$$

Where M is the integer number, and odd or even value of M corresponds to the dark or bright diffraction pattern, respectively. From the following equation L_{eff} of the laser beam can be determined,

$$L_{eff} = \int_{L_1}^{L_2}(1+\frac{z^2}{z_0^2})^{-1}dz = z_0\, tan^{-1}\left[\frac{z}{z_0}\right]_{L_1}^{L_2}$$

where, $z_0 = \pi\omega_0^2/\lambda$; L_1, L_2 are the distance from the focus (f) to the side of the quartz cuvette; z_0 is the diffraction length, $\omega_0 = 1/e^2$ beam radius. Therefore, the nonlinear refractive index of material can be determined from the formula,

$$n_2 = \frac{\lambda}{2n_0 L_{eff}}\frac{dN}{dI}$$

subsequently, the third order nonlinear susceptibility $\chi^{(3)}_{total}$ of nonlinear materials can be determined as,

$$\chi^{(3)}_{total} = \frac{cn_0^2}{12\pi^2} 10^{-7} n_2 \text{ (esu)}$$

Where c is the velocity of light in free space. In layered material, nonlinear susceptibility of a single layer has a significant role and can be determined by

$$\chi^{(3)}_{total} = \chi^{(3)}_{singlelayer} \times N^2_{eff}$$

Here N_{eff} is the effective number of charge carrier layers present in the material.

1.4.5 Wind-chime model (Origin of SSPM diffraction pattern)

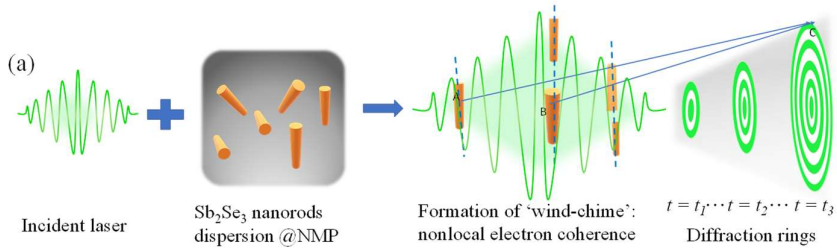

Figure 1.14: *Experimental verification of 'Wind-chime' model: (a). Schematic illustration of 'Wind-Chime model' showing the mechanism of light matter interaction and related diffraction pattern*

When an optical electromagnetic wave with a frequency of 10^{14} Hz (visible range) interacts with a matter local polarization is created. The resulting dipoles oscillate with the same frequency as that of the incident radiation thereby emitting scattered radiation. The intensity of re-radiation is determined by how readily the charged particles oscillate in response to the incoming electromagnetic wave. The primary constraint on these oscillations arises from the material's tendency to restore its electronic distribution to its preferred equilibrium state. However, a balance exists between this restoring force and the extent to which the charged particles can follow the electromagnetic wave. This behaviour is quantitatively characterized by the mobility of the charged particles. During SSPM, the coherence of electrons or holes causes nanorods, nanosheets, or nanoflakes in the nonlinear medium to become

polarized and align with the direction of the external optical field. The schematic of wind-chime model is represented in figure 1.14. The maximum number of rings observed on the screen takes some time to form, as it depends on the completion of the nanoparticles' alignment with the field direction. The time required for aligned most of the nanodomains inside the viscous medium has been presented as

$$T = \frac{\epsilon \pi \eta \xi RC}{1.72(\epsilon - 1)Ih}$$

where ϵ is the relative dielectric constant of material, η is the co-efficient of viscosity of the solvent, ξ is the portion of the fluid globe that rotates with the domain, R is the nanoparticles domain radius, h is the thickness of nanoparticles and I is the laser intensity.

The evolution time of ring formation follows the exponential model as below

$$N = A\left(1 - e^{-\frac{t}{t_c}}\right)$$

Where N is the number of rings, t_c is the rising time for the ring formation and A is a constant.

1.4.6 Nonlinear photonic diode based on SSPM

When a Kerr nonlinear material is illuminated with light of an appropriate wavelength, a diffraction pattern is generated. This behaviour changes when the Kerr material is coupled with a wide-bandgap reverse saturable absorber (RSA) material. In a forward configuration, where the Kerr material is placed before the RSA material, illumination results in a diffraction pattern observed in the far field. However, in the reverse configuration, where the RSA material precedes the Kerr material, no diffraction pattern is observed.

This occurs because, in the reverse configuration, the wide bandgap of the RSA material prevents the incident light from exciting the diffraction pattern. At higher intensities, the RSA material exhibits strong linear absorption, reducing the intensity of light as it exits the material. This reduced intensity falls below the threshold

required to excite the Kerr nonlinear material, thus preventing the formation of a diffraction pattern.

1.4.7 Light-light modulation (optical logic gate)

When two beams of light with different wavelengths meet in free space, they do not interact or exchange energy. However, when these beams intersect in a Kerr material, they interact and generate separate diffraction patterns. Specifically:

- When a high-intensity pump beam (A) interacts with a high-intensity probe beam (B), distinct diffraction patterns appear in the far field
- Similarly, when the pump beam (A) has high intensity and the probe beam (B) has an intensity below a certain threshold, diffraction patterns are still observed in the far field
- However, if both beams have intensities below the threshold, no diffraction pattern is produced in the far field

This interaction effectively demonstrates an OR logic gate behaviour, where the presence of diffraction patterns corresponds to the logic output.

1.5 Desalination

The demand for freshwater is one of the most pressing global challenges. Seawater desalination is widely regarded as a promising solution to address freshwater scarcity. Currently, reverse osmosis and multistage desalination are the most commonly used commercial methods. However, these techniques require expensive infrastructure and consume significant amounts of electricity. In contrast, seawater desalination through interfacial solar evaporation offers a more accessible alternative. This method stands out for its simplicity, as it relies on a straightforward evaporation module and uses sunlight as its sole energy source. The concept of interfacial solar evaporation is crucial. Natural evaporation is typically slow because it occurs only at the water-air interface, where water molecules are in a higher energy state. However, this process is hindered by volumetric heat loss, as heat dissipates throughout the entire volume of water in the reservoir. This results in

a low thermal efficiency, typically around 40%.[8] In interfacial solar evaporation, only the water molecules at the air-liquid interface are heated, resulting in a thermal efficiency of up to 90%.[8] Achieving optimal performance in this process requires the development of advanced photothermal materials and innovations in structural engineering. Heat localization and thermal concentration play pivotal roles in enhancing efficiency. Additionally, water pathway designs—whether 3D, 2D, or 1D—determine the amount of water delivered to the heated zone. [27,28,29] These factors significantly impact the overall performance of interfacial solar evaporation. The performance of interfacial solar evaporation is greatly influenced by the following factors.

1.5.1 Absorption of sunlight and solar light to heat conversion efficiency

High solar absorption across the entire solar spectrum is essential for effective interfacial solar evaporation. To enhance solar evaporation, several state-of-the-art strategies are available which are listed in following.

- Modifying the microstructure of the solar absorber enhances the multiple scattering of incident light, thereby minimizing heat loss from transmission and reflection
- Tuning the band structure of semiconductor absorber materials is another effective approach to capturing sunlight over a broader wavelength range. Narrow bandgap semiconductors produce more heat than wide bandgap semiconductors due to the carrier thermalization process
- The varying sizes and shapes of plasmonic nanoparticles enable broad-spectrum solar absorption, resulting in higher solar light-to-heat conversion efficiency

1.5.2 Heat localization

Heat localization is a critical factor in interfacial solar evaporation,[30] and various methods are available to achieve it.

- To minimize heat loss through the substrate, materials with low thermal conductivity are essential
- To ensure heat localization, the evaporator module includes a thermal insulator that prevents heat loss to the bulk water and helps retain heat in the upper layer of the absorber material

Achieving high solar absorption and heat localization alone is not enough to ensure high solar evaporation efficiency. When high solar absorption and heat localization are combined with efficient water transport pathways, the result is a significant increase in solar-to-water evaporation efficiency.

1.5.3 Different types of water transport pathways

Traditionally, 3D porous interconnected water pathways are used in solar evaporation modules, where capillary forces drive the water supply to the hot zone. However, during water transport, the 3D pores become filled with water, leading to heat loss through conduction to the bulk water, which diminishes the heat localization effect.[27] In contrast, 2D water pathways provide efficient water evaporation while reducing volumetric heat loss to the bulk water.[28] In the evaporation module, the 2D and 1D water pathways are kept separate from the thermal insulator. However, the requirements for these pathways and the thermal insulator are in conflict. The thermal insulator needs a closed porous structure to minimize heat loss to the surrounding water, while the water transport pathways require open pores to ensure efficient and continuous water supply.

In the case of solar desalination, the efficiency of light-to-heat conversion, heat localization and water pathways are all equally crucial.[8]

References

1. Chen C, Li K, Tang J.Solar RRL. 2022,**6**(7),2200094.
2. Ko TY, Shellaiah M, Sun KW. Scientific reports. 2016,**6**(1),35086.
3. Lee H, Yang W, Tan J, Oh Y, Park J, Moon J.ACS Energy Letters. 2019,**4**(5),995-1003.
4. Liu J, Chen Z, Wu C, Yu X, Yu X, Chen C, Li Z, Qiao Q, Cao Y, Zhou Y. Advanced Materials. 2024,**36**(41),2406028.
5. Jeong Y, Song J, Kim H, Park J, Maulana AY, An N, Yun B, Jung S, Park M, Kim J. Journal of Energy Storage. 2024,**92**,112000.
6. Ferriday TB, Middleton PH, Kolhe ML. Energies. 2021,**14**(24),8535.
7. https://www.india.gov.in/spotlight/national-green-hydrogen-mission
8. Chen C, Kuang Y, Hu L.Joule. 2019,**3**(3),683-718.
9. Wu L, Yuan X, Ma D, Zhang Y, Huang W, Ge Y, Song Y, Xiang Y, Li J, Zhang H. Small. 2020,**16**(35),2002252.
10. Mavlonov A, Razykov T, Raziq F, Gan J, Chantana J, Kawano Y, Nishimura T, Wei H, Zakutayev A, Minemoto T, Zu X. Solar Energy. 2020,**201**,227-46.
11. Seh ZW, Kibsgaard J, Dickens CF, Chorkendorff IB, Nørskov JK, Jaramillo TF. Science, 2017,**355**(6321),4998.
12. Wang S, Lu A, Zhong CJ. Nano Convergence. 2021,**8**(1),4.
13. Laursen AB, Varela AS, Dionigi F, Fanchiu H, Miller C, Trinhammer OL, Rossmeisl J, Dahl S. Journal of Chemical Education, 2012, **89**(12), 1595-9.
14. https://en.wikipedia.org/wiki/Butler%E2%80%93Volmer_equation
15. Dickinson EJ, Wain AJ. Journal of Electroanalytical Chemistry, 2020,**872**,114145.
16. C. G. Morales-Guio, L. A. Stern and X. Hu, *Chem. Soc. Rev.*, 2014, **43**(18), 6555–6569
17. Wei J, Zhou M, Long A, Xue Y, Liao H, Wei C, Xu ZJ.Nano-micro letters. 2018,**10**,1-5.
18. Zhao G, Rui K, Dou SX, Sun W. Advanced Functional Materials. 2018,**28**(43),1803291.

19. Meunier V, Huang J, Feng G, Qiao R, Sumpter BG. InASME International Mechanical Engineering Congress and Exposition 2010, **44489**, 21-30.
20. Boyd RW, Gaeta AL, Giese E. Nonlinear optics. InSpringer Handbook of Atomic, Molecular, and Optical Physics 2008 Mar 28 (pp. 1097-1110). Cham: Springer International Publishing.
21. Ghatak AK, Thyagarajan K. Cambridge university press, 1998 Jun 28.
22. Lundstrom M. Science. 2003,**299**(5604),210-1.
23. Wilson J, Hawkes JF. 1989.
24. Davis CC. Cambridge university press, 1996 May 2.
25. Boyd R. Academic Press, 2012.
26. Liao Y, Song C, Xiang Y, Dai X. Annalen der physik. 2020 **532(12),**2000322.
27. Liu H, Chen C, Chen G, Kuang Y, Zhao X, Song J, Jia C, Xu X, Hitz E, Xie H, Wang S. *Advanced Energy Materials,* 2018, **8**, 1701616.
28. Li X, Xu W, Tang M, Zhou L, Zhu B, Zhu S, Zhu J. Proceedings of the National Academy of Sciences. 2016,**113**(49),13953-8.
29. Li Y, Gao T, Yang Z, Chen C, Kuang Y, Song J, Jia C, Hitz EM, Yang B, Hu L. Nano Energy. 2017,**41**,201-9.
30. Ghasemi H, Ni G, Marconnet AM, Loomis J, Yerci S, Miljkovic N, Chen G. Nature communications, 2014,**5**,4449.

Chapter 2

Review of past work

2.1. Sb_2Se_3 Semiconductors for Solar Cell

Every renewable energy sector requires materials that are environmentally friendly, cost-effective, non-toxic and abundantly available on Earth, with the inherent potential to excel in their specific applications. Materials that offer high efficiency for a specific application but are toxic or costly are quickly replaced. This pursuit of better materials in photovoltaics led to the discovery of Sb_2Se_3. Its unique properties, detailed in the previous chapter, have made it a remarkable choice for extensive use in photovoltaics. Thin-film-based solar cells generally come in two distinct configurations: the substrate configuration and the superstrate configuration. In the

substrate configuration, the deposition process begins with the formation of the back contact and concludes with the top transparent electrode layer. Conversely, in the superstrate configuration, the deposition starts with the transparent electrode layer and finishes with the metallic back contact.

The development of Sb_2Se_3 solar cells has a chronological background. The first industrial-scale solar cell, based on silicon, was reported with an impressive efficiency of 26.7%.[1] Although Si offers high efficiency and several benefits, its potential is hindered by significant drawbacks. These include a high fabrication temperature of 1400°C and a low absorption coefficient, which requires a thickness of several hundred micrometres to adequately absorb sunlight. As a result, researchers are increasingly investigating alternative absorber materials for solar cells. GaAs (efficiency ≈ 29.1%) and Cu (In, Ga) (S, Se) $_2$ (efficiency ≈ 23.4%) were introduced, but their primary drawbacks are scarcity and high costs.[1] Following these, CdTe was developed, offering a simple phase and suitable bandgap, but concerns arose due to its toxicity. Subsequently, the non-toxic and low-cost $Cu_2ZnSn(S,Se)_4$ emerged, demonstrating an efficiency of 9.6%[1]. Later, hybrid perovskites gained attention as promising photovoltaic (PV) materials, though issues with instability and toxicity remained significant challenges. This historical progression sets the stage for 2013, which marked the emergence of Sb_2Se_3 as a potential game-changer. The performance of a solar cell is influenced not only by the absorber layer but also by the hole transport layer, electron transport layer, back contact and buffer layer. The chronological development of Sb_2Se_3 solar cells is illustrated in table 2.1.

Table 2.1: The chronological development of Sb_2Se_3 solar cells

Sb_2Se_3 solar cells description	Deposition method	Efficiency	Year	References
First sensitized type Sb_2Se_3 solar cell	Spin coating	3.21 %	2013 Dec	[2]
First planar type Sb_2Se_3 solar cell	Hydrazine solution process	2.26 %	2014 Feb	[3]
planar type Sb_2Se_3 solar cell	Thermal evaporation process	1.9 %	2014 Apr	[4]
Benign grain boundary oriented polycrystalline Sb_2Se_3 solar cell	Rapid Thermal evaporation process	5.6 %	2015 Jun	[5]
Orientation control of Sb_2Se_3 induced by ZnO buffer layer	Rapid thermal evaporation process	5.93 %	2017 Mar	[6]
Sb_2Se_3 film	Closed spaced sublimation	4.3 %	2017 Jun	[7]
Sb_2Se_3 film	Vapor transport	7.6 %	2018 Jun	[8]
Nanorods array Sb_2Se_3	Device structure	9.2 %	2019 Jan	[9]
Improved selenization of Sb_2Se_3	Selenization method	6.84 %	2019 Apr	[10]
Sb_2Se_3 mini module	Flexible solar cells	6.13 %	2021 May	[11]

2.2. Sb_2Se_3 Semiconductors for Thermoelectric Applications

Thermoelectric materials convert temperature gradients into electricity, and Sb_2Se_3 shows promise in this area too:

- High Seebeck Coefficient:

  Sb_2Se_3 demonstrates a significant voltage response to temperature differences, crucial for efficient thermoelectric performance

- Low Thermal Conductivity:

  Its low thermal conductivity ensures heat retention at the junctions, enhancing thermoelectric efficiency

- Bandgap Tunability:

  Slight adjustments in its composition can optimize its thermoelectric properties

Ting et al. [12] reported that the thermal conductivity of a single Sb_2Se_3 nanowire with a diameter of 680 nm is $0.037 \pm 0.002\ W/m.K$. Their findings also revealed that the thermal conductivity of the nanowire is over an order of magnitude lower than that of bulk Sb_2Se_3. Additionally, the nanowire exhibited a Seebeck coefficient of 750 μV/K [12]. Moreover, the electrical conductivity of Sb_2Se_3 improved significantly when combined with β-Cu_2Se and PANI (polyaniline), with the β-Cu_2Se/PANI composite achieving the highest power factor of 181.61 $\mu W/m \cdot K^2$ at 473 K [13]. A remarkable figure of merit (ZT) value of 0.38 at room temperature has been achieved through the atomic layer deposition of Sb_2Te_3- Sb_2Se_3 nanostructures [14]. This research offers important insights into the design and development of high-

performance chalcogenide materials. Numerous studies have explored the use of Sb_2Se_3 in photoelectrochemical applications, photodetectors and integrated photonic devices. However, certain areas, such as the hydrogen evolution reaction (HER), desalination and nonlinear optics, remain underexplored for Sb_2Se_3. Despite this, extensive research exists in these fields and some of the key studies are highlighted below.

2.3. Hydrogen evolution reaction (HER)

Hydrogen is a highly efficient, clean and economical energy source due to its impressive gravimetric energy density and a lower heating value of 120 kJ/g [15]. For the reasons mentioned above, three primary technologies are available for producing hydrogen safely and on a large scale:

(a) Coal gasification

(b) Water electrolysis

(c) Methane reforming

Among these, only water electrolysis is entirely green and free of CO_2 emissions.

The hydrogen evolution reaction in electrocatalysis is inherently slow, requiring the use of efficient catalysts to enhance the reaction's kinetics and improve the efficiency of water electrolysis. For efficient hydrogen production that is both economically viable and suitable for large-scale applications, the catalyst must meet the following criteria:

1. Cost-effectiveness

   (a) Use low-cost materials with abundant availability on Earth.

   (b) Ensure low fabrication costs for the photocathode.

2. High efficiency and minimal overpotential

   (a) Exhibit high electrical conductivity.

   (b) Minimize the charge diffusion path length.

   (c) Provide a large active surface area.

   (d) Deliver high current density at low overpotential.

   (e) Have active sites with Gibbs free energy values close to zero for optimal performance.

3. Durability

   (a) Maintain high chemical stability in harsh acidic and alkaline environments.

Platinum is the most efficient noble-metal-based electrocatalyst, known for achieving high current density at low overpotential. However, its limited availability and high cost restrict its widespread use as a catalyst for the hydrogen evolution reaction (HER).

2.3.1. Work done on various types of electrocatalysts

Although electrolysis of water for the production of hydrogen is known and used over centuries, finding an appropriate catalyst with desirable attributes is a very active field of research over the last three decades. The catalysts can be broadly

categorized into two sections: (i) Non-metal based electrocatalysts and (ii) Metal based electrocatalysts.

2.3.1.1 Non-metal based electrocatalysts:

Metal-free electrocatalysts are widely utilized due to their tunable structures, diverse compositions, low cost, eco-friendliness and abundance on Earth. Among these, carbon-based materials are particularly prominent and widely recognized for their effectiveness as electrocatalysts. Zero-dimensional (0D) fullerenes (C60) exhibit notable electrochemical electron-accepting ability and efficient electron transport properties. [16] In 0D materials, carbon quantum dots (CQD) enhance performance by offering a large surface area, improved conductivity and excellent dispersibility. [17,18] N-doped carbon quantum dots (N-CQDs) have demonstrated an overpotential value of 341 mV in reported studies. [19] One-dimensional (1D) carbon nanotubes have been shown to exhibit excellent electrochemical activity (0.29 V) and remarkable stability in electrocatalysis, even after 10,000 cycles. [20,21] Two-dimensional (2D) carbonaceous materials like graphene meet all the essential criteria for an effective catalyst, including excellent conductivity, a large surface area, high stability and strong corrosion resistance. However, surprisingly, graphene's electrocatalytic activity is relatively poor. This limitation arises because graphene layers are chemically inert due to the uniform charge distribution of sp^2 carbon atoms in the basal plane and the absence of efficient charge transfer sites. Graphene can display electrochemical activity when its layers are bent, causing a shift in charge distribution. Techniques such as nitrogen (N) doping, [22,23] introducing double-defect structures [24] and heteroatom doping [25] can effectively modify

graphene's electronic structure, thereby enhancing its electrocatalytic performance for the hydrogen evolution reaction (HER). Boron carbon nitride is another notable metal-free catalyst used in electrocatalysis, making a significant impact on hydrogen evolution reaction (HER). While non-metal-based catalysts are eco-friendly and cost-effective, metal-based catalysts continue to dominate for large-scale hydrogen production.

2.3.1.2 Metal based electrocatalysts:

According to the Sabatier principle, an ideal catalyst for the hydrogen evolution reaction (HER) should have a ΔG_H value of zero. In 1957, Parsons demonstrated that catalyst surfaces with ΔG_H close to zero exhibit high activity for HER. Metals such as Pt, Rh, Re and Ir, which are positioned near the peak of the HER volcano plot, provide optimal hydrogen atom binding energies, making them highly effective for this reaction. Platinum is renowned for superior catalyst for H_2 production. The primary challenge in hydrogen production is its high cost. Ruthenium (Ru) emerges as a practical alternative to platinum (Pt) because it is more affordable while maintaining a comparable metal-hydrogen bond strength of 65 kcal/mol, similar to that of Pt[26].The Ru@C_2N catalyst in 0.5 M H_2SO_4 demonstrates an impressively low overpotential of 22 mV at a current density of 10 mA/cm², outperforming other catalysts such as Co@C_2N (290 mV), Ni@C_2N (410 mV), Pd@C_2N (330 mV) and even Pt@C_2N (60 mV)[26] . Surprisingly, Ru@C_2N exhibits higher activity even in an alkaline solution, with a low overpotential of 17 mV at a current density of 10 mA/cm². Theoretically, Ni @Ni_2P-Ru achieves an optimal Gibbs free energy (ΔG_H) of 0.01 eV. Experimentally, it demonstrates overpotentials of 51 mV and 41 mV

(10mA/cm^2) in acidic and alkaline electrolytes, respectively.[27] In comparison to the Pt (100) facet, the Ir (111) facet presents another viable option with a relatively balanced hydrogen adsorption/desorption capacity. Additionally, it offers better stability than platinum.[28] Metals have traditionally been regarded as effective electrocatalysts. However, they face several challenges, including high costs, instability, a tendency for metal-based catalysts to agglomerate easily and limited resource availability. To address these various drawbacks of using metals as catalysts, metal nanoclusters (MNCs) have been developed. These clusters, composed of several to hundreds of metal atoms, are characterized by sizes comparable to the Fermi wavelength of electrons, typically less than 2.0 nm. Metal nanoclusters (MNCs) provide several advantages, including higher surface energy, which helps overcome the potential energy barrier, thereby requiring a lower overpotential. Additionally, they enable efficient atom utilization, minimizing the need for large quantities of noble metals. The quantum size effect of metal nanoclusters imparts distinctive electronic properties, significantly enhancing their functionality. Numerous studies have reported the application of metal nanoclusters in hydrogen evolution reactions, including Pd-Ru MNC [29], Ni-Fe MNC [30], clusters of Cu, Co, Ni, Pd and Pt[31], Pt-Cu clusters[32], Pt clusters on F-doped SnO_2 [33],Pt clusters on MoO_2[34] and Pt clusters on $Ti_3C_2T_x$[35], among others. Significant progress has been achieved in the research on MNCs; however, challenges remain in their application to hydrogen evolution reactions (HER). In practice, MNCs tend to agglomerate during experiments. Furthermore, advanced characterization techniques, such as in-situ Raman spectroscopy and X-ray Absorption Fine Structure

(XAFS), are needed to identify active centres. However, the limited accessibility of these tools poses technological constraints. Traditionally the transition metals are good electrocatalysts. However, they have the following limitations:

With the advent of Nanotechnology significant improvement of catalysts performance have been found. Transition metal-based chalcogenides and their nanostructures are found to exhibit improved catalysis performance.

With the advent of 2D materials significantly improved performance of electrocatalysts for HER applications have been found. These include MoS_2, $MoSe_2$, etc. Also alloys of 2D transition metal chalcogenides and their composites are important members of electrocatalysts family for HER applications.

2.3.2 2D metal dichalcogenides as electrocatalyst in (HER)

In recent years, numerous alternatives to platinum-based electrocatalysts have been explored, with MoS_2 gaining significant attention. Its abundance, high catalytic activity and potential have led to the development of various MoS_2-based electrocatalysts. Additionally, due to its anisotropic nature, MoS_2 tends to form a two-dimensional structure, providing a large surface area that is advantageous for the hydrogen evolution reaction (HER).

Xie et al. used ultrathin MoS_2 nanosheets for enhanced HER by introducing controlled disorder and oxygen incorporation [36]. The disordered structure created abundant active sulfur sites, while oxygen incorporation improved electronic structure and conductivity. The modified catalyst achieved low overpotential (120

mV), high current density and excellent stability.[36] Reducing the layer number of MoS_2 significantly enhances its catalytic activity for the hydrogen evolution reaction (HER), as shown by Yifei et al. They found that adding a single layer decreases catalytic activity by a factor of 4.47, attributed to improved vertical electron hopping. This study challenges the conventional belief that only edge sites are catalytically active in MoS_2, demonstrating that basal plane atoms can also serve as active sites. The reported Tafel slope for this activity is 140 mV dec^{-1}. [37] Li et al. have also optimized and activated the basal plane of the monolayer 2H-MoS_2 for hydrogen evolution reaction (HER) by introducing sulfur vacancies. Here onset potential is 170 mV and Tafel slope is 60 mV dec^{-1}.[38] Voiry et al. [39] enhanced the electrocatalytic activity of the 2H monolayer MoS_2 by improving the coupling between the substrate and the catalyst. Zhang et al. synthesized a uniform, centimetre-scale dendritic monolayer of MoS_2 on the insulator $SrTiO_3$. This monolayer was successfully transferred onto a gold foil electrode, where it served as an excellent electrocatalyst for the hydrogen evolution reaction, demonstrating a low Tafel slope of 73 mV dec^{-1}.[40] Additional studies on 2D metal dichalcogenides as catalysts for hydrogen evolution reaction (HER) are available, and their performance is summarized in the table 2.2 below.

Table 2.2: 2D metal dichalcogenides as catalysts for hydrogen evolution reaction

Materials	Electrolyte	Current density (mA/cm^2)	Overpotential (mV)	Tafel slope(mV/dec)	Reference
1.$Co_{0.85}Se$/graphene	0.5 M H_2SO_4	10	250	41.8	[41]
2. Co_9S_8	0.5 M H_2SO_4	10	149	70	[42]
3. CoS_2	0.5 M H_2SO_4	10	197	29.9	[43]
4. CoS_2/ CoSe @C	0.5 M H_2SO_4	10	164	42	[44]
5. $CoSe_2/MoSe_2$	0.5 M H_2SO_4	10	218	76	[45]
6.VS_2	0.5 M H_2SO_4	10	-	159	[46]
7. WS_2	0.5 M H_2SO_4	10	130	45	[47]
8.V doped WS_2	0.5 M H_2SO_4	10	148	71	[48]
9.TaS_2	0.5 M H_2SO_4	10	200	135	[49]
10. TaS_2, $TaSe_2$	0.5 M H_2SO_4	10	120	-	[50]
11. MoS_2- WS_2	0.5 M H_2SO_4	10	129	72	[51]
12.$Ni_{0.85}Se$/ $MoSe_2$	1M KOH	10	108	77	[52]
13. NiS@ MoS_2	1M KOH	10	208	62.4	[53]
14. Ni_3S_2- NiS	1M KOH	10	141	75	[54]
15. MoS_2/ Ni_3S_2	1M KOH	10	110	83.1	[55]
16. MoS_2/ MoO_2	0.5 M H_2SO_4	10	300	35.6	[56]
17.$Fe_{1-x}Co_xSe_2$/rGO	0.5 M H_2SO_4	10	166	36	[57]
18. $MoSe_2$	0.5 M H_2SO_4	10	250	59.8	[58]
19. $MoSe_2$	0.5 M H_2SO_4	10	150	80	[59]
20. $MoSe_2$	0.5 M H_2SO_4	10	102	53	[60]

2.3.3 Heterostructures of different materials with rGO as electrocatalyst in (HER)

Dong et al. [61] demonstrated that defective MoS_2/rGO heterostructures exhibited excellent HER activity, with a low overpotential of 154.77 mV and a small Tafel slope of 56.17 mV/dec.[61] On the other hand, the van der Waals heterostructure of rGO and hBN also displayed overpotential of 220 mV.[62] The electrocatalytic hydrogen evolution reaction was further enhanced by MoS_2/rGO heterostructures combined with Cu_2ZnSnS_4, achieving a low overpotential of 50 mV at 10 mA/cm² and a Tafel slope of 68 mV/dec.[63] An exceptionally low overpotential of 76.3 mV has also been achieved using CoS/rGO@carbon cloth as a catalyst for HER.[64]

2.3.4 Sb_2Se_3 as *electrocatalyst in (HER)*

Reports on Sb_2Se_3 as an electrocatalyst for HER are scarce. One example, Sb_2Se_3/polyacrylonitrile, demonstrated an overpotential of 152 mV and a Tafel slope of 78.4 mV/dec. [65] N, Ru, Co doped Sb_2S_3 also shows excellent HER activity (72 mV at 10 mA/cm²).[66]

2.4. Spatial-Self phase modulation (SSPM)

In self-induced spatial phase modulation (SSPM), materials play a critical role. Achieving a diffraction pattern in the far field requires both a high-intensity laser and materials with significant third-order nonlinear susceptibility. The following table 2.3 presents some reported materials along with their corresponding third-order nonlinear susceptibility values.

Table 2.3: Third order optical susceptibilities of reported materials.

Materials	Dimensions	Solvent	Concentrations	Laser parameters	$X^{(3)}_{monolayer}$	References
$MoSe_2$	2D	NMP	$7.1*10^{-4}$ mol/L	532 nm CW Laser	10^{-9} esu	[67]
MoS_2	2D	Acetone	0.14 g/L	532 nm CW Laser,400 nm and 800 nm ultrafast lasers	10^{-9} esu	[68]
$MoTe_2$	2D	NMP	0.1 g/L	473 nm 532 nm, 750 nm and 801 nm CW Lasers	10^{-9} esu	[69]
Black phosphorus	2D	NMP	$4.03*10^{-3}$ mol/L	350- 1160 nm femtosecond Lasers	10^{-8} esu at multiple wavelengths	[70]
Graphite	3D	NMP	0.075 mg/L	532 nm CW Laser	$2.2*10^{-9}$ esu	[71]
Graphene	2D	NMP	-	532 nm CW Laser	10^{-7} esu	[72]
$Ti_3C_2T_x$	2D	-	-	800 nm femtosecond Laser and 1064 nm picosecond Laser	10^{-15} esu at 800 nm and 10^{-7} esu at 1064 nm	[73]
TaAS	3D	NMP	0.2 g/L	532 nm laser	$9.9*10^{-9}$ esu	[74]
Te NTs	1D	-	0.25 mg/mL	532 nm laser	-	[75]
Te@ BiQDNTs	1D@0D	-	0.25 mg/mL	532 nm laser	-	[75]

2.5. Review of past work on desalination

Solar evaporation is one of the oldest methods of harnessing solar energy to heat water. Traditionally, the entire volume of water is heated, but since evaporation occurs only at the surface, this approach results in a low thermal efficiency of around 40%. In contrast, interfacial solar evaporation focuses on heating just the surface layer of water, where evaporation takes place. This targeted approach significantly improves thermal efficiency, reaching levels as high as 90%. Solar evaporation is gaining prominence in various emerging fields such as contaminated water purification, seawater desalination and electricity generation. For these applications, materials with high light-to-heat conversion efficiency are essential.

Interfacial solar evaporation is a potential technique in which solar energy can be utilized for evaporation of brine water which has utilization in desalination purposes.[76] Various types of photothermal materials are available, including plasmonic materials, semiconductors and carbon-based materials. The following graph highlights some of these materials along with their efficiencies and key characteristics.

2.5.1 Work done on carbon-based materials:

Carbon-based materials are widely utilized as photothermal materials due to their high light absorption over a broad wavelength range, affordability and ability to convert absorbed light into heat energy. This process occurs when electrons are excited from the π orbital to the π* orbital under external stimulation. As the excited electrons relax back to the ground state, heat is generated. In various interfacial solar

evaporation module graphene [77-84] graphene oxide/ reduced graphene oxide [85,86,87,88], Carbon nanotubes (CNTs)[89-91], graphite[92-94], carbon black[95], are used as photothermal materials.

2.5.2 Work done utilising semiconductor materials

In semiconductors, electron-hole pairs are generated when energy above the bandgap is absorbed. These pairs subsequently relax to the band edges, releasing energy as heat through thermalization processes. Some semiconductors like black titania [96], Ti_2O_3 nanoparticles [97], Fe_3O_4, $MnFe_2O_4$,[98] serves as a potential candidate for light to heat conversion.

2.5.3 Work done utilising other type/ composite materials

Some metal nanoparticles demonstrate strong light absorption and efficient light-to-heat conversion through plasmonic resonance. Gold (Au) plasmonic nanoparticles are particularly effective at converting light into heat energy [99-105]

The efficiency of an interfacial solar evaporation system is primarily influenced by factors such as the choice of solar absorber materials, supporting substrates, structural design techniques, water transport pathways, surface wettability and effective heat localization. Selecting appropriate materials for solar light absorption and heat localization is particularly crucial. Generally, there are three main mechanisms for photothermal heat generation: molecular thermal vibrations, electron-hole pair generation and relaxation and localized plasmonic heating.

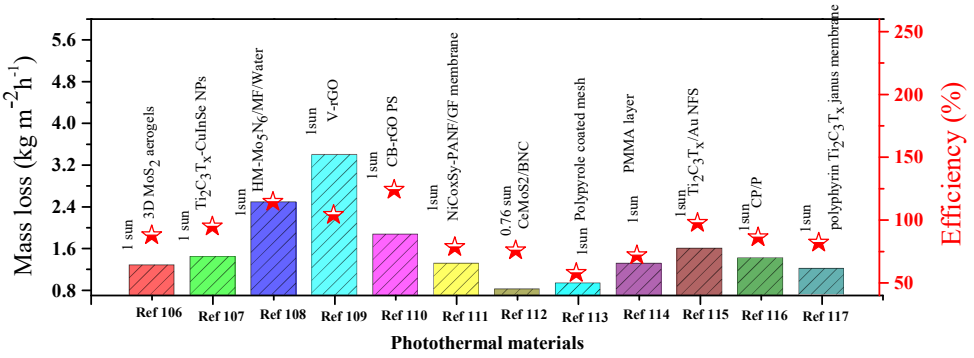

Figure 2.1. *Mass loss and efficiency of several composite photothermal materials*

2.6 Objective of the Thesis

To achieve a sustainable and high-speed communication future, it is vital to harness renewable and green energy resources, along with the development of all-optical diodes and logic gates. It is now time to transition from the fossil fuel era to the renewable energy era and from the electronic age to the photonic age. In this shift, hydrogen evolution reactions (HER), desalination and nonlinear optics have become critical areas of focus. However, the primary challenge lies in overcoming the materials bottleneck. In this context, Sb_2Se_3 nanostructures have emerged as leading candidates due to their ability to harness significant solar energy, their economic feasibility and their low toxicity. Despite these advantages, Sb_2Se_3 nanostructures remain underexplored for applications in HER, desalination and nonlinear optics. Motivated by these gaps, the key objectives of this thesis are:

1. To synthesize the specific nanomaterials by easy, scalable and economically viable routes. This will primarily include

- Synthesis of Sb_2Se_3 NRs by easy solvothermal technique and also

  to develop controlled synthesis of 2D materials like reduced graphene oxide (rGO) and SnS_2 which will be required for modifying the Sb_2Se_3 nanostructures

2. To characterize the synthesize nanostructures: this will include
    - Morphological characterization
    - Structural characterizations
    - Compositional characterizations and optical characterizations
3. To investigate the efficacy of Sb_2Se_3 NRs for as electrocatalyst for HER applications and also finding ways to improve its performance
4. Investigation on the light to heat conversion efficiency using Sb_2Se_3 NRs
5. Investigation on the desalination performance of Sb_2Se_3 NRs
6. One of the major aims of the thesis is to investigate the nonlinear optical properties of Sb_2Se_3 NRs through spatial self-phase modulation

2.7 Organization of the Thesis

The thesis is divided into seven chapters, and a concise overview of each chapter is provided below.

Chapter 1: Introduction

This chapter explores various advantageous properties of antimony selenide, including its optical and electronic characteristics. It emphasizes the importance of

renewable energy infrastructure, with a special focus on electrocatalytic hydrogen evolution reactions (HER) as a key solution to future energy challenges. The chapter also provides a concise explanation of concepts closely related to HER, such as the thermodynamic potential for water electrolysis, the role of electrocatalysts in HER, onset potential and overpotential, the Sabatier principle, the current-voltage relationship, reaction kinetics and electrochemical double-layer capacitance. Furthermore, it discusses the critical role of desalination in ensuring potable water, heat localization and various water diffusion pathways. Additionally, the chapter offers insights into light-matter interactions, the origins of optical nonlinearity in materials, the optical Kerr effect, an introduction to spatial self-phase modulation (SSPM), nonlinear photonic diodes and optical logic gates.

Chapter 2: Review of past work

This chapter offers a succinct review of the crucial role of antimony selenide in solar cells, thermoelectric systems and photoelectrochemical applications. It also discusses previous research on HER, desalination and SSPM across various materials.

Chapter 3: Experimental Details

This chapter explores the various methods used to fabricate different semiconductor nanostructures and the range of characterization techniques applied to analyse their diverse properties.

Chapter 4: Tailoring the Sb_2Se_3/rGO heterointerfaces for modulation of electrocatalytic hydrogen evolution performances in acidic media

The chapter discusses the development of Sb_2Se_3/rGO electrocatalyst for improved hydrogen evolution reaction.

Chapter 5: Strong non-linear optical response of Sb_2Se_3 nanorods suspension based on spatial self-phase modulation and their all-optical photonic device applications

This chapter investigates the nonlinear optical phenomena in Sb_2Se_3 using the spatial self-phase modulation (SSPM) technique and determines the third-order nonlinear susceptibility of Sb_2Se_3.

Chapter 6: Efficient light to heat conversion in Sb_2Se_3 nanorods and the role of macro-channel imprinted Sb_2Se_3 loaded hybrid membrane for superior desalination performance

This study showcases the efficient light-to-heat conversion capabilities of Sb_2Se_3 for red (671 nm) and green (532 nm) lasers, as demonstrated through customized water droplet experiments. Additionally, hybrid PVDF(M)/Sb_2Se_3 NRs membranes were designed for solar desalination applications.

Chapter 7: Conclusion of the thesis

This chapter presents the overall conclusions of the research work.

References

1. Chen C, Li K, Tang J. 2022, **6**, 2200094.
2. Choi YC, Mandal TN, Yang WS, Lee YH, Im SH, Noh JH, Seok SI. Angew. Chem. 2014, **126**, 1353-7.
3. Y. Zhou, M. Leng, Z. Xia, J. Zhong, H. Song, X. Liu, B. Yang, J. Zhang, J. Chen, K. Zhou, J. Han, Y. Cheng, J. Tang, Adv. Energy Mater. 2014, **4**, 1301846.
4. M. Luo, M. Y. Leng, X. S. Liu, J. Chen, C. Chen, S. K. Qin, J. Tang, Appl. Phys. Lett. 2014, **104**, 173904.
5. Y. Zhou, L. Wang, S. Chen, S. Qin, X. Liu, J. Chen, D.-J. Xue, M. Luo, Y. Cao, Y. Cheng, E. H. Sargent, J. Tang, Nat. Photonics 2015, **9**, 409.
6. L. Wang, D. B. Li, K. H. Li, C. Chen, H. X. Deng, L. Gao, Y. Zhao, F. Jiang, L. Y. Li, F. Huang, Y. S. He, H. S. Song, G. D. Niu, J. Tang, Nat. Energy 2017, **2**, 17046.
7. L. J. Phillips, P. Yates, O. S. Hutter, T. Baines, L. Bowen, K. Durose, J. D. Major, presented at IEEE 44th Photovoltaic Specialist Conf., Washington, DC, June, 2017.
8. X. Wen, C. Chen, S. Lu, K. Li, R. Kondrotas, Y. Zhao, W. Chen, L. Gao, C. Wang, J. Zhang, G. Niu, J. Tang, Nat. Commun. 2018, **9**, 2179.
9. Z. Li, X. Liang, G. Li, H. Liu, H. Zhang, J. Guo, J. Chen, K. Shen, X. San, W. Yu, Nat. Commun. 2019, **10**, 125

10. G.-X. Liang, Y.-D. Luo, S. Chen, R. Tang, Z.-H. Zheng, X.-J. Li, X.-S. Liu, Y.-K. Liu, Y.-F. Li, X.-Y. Chen, Z.-H. Su, X.-H. Zhang, H.-L. Ma, P. Fan, Nano Energy 2020, **73**, 104806.
11. K. Li, F. Li, C. Chen, P. Jiang, S. Lu, S. Wang, Y. Lu, G. Tu, J. Guo, L. Shui, Z. Liu, B. Song, J. Tang, Nano Energy 2021, **86**, 106101.
12. Ko TY, Shellaiah M, Sun KW. 2016, **6**, 135086.
13. Kim M, Park D, Kim J. 2021, **13**, 1518.
14. Yang J, Daqiqshirazi M, Ritschel T, Bahrami A, Lehmann S, Wolf D, Feng W, Pöhl A, Charvot J, Bureš F, Brumme T. ACS Nano 2024, **18**, 17500-8.
15. Mondal A, Vomiero A. Adv. Func. Mater. 2022, **32**, 2208994.
16. T. Xu, W. Shen, W. Huang, X. Lu, et al., Mater. Today Nano 2020,**11** 100081.
17. X. Wang, Y. Feng, P. Dong, J. Huang, et al., Front. Chem. 2019, **7**, 671.
18. J. Yu, H. Song, X. Li, L. Tang, Z. Tang, et al., Adv. Func. Mater. 2021,**31,** 2107196.
19. Y. Liu, N. Ye, X. Li, X. Li, H. Liu, et al., J. Solid State Chem. 2021,**293**, 121781.
20. L. Dai, D.W. Chang, J.-B. Baek, W. Lu, et al., Small 2012, **8**, 1130–1166.
21. J. Han, C. Gong, C. He, P. He, J. Zhang, et al., J. Mater. Chem. A 2022, **10,**16403–16408.
22. D. Zhang, F. Wang, X. Fan, W. Zhao, M. Cui, et al., Carbon 2022, **187,** 386–395
23. Y. Li, Y. Luo, Z. Zhang, Q. Yu, C. Li, et al., Carbon 2021,**183,** 362–367.

24. Y.-L. Wang, G.-Q. Sun, L.-H. Chen, Z.-K. Du, X.-Y. Li, et al., Appl. Surf. Sci. 2021, **566,** 150712.
25. H. Li, B. Ren, W. Liu, L. Jing, R.Y. Tay, et al., Nano Energy 2021, **88,** 106246.
26. Mahmood, J.; Li, F.; Jung, S.-M.; Okyay, M. S.; Ahmad, I.; Kim, S.-J.; Park, N.; Jeong, H. Y.; Baek, J.-B. Nat. Nanotechnol. 2017, **12**, 441-446.
27. Liu, Y.; Liu, S.; Wang, Y.; Zhang, Q.; Gu, L.; Zhao, S.; Xu, D.; Li, Y.; Bao, J.; Dai, Z. J. Am. Chem. Soc. 2018, **140**, 2731-2734.
28. Engstrom, J. R.; Tsai, W.; Weinberg, W. H. J. Chem. Phys. 1987, **87**, 3104-3119
29. S. Liu, Q. Zhang, J. Bao, Y. Li, Z. Dai, L. Gu, *Chem. Eur. J.* 2017, **23**, 18203.
30. S. Xue, R. W. Haid, R. M. Kluge, X. Ding, B. Garlyyev, J. Fichtner, S. Watzele, S. Hou, A. S. Bandarenka, *Angew. Chem., Int. Ed.* 2020, **59**, 10934.
31. B. Zhang, Y. Zhang, M. Hou, W. Wang, S. Hu, W. Cen, X. Cao, S. Qiao, B.-H. Han, *J. Mater. Chem. A* 2021, **9**, 10146.
32. M. C. Spadaro, J. J. L. Humphrey, R. Cai, L. Martinez, S. J. Haigh, Y. Huttel, S. J. Spencer, A. J. Wain, R. Palmer, *J. Phys. Chem. C* 2020, **124**, 23683.
33. T. Kim, S. B. Roy, S. Moon, S. Yoo, H. Choi, V. G. Parale, Y. Kim, J. Lee, S. C. Jun, K. Kang, S.-H. Chun, K. Kanamori, H.-H. Park, *ACS Nano* 2022, **16**, 1625.

34. X. Li, J. Yu, J. Jia, A. Wang, L. Zhao, T. Xiong, H. Liu, W. Zhou, *Nano Energy* 2019, **62**, 127
35. Y. Wu, W. Wei, R. Yu, L. Xia, X. Hong, J. Zhu, J. Li, L. Lv, W. Chen, Y. Zhao, L. Zhou, L. Mai, *Adv. Func. Mater.* 2022, **32**, 2110910.
36. Junfeng Xie, Jiajia Zhang, Shuang Li, Fabian Grote, Xiaodong Zhang, Hao Zhang, Ruoxing Wang, Yong Lei, Bicai Pan, and Yi Xie *J. Am. Chem. Soc.* 2013, **135**, 17881-17888.
37. Yifei Yu, Sheng-Yang Huang, Yanpeng Li, Stephan N. Steinmann, Weitao Yang, and Linyou Cao *Nano Lett.* 2014, **14**, 553-558.
38. Li, H., Tsai, C., Koh, A. *et al. Nat. Mater.* 2016, **15**, 48–53
39. Voiry, D., Fullon, R., Yang, J. *et al. Nat. Mater.* 2016, **15**, 1003–1009.
40. Yu Zhang, Qingqing Ji, Gao-Feng Han, Jing Ju, Jianping Shi, Donglin Ma, Jingyu Sun, Yanshuo Zhang, Minjie Li, Xing-You Lang, Yanfeng Zhang, and Zhongfan Liu. *ACS Nano* 2014, **8** (8), 8617-8624.
41. B. Yu, F. Qi, Y. Chen, X. Wang, B. Zheng, W. Zhang, Y. Li, L.-C. Zhang, *ACS Appl. Mater. Interfaces* 2017, **9**, 30703.
42. J. Mujtaba, L. He, H. Zhu, Z. Xiao, G. Huang, A. A. Solovev, Y. Mei, *ACS Appl. Nano Mater.* 2021, **4**, 1776.
43. S. Y. Shajaripour Jaberi, A. Ghaffarinejad, Z. Khajehsaeidi, *Int. J. Hydrogen Energy* 2021, **46**, 3922.

44. K. Karuppasamy, R. Bose, V. R. Jothi, D. Vikraman, Y.-T. Jeong, P. Arunkumar, D. B. Velusamy, T. Maiyalagan, A. Alfantazi, H.-S. Kim, *J. Alloys Compd.* 2020, **838**, 155537.
45. G. Zhao, P. Li, K. Rui, Y. Chen, S. X. Dou, W. Sun, *Chem. Eur. J.* 2018, **24**, 11158.
46. X. Chia, A. Ambrosi, P. Lazar, Z. Sofer, M. Pumera, *J. Mater. Chem. A* 2016, **4**, 14241.
47. A. K. Nayak, E. Enhtuwshin, S. J. Kim, H. Han, *Catalysts* 2020, **10**, 1238.
48. A. Jiang, B. Zhang, Z. Li, G. Jin, J. Hao, *Chem. Asian J.*2018, **13**, 1438.
49. H. Li, Y. Tan, P. Liu, C. Guo, M. Luo, J. Han, T. Lin, F. Huang, M. Chen, *Adv. Mater.* 2016, **28**, 8945.
50. L. Najafi, S. Bellani, R. Oropesa-Nuñez, B. Martín-García, M. Prato, L. Pasquale, J.-K. Panda, P. Marvan, Z. Sofer, F. Bonaccorso, *ACS Catal.* 2020, **10**, 3313.
51. D. Vikraman, S. Hussain, K. Akbar, L. Truong, A. Kathalingam, S.-H. Chun, J. Jung, H. J. Park, H.-S. Kim, *ACS Sustainable Chem. Eng.* 2018, **6**, 8400.
52. H. R. Inta, S. Ghosh, A. Mondal, G. Tudu, H. V. S. R. M. Koppisetti, V. Mahalingam, *ACS Appl. Energy Mater.* 2021, **4**, 2828.
53. Z. Chen, X. Liu, P. Xin, H. Wang, Y. Wu, C. Gao, Q. He, Y. Jiang, Z. Hu, S. Huang, *J. Alloys Compd.* 2021, **853**, 157352.
54. B. Zhou, J. Li, X. Zhang, J. Guo, *J. Alloys Compd.* 2021, **862**, 158391.

55. J. Zhang, T. Wang, D. Pohl, B. Rellinghaus, R. Dong, S. Liu, X. Zhuang, X. Feng, *Angew. Chem.* 2016, **128**, 6814.
56. R. D. Nikam, A.-Y. Lu, P. A. Sonawane, U. R. Kumar, K. Yadav, L.-J. Li, Y.-T. Chen, *ACS Appl. Mater. Interfaces* 2015, **7**, 23328.
57. X. Xu, Y. Ge, M. Wang, Z. Zhang, P. Dong, R. Baines, M. Ye, J. Shen, *ACS Appl. Mater. Interfaces* 2016, **8**, 18036.
58. H. Wang, D. Kong, P. Johanes, J. J. Cha, G. Zheng, K. Yan, N. Liu, Y. Cui, *Nano Lett.* 2013, **13**, 3426.
59. Z. Lei, S. Xu, P. Wu, *Phys. Chem. Chem. Phys.* 2016, **18**, 70.
60. B. Qu, C. Li, C. Zhu, S. Wang, X. Zhang, Y. Chen, *Nanoscale* 2016, **8**, 16886.
61. Dong, Wanmeng, Hui Liu, Xiaoxu Liu, Haoyu Wang, Xinru Li, and Lejie Tian. *International Journal of Hydrogen Energy* 2021, **46**, 9360-9370.
62. Bawari, Sumit, Nisheal M. Kaley, Shubhadeep Pal, Thazhe Veettil Vineesh, Shamasree Ghosh, Jagannath Mondal, and Tharangattu N. Narayanan. *Phys. Chem. Chem. Phys.* 2018, **22**, 15007-15014.
63. Digraskar, Renuka V., Vijay S. Sapner, Anil V. Ghule, and Bhaskar R. Sathe. *J. Electroanal. Chem.* 2021, **882**, 114983.
64. Chen, Yuxian, Jiayi Rong, Qiaolin Fan, Meng Sun, Qiuyi Deng, Zhonghua Ni, Xiao Li, and Tao Hu. *J. Mater. Chem. A* 2024.
65. Li, Jiaqi, Jiahao He, Tongtong Zhang, Ruobing Bi, Ying Hou, Fang Wang, and Zhuxia Zhang. *Int.l J. Hydrogen Energy* 2022, **47**, 31309-31320.

66. Maiti, Anurupa, and Suneel Kumar Srivastava. *ACS Appl. Mater. Interfaces.* 2020, **12**(**6),** 7057-7070.

67. Wang GZ, Zhang SF, Zhang XY, et al. Photonics Res 2015 A51–5.

68. Wu, Yanling, et al. *Proc. Natl. Acad. Sci.* 2015, **112**(38**),** 1800-11805.

69. Hu, Lili, et al. *Opt. Lett.* 2019, **44**(21, 5214-5217.

70. Zhang, Jingdi, et al. *Opt. Lett.* 2016, **41(8)**,1704-1707.

71. Wu YL, Zhu LL, Wu Q, et al. *Appl. Phys. Lett.* 2016, **108**(24),1110.

72. Wu R, Zhang YL, Yan SC, et al. Nano Lett. 2011, **11**(51),59–64.

73. Li, Jie, et al. *Nanophononics* 2020, **9**(8), 2415-2424.

74. Huang, Yixuan, et al. *Adv. Mater.* 2023, **35**(11), 2208362.

75. Wu, Leiming, et al. *Appl. Mater. Today* 2020, **19**, 100589.

76. Chen C, Kuang Y, Hu L. Joule. 2019, **3**(3),683-718.

77. Yang J, Pang Y, Huang W, Shaw SK, Schiffbauer J, Pillers MA, Mu X, Luo S, Zhang T, Huang Y, Li G. ACS Nano. 2017, **11**(6), 5510-8.

78. Awad FS, Kiriarachchi HD, AbouZeid KM, Ozgur U, El-Shall MS. ACS Appl. Energy Mater. 2018, **1**(3), 976-85.

79. Cui L, Zhang P, Xiao Y, Liang Y, Liang H, Cheng Z, Qu L. Adv. Mater. 2018, **30**(22), 1706805.

80. Fu Y, Wang G, Ming X, Liu X, Hou B, Mei T, Li J, Wang J, Wang X. Carbon 2018, **130**, 250-6.

81. Hao W, Chiou K, Qiao Y, Liu Y, Song C, Deng T, Huang J. Nanoscale 2018, **10**(14), 6306-12.

82. Kim K, Yu S, An C, Kim SW, Jang JH. ACS Appl. Mater. Interfaces. 2018, **10**(18), 15602-8.

83. Yang Y, Zhao R, Zhang T, Zhao K, Xiao P, Ma Y, Ajayan PM, Shi G, Chen Y. ACS Nano 2018, **12**(1), 829-35.

84. Zhang P, Liao Q, Zhang T, Cheng H, Huang Y, Yang C, Li C, Jiang L, Qu L. Nano Energy 2018, **46**, 415-22.

85. Li X, Xu W, Tang M, Zhou L, Zhu B, Zhu S, Zhu J. Proc. Natl. Acad. Sci. 2016, **113**(49), 13953-8.

86. Shi L, Wang Y, Zhang L, Wang P. J. Mater. Chem. A 2017, **5**(31), 16212-9.

87. Hu X, Xu W, Zhou L, Tan Y, Wang Y, Zhu S, Zhu J. Joule 2017, **29**(5), 1604031.

88. Li Y, Gao T, Yang Z, Chen C, Kuang Y, Song J, Jia C, Hitz EM, Yang B, Hu L. Nano Energy. 2017,**41**,201-9.

89. Chen C, Li Y, Song J, Yang Z, Kuang Y, Hitz E, Jia C, Gong A, Jiang F, Zhu JY, Yang B. Adv. Mater. 2017, **29**(30), 1701756.

90. Wang Y, Zhang L, Wang P. ACS Sustain Chem. Eng. 2016, **4**(3), 1223-30.

91. Wang X, He Y, Cheng G, Shi L, Liu X, Zhu J. Energy Convers. Manag. 2016, **130**, 176-83.

92. Li T, Liu H, Zhao X, Chen G, Dai J, Pastel G, Jia C, Chen C, Hitz E, Siddhartha D, Yang R. Adv. Func. Mater. 2018, **28**(16), 1707134.

93. Chandrashekara M, Yadav A. Solar Energy. 2017, **151**, 129-45.

94. Sajadi SM, Farokhnia N, Irajizad P, Hasnain M, Ghasemi H. J. Mater. Chem. A 2016, **4**(13), 4700-5.

95. Liu Y, Chen J, Guo D, Cao M, Jiang L. ACS Appl. Mater. Interfaces. 2015, **7**(24), 13645-52.

96. Zhu G, Xu J, Zhao W, Huang F. ACS Appl. Mater. Interfaces. 2016, **8**(46), 31716-21.

97. Wang J, Li Y, Deng L, Wei N, Weng Y, Dong S, Qi D, Qiu J, Chen X, Wu T. Adv. Mater. 2017, **29**(3), 1603730.

98. Chen R, Wu Z, Zhang T, Yu T, Ye M. RSC Adv. 2017, **7**(32), 19849-55.

99. Neumann O, Urban AS, Day J, Lal S, Nordlander P, Halas NJ. ACS Nano 2013, **7**(1), 42-9.

100. Hogan NJ, Urban AS, Ayala-Orozco C, Pimpinelli A, Nordlander P, Halas NJ. Nano Lett. 2014, **14**(8), 4640-5.

101. Fang Z, Zhen YR, Neumann O, Polman A, García de Abajo FJ, Nordlander P, Halas NJ. Nano Lett. 2013, **13**(4), 1736-42.

102. Zhou L, Tan Y, Wang J, Xu W, Yuan Y, Cai W, Zhu S, Zhu J. Nat. Photonics 2016, **10**(6), 393-8.

103. Zhu M, Li Y, Chen F, Zhu X, Dai J, Li Y, Yang Z, Yan X, Song J, Wang Y, Hitz E. Adv. Energy Mater. 2018, **8**(4),1701028.

104. Sun W, Zhong G, Kübel C, Ali FM, Qian C, Wang L, Ebrahimi M, Reyes LM, Helmy AS, Ozin GA. Angew. Chem. Int. Ed. 2017, **56**(22), 6329-34.

105. Chen M, He Y, Huang J, Zhu J. Energy Convers. Manag. 2016, **127**, 293-300.

106. Q. Wang, Q. Guo, F. Jia, Y. Li, S. Song, *ACS Appl. Mater. Interfaces* 2020, **12(29),** 32673-32680.

107. Y. Wang, J. Nie, Z. He, Y. Zhi, X. Ma, P. Zhong, *ACS Appl. Mater. Interfaces* 2022, ***14*****(4),** 5876-5886.

108. L. Wang, J. Shang, G. Yang, Y. Ma, L. Kou, D. Liu, W. Lei, *Small* 2022, ***18*****(28),** 2201770.

109. W. Li, X. Tian, X. Li, S. Han, C. Li, X. Z. Zhai, Y. Kang, Z. Z. Yu, *J. Mater. Chem. A* 2021, ***9*****(26),** 14859-14867.

110. H. Fan, A. Gao, G. Zhang, S. Zhao, J. Cui, Y. Yan, *Chem. Eng. J.* 2021, **415**, 128798.

111. L. Ying, H. Zhu, H. Huang, X. Qu, C. Wang, X. Wang, F. Duan, S. Lu, M. Du, *ACS Appl. Energy Mater.* 2021, ***4*****(4),** 3563-3572.

112. D. Ghim, Q. Jiang, S. Cao, S. Singamaneni, Y. S. Jun, *Nano Energy* 2018, **53**, 949-957.

113. L. Zhang, B. Tang, J. Wu, R. Li, P. Wang, Adv. Mater. 2015**, 27**, 4889-4894.

114. W. Xu, X. Hu, S. Zhuang, Y. Wang, X. Li, L. Zhou, J. Zhu, *Adv. Energy Mater.* 2018, ***8*****(14),** 1702884.

115. C. Liu, P. Wu, RSC *Adv.* 2024, **14(15),** 10370-10377.

116. T. Gao, Y. Li, C. Chen, Z. Yang, Y. Kuang, C. Jia, L. Hu, *Small Methods*, 2019, **3(2),** 1800176.

117. B. Zhang, Q. Gu, C. Wang, Q. Gao, J. Guo, P. W. Wong, A. K. An, ACS *Appl Mater. Interfaces*, 2021, **13(3),** 3762-3770.

Chapter 3 Experimental Details

This chapter provides an in-depth discussion of the experimental methods utilized for fabricating various nanostructures, including nanorods, nanosheets, and heterointerfaces. It also covers the diverse characterization techniques employed to analyse these nanostructures.

3.1 Preamble:

This chapter explores various synthesis methods for nanostructures, particularly focusing on nanorods and nanosheets. It delves into the utilization of diverse characterization techniques to verify the nanoscale dimension, phase purity, lattice structure, morphology as well as electrical and optical properties of the samples. Additionally, it addresses the methodologies and instruments employed for electrocatalysis, spectroscopy and desalination characterization.

3.2 The landscape of synthesis route for nanomaterials:

There are two fundamental synthesis approaches for nanomaterials: one is the top-down approach, and the other is the bottom-up approach. The ultimate goal of these two approaches is to synthesize nanomaterials. However, there is a stark contrast between the top-down and bottom-up approaches.

3.2.1 Top-down approach

This approach initiates with large-scale or bulk materials and culminates in the creation of nano-sized structures. Various methods such as mechanical milling, lithography and laser ablation are employed within the framework of the top-down approach.

3.2.2 Bottom-up approach

The bottom-up approach commences with the aggregation of atoms or molecules, gradually forming clusters through nucleation, ultimately leading to the synthesis of nanomaterials. Various techniques, including chemical vapor deposition, solvothermal and hydrothermal methods, as well as the sol-gel method, adhere to the bottom-up approach.

Both the top-down and bottom-up approaches play crucial roles in nanomaterial synthesis. However, a notable challenge with the top-down method lies in its tendency to introduce imperfections in surface structure, leading to the presence of unwanted impurities and structural defects in the synthesized materials. Conversely, the bottom-up approach offers the advantage of achieving desired sizes, shapes and

orientations of nanomaterials during synthesis. This method is characterized by its efficiency, cost-effectiveness and widespread acceptance in the field of nanomaterial synthesis.

The optical and electrical properties of nanomaterials are significantly influenced by factors such as uniformity in size, shape and growth orientation. In the upcoming section, we will explore several advantageous synthesis procedures employed to fabricate nanorods and 2D nanosheets, crucial for achieving desired material properties.

3.2.3 Solvothermal and Hydrothermal methods:

Hydrothermal or solvothermal synthesis emerges as a straightforward and highly efficient approach for crafting various nanostructured materials. This method, also known as closed-vessel reaction, involves sealing the precursor within an aqueous medium inside an autoclave vessel, typically encased in a steel jacket to prevent any chemical reactions. To further mitigate potential interactions with the steel, an inner Teflon container is employed. The system is then subjected to high pressure and high temperature conditions for a specific duration. Solvothermal variants substitute water with different solvents. The versatility of hydrothermal or solvothermal techniques facilitates the easy attainment of diverse nanostructures. Researchers are drawn to its high product purity, gentle preparation conditions and the simplicity of equipment required.

3.3 Synthesis technique and instruments of 2D materials specially (reduced graphene oxide)

Graphene, composed of a single layer of carbon atoms in a hexagonal honeycomb pattern through sp^2 hybridization, has fascinated researchers since its inception due to its exceptional thermal, optical and electrical attributes. Graphene can be produced through various techniques, including chemical vapor deposition, mechanical exfoliation and annealing of single crystal SiC under ultrahigh vacuum conditions. However, these methods are not suitable for widespread research due to

their high costs and low yields. Among these methods, chemical approaches are preferred, although they often result in the formation of reduced graphene oxide (rGO), which is a mixture of sp^3 and sp^2 hybridized carbon atoms contained a significant amount of several functional groups.

The chemical synthesis of reduced graphene oxide comprises three distinct steps. In the subsequent section, we will provide a concise overview of each step along with the necessary instrumentation employed in the process.

1st step (oxidation of graphite)

Graphite oxide is prepared by modified Hummer's method. Typically, 2 gm graphite powder was mixed with 30 gm NaCl and grinded well. NaCl particles are brittle and harder than graphite which act as milling agents, chopping graphite particles. Then the fine powder was dispersed in 200 ml of distilled water under continuous stirring for 30 minutes. After that, the dispersion was filtered and washed with distilled water thoroughly to remove the residual NaCl. In the second step, the collected graphite powder was mixed into 46 ml concentrated H_2SO_4 in a glass beaker and stirred continuously for at least 72 hours. Here, H_2SO_4 was used as an intercalating agent. In third step, glass beaker was placed on an ice bath. Then 6 gm of KMnO4 was added slowly into the solution under continuous stirring (400 rpm) for 4 hours. The beaker was then transferred on the hot plate at temperature 60 °C. After 1 hour, the beaker was kept on another magnetic stirrer and 20 ml of distilled water was added into it, under continuous stirring for 15 minutes. Then 8 ml H_2O_2 (30%) was added to reduce residual $KMnO_4$ to soluble manganese sulfate ($MnSO_4$) in an acidic medium.

$$2KMnO_4 + 5H_2O_2 + 3H_2SO_4 \rightleftharpoons 2MnSO_4 + K_2SO_4 + 8H_2O + 5O_2.$$

The obtained solution was centrifuged at 6000 rpm at least 4 times with a mixture of 46 ml concentrated HCl and 456 ml of distilled water for removing the metal sulfate ions. After that, the solution was neutralized by multiple centrifugation process (8000 rpm) with distilled water.

3.3.1 Centrifugation technique

In a dispersion of liquid, solid particles precipitate at the bottom of the container under the action of gravitational force. In that way, solid particles are separated from the liquid. However, this process is extremely slow and depends on density of the particles. Particles of different sizes have different mass exhibits different density go through different gravitational force. That's why massive particles precipitates so quickly. But for lighter particles precipitation rate is too low. Centrifugation is a technique that accelerates the sedimentation rate of solid particles in a liquid, overcoming the slower precipitation rate. Centrifugal force acts on the liquid containing solid particles, causing them to separate from the liquid and accumulate towards the bottom or wall of the container, based on their shape, size, density, viscosity of the liquid medium and rotor speed. Figure 3.1 represents the digital image of (a) centrifuge machine (b) centrifuge rotor with centrifuge tube holder.

3.3.2 What is supernatant?

In centrifugation technique, the liquid lying above the precipitate is called the supernatant. It plays a crucial role in the synthesis of few-layer 2D nanomaterials.

3.3.3 Role of centrifugation in 2D nanomaterial synthesis

Centrifugation is utilized rigorously for washing purposes, effectively adjusting the pH of a solution from acidic or alkaline to a neutral state. After achieving neutral pH the 2D nanomaterials are subjected to exfoliation through ultrasonication. The resultant stock solution is assorted of different size and thickness of 2D nanosheets. Typically, the stock solution is centrifuged at a rate of 8000-12000 rpm, and the resulting supernatant contains exfoliated 2D nanomaterials. Centrifugation plays a crucial role in liquid exfoliation of 2D nanosheets, as the centrifugation force prevailed the van der Waals force.

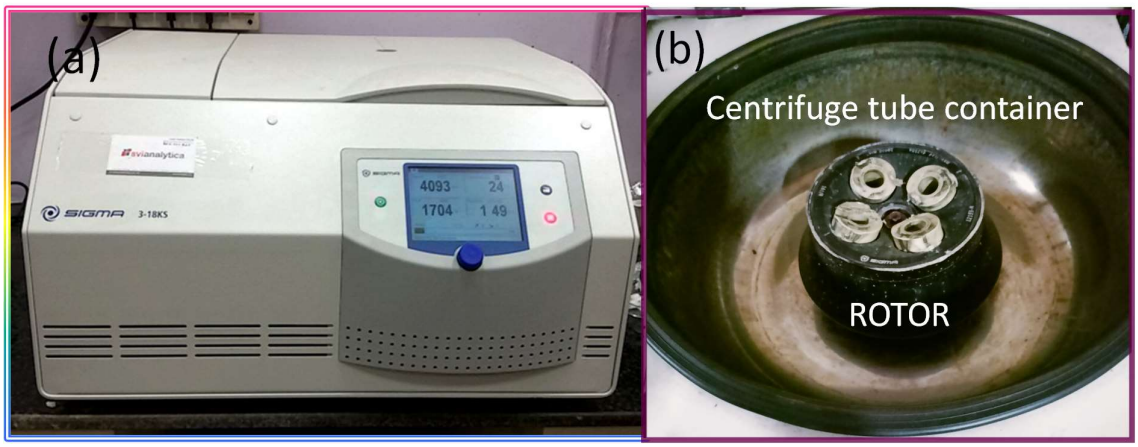

Figure 3.1: *Digital image of (a) centrifuge machine (b) Inside view of chamber with rotor and centrifuge tube holder*

3.4 X -Ray Diffractometer

X-ray diffraction is a non-destructive technique used to study the crystalline nature of materials. It works by having X-rays coherently diffract off different atomic planes of a material in specific directions, which are determined by the orientation of these atomic planes. This scattering factor depends on both the electronic density of atoms and the geometrical atomic arrangement in the unit cell of that material. There is a relation between diffraction intensity and total scattering factor

$$I = |F|^2$$

Where, I is the diffraction intensity, F is the total scattering factor.

Hence, the diffraction intensity and angle of diffraction provide a three-dimensional understanding of the electron cloud density and the atomic arrangement of the crystals being studied.

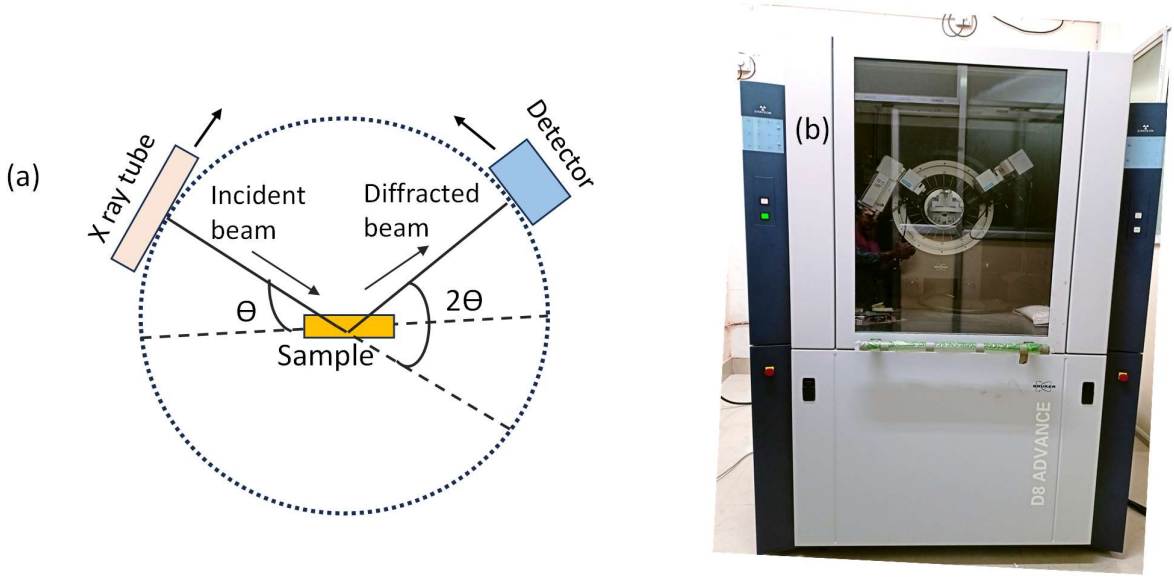

Figure 3.2: *(a) Schematic diagram of X-ray diffractometer in θ-2θ mode, (b) Digital image of X-ray diffractometer*

An X-ray diffractometer consists of three main components: an X-ray tube, a sample holder and a detector. In figure 3.2(a) and 3.2(b) represents schematic diagram and digital image of X-ray diffractometer respectively. In this setup, X-rays (specifically Cu K_α, λ = 1.54 Å) are generated by the X-ray tube. These X-rays are directed onto the sample holder, where they undergo elastic scattering from the atomic planes of the sample. The scattered waves emerge as outgoing spherical waves. Constructive interference of these waves occurs only when following Bragg's law is satisfied for a specific set of planes.

$$2d \sin\theta = n\lambda$$

where, d is the interplanar spacing, θ is the diffraction angle and n is an integer. In practice, scanning the sample across a range of 2θ angles, all potential diffraction directions of the lattice are captured due to scattering by the various planes within the material. Each crystal has a unique set of d-spacings, so converting the diffraction peaks to d-spacings using Bragg's law enables the identification of the elements or compounds present. Typically, this identification is done by comparing the calculated d-spacings with standard reference patterns from the JCPDS database.

There are two basic configuration of powder Xray diffractometers:

- θ-θ configuration: In this configuration source of X-ray and detector move simultaneously
- θ-2θ configuration: Here, sample moves at half the speed of the detector

In data curation time, the detector, integrated with electronics and specialized software, electronically processes and records the angles and intensities of the diffracted beams.

3.5 Electron Microscope

An electron microscope is a type of microscope that uses a highly energetic beam of electrons as the illumination source, instead of visible light as in a conventional microscope.[1] An electron microscope examines the surface topography of materials and measures the shape and size of particles ranging from the sub-micrometre to nanometre scale that compose the material. An electron microscope also reveals the elemental composition and their relative quantities. Due to electrons having wavelengths 100,000 times smaller than visible light, electron microscopes have 100,000 times greater magnification power than optical microscopes. The first electron microscope, the transmission electron microscope, was developed in 1931 and is used to 'see through' specimens. The others are scanning electron microscope (SEM),[2] transmission electron microscope (TEM) [3,4] etc.

The basic working principle of an electron microscope is that, in a vacuum chamber, a highly energetic beam of electrons is generated by an electron gun and accelerated towards a positive electrode potential. The electron beam is focused onto the sample by a magnetic lens. After interacting with the sample, the electron beam is recorded by a detector and then converted into an image.

3.5.1 Scanning Electron Microscope (SEM)

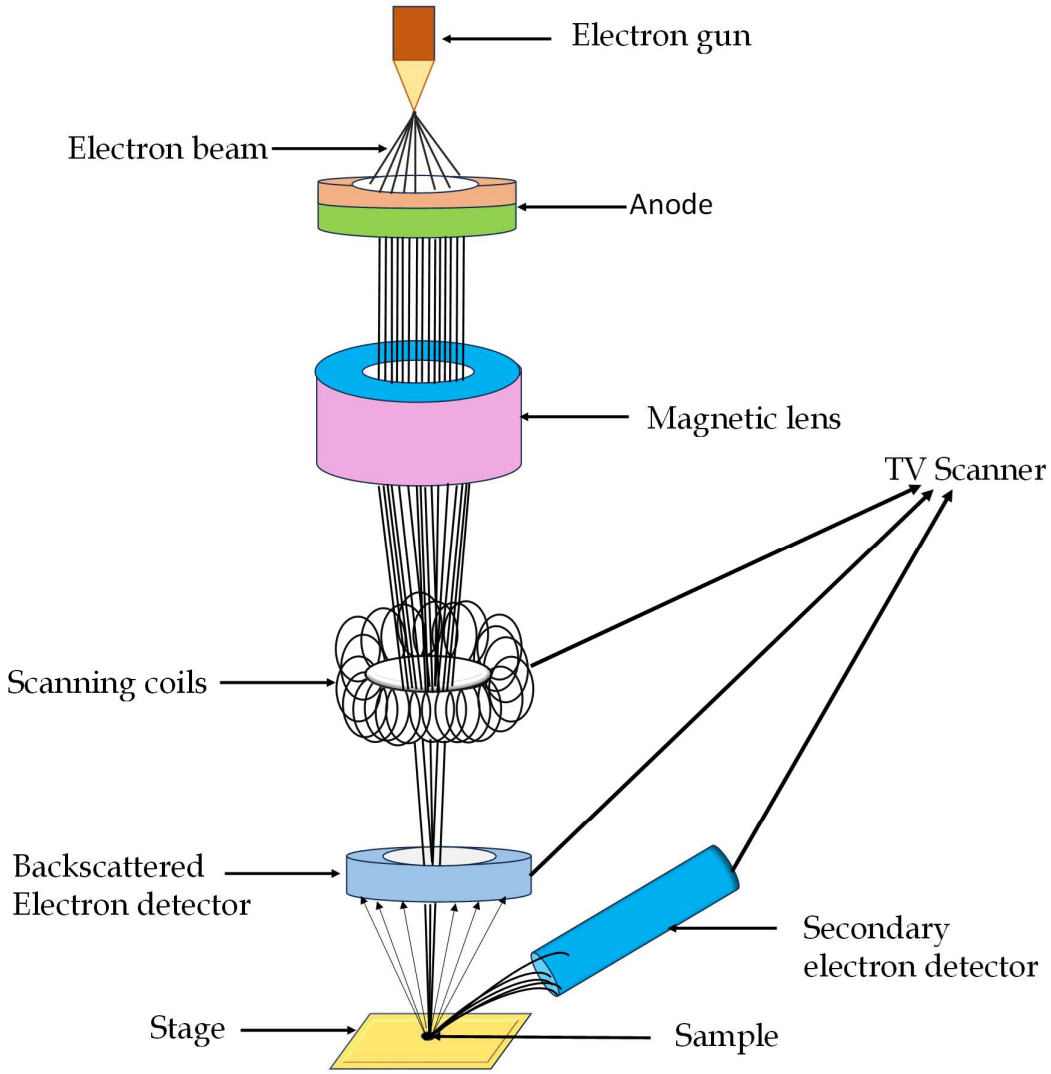

Figure 3.3: *Schematic diagram of Scanning electron microscope*

Schematic diagram and digital image of Scanning electron microscope is displayed in the above figure 3.3. and figure 3.4 respectively. In (SEM), an electron beam is produced thermionically from a tungsten filament cathode within the electron gun. This beam is focused into a fine probe and rastered over the specimen's surface. lanthanum hexaboride (LaB_6) single crystal, field emission gun (FEG), Schottky emission electron gun are used as electron emitters. The SEM operates at a working voltage ranging from 2 to 50 keV. The diameter of the electron beam can vary from 5

nanometres to several micro meters, depending on the type of electron gun, the accelerating voltage of the electrons and the types of lenses used.

Figure 3.4 *Digital image of Scanning electron microscope*

Scanning coils placed above the objective lens direct the electron beam onto the sample and scan the surface of the sample in the X-Y plane. The scanning coils are connected to an external computer, which, with the help of specialized software, records the position of the electron beam on the sample surface in the X-Y plane. When the electron beam interacts with the sample, it penetrates a few microns into the material, generating various types of signals such as Auger electrons, secondary electrons, backscattered electrons, characteristic X-rays and continuum X-rays.

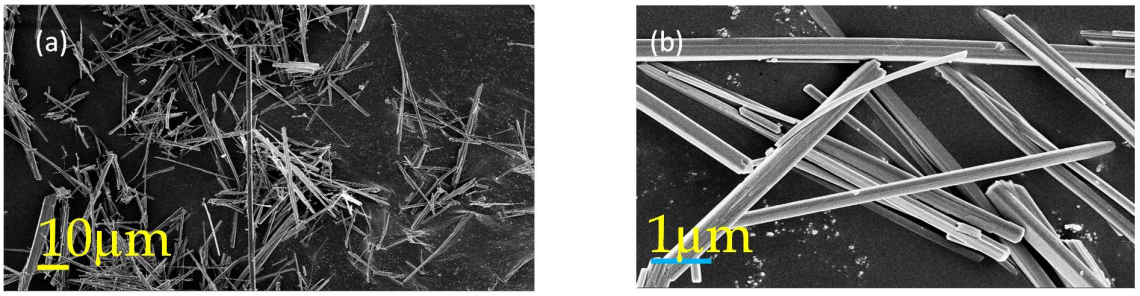

Figure 3.5 *(a) low magnification and (b) high magnification field emission scanning electron microscope image of Sb_2Se_3 nanorods*

The image of SEM displayed in figure 3.5 (a)-(b) result from the emission of secondary electrons caused by the inelastic scattering of incident electrons. Since the probing electron beam is very narrow, SEM micrographs have a large depth of field, providing a distinctive three-dimensional appearance that is useful for examining the surface structure of a sample. Energy dispersive analysis of X-ray (EDAX)is done by collecting Characteristic X-rays which are generated when an ionized atom returns to its ground state by filling an inner shell electron vacancy with an electron from a higher orbital. The energy difference between the two electron shells corresponds to the characteristic X-ray energy, which can be used to identify the specific element from which it originated. EDAX determines the elemental composition of materials, it also generates continuum background along with characteristic X-ray.

The resolution of SEM depends on different factors such as electron beam spot size, the volume of the sample with which the electron beam interacts.

3.5.2 Transmission Electron Microscope (TEM)

Figure 3.6 *Digital image of transmission electron microscope (TEM)*

Transmission electron microscopy is an analytical technique that provides both morphological and crystallographic information (lattice spacing) simultaneously. It also reveals the orientation of atomic planes, atomic arrangement and coordination chemistry of atoms in the specimen. Digital image and schematic diagram of transmission electron microscope is represented in figure 3.6 and figure 3.7 respectively.

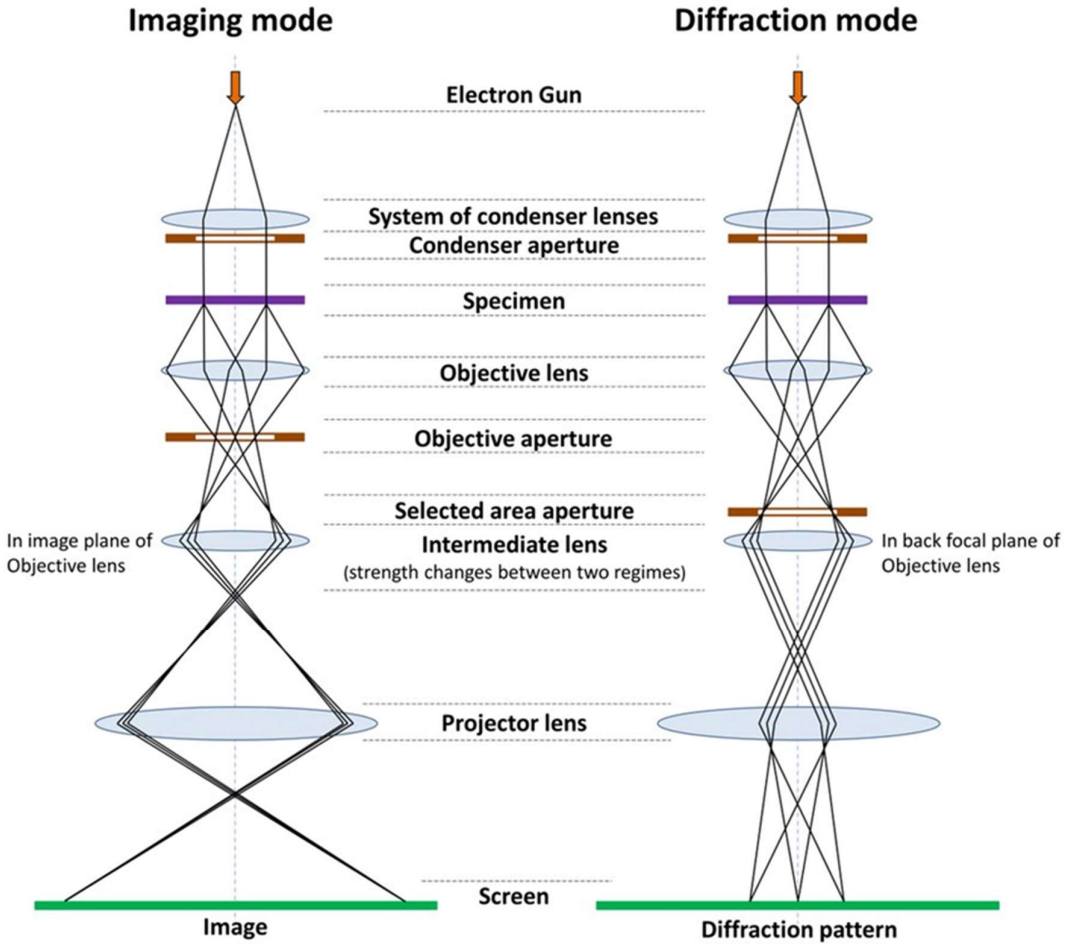

Figure 3.7 *Schematic diagram of TEM*

To produce an image, the electron beam is accelerated with a high voltage (80-300 kV) to pass through ultrathin samples, making them transparent to the electrons.

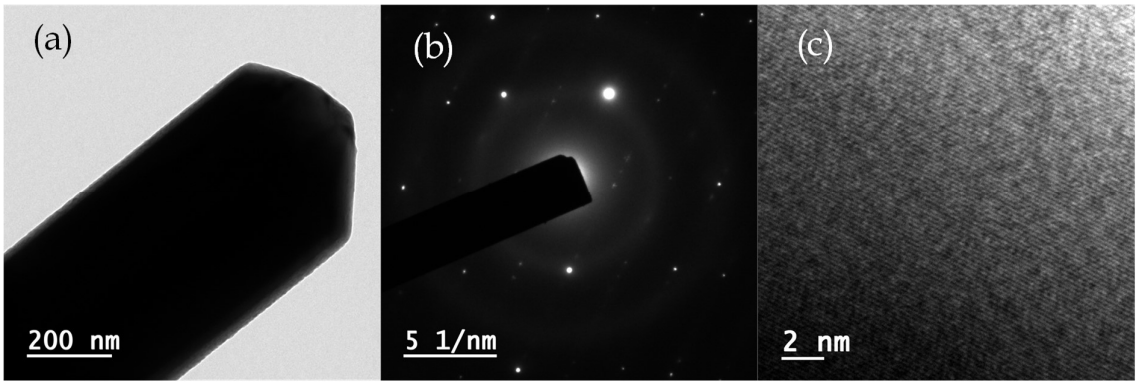

Figure 3.8 *(a)TEM image of Sb_2Se_3 nanorods (b) selected area electron diffraction pattern (SAED) of Sb_2Se_3 nanorods (c) High resolution transmission electron microscopy (HRTEM) of Sb_2Se_3 nanorods*

The number of un-scattered electrons that pass through a sample is inversely related to the sample's thickness. Thicker areas of the sample will transmit fewer un-scattered electrons and therefore appear darker, while thinner areas will transmit more electrons and appear lighter. This variation in electron transmission creates a contrast between dark and light areas in the sample. This method of TEM operation is known as bright field imaging, as illustrated in figure 3.8 with the resulting micrograph shown in figure 3.8 (a). Additionally, when an electron beam is directed at a crystalline material and Bragg's condition is met, the resulting scattered electrons are collected by magnetic lenses, forming a pattern of spots specific to the material. This pattern represented in figure 3.8(b) corresponds to the lattice spacing d. In high-resolution TEM (HRTEM) mode, displayed in figure 3.8(c) a resolution of up to 0.2 nm can be achieved, making it highly effective for observing the lattice fringes of the specimen being examined. Energy-filtered transmission electron microscopy (EFTEM) is a technique that utilizes electrons of specific energies to create images or diffraction patterns. This method offers insights into the elemental composition of the material being examined.

3.6 X-ray Photoelectron Spectroscopy (XPS)

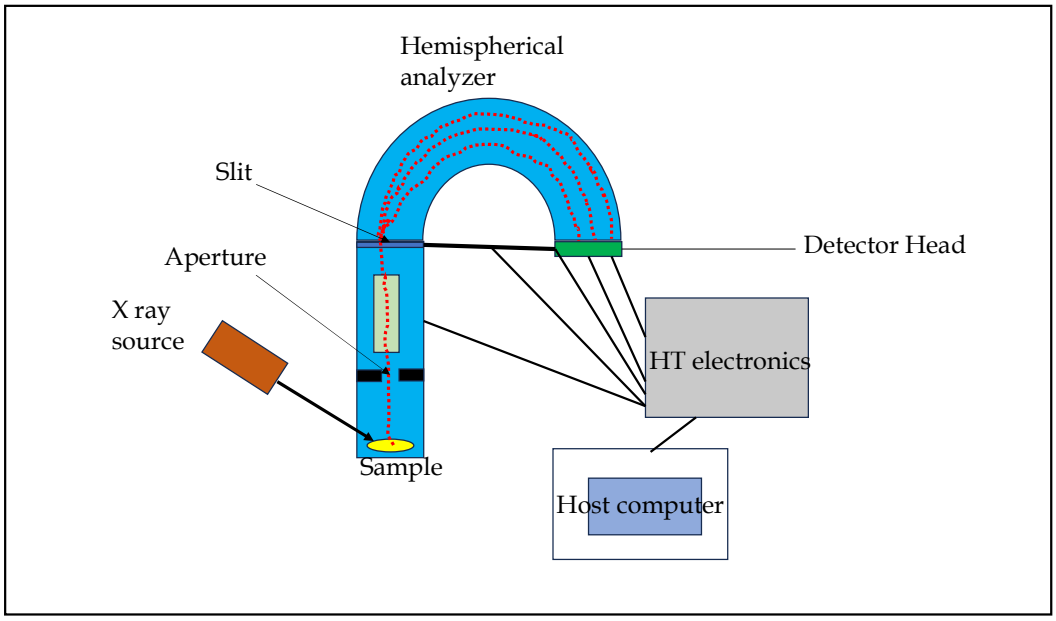

Figure 3.9 *Schematic diagram of an XPS spectrometer*

X-ray photoelectron spectroscopy (XPS) is a highly powerful and sensitive technique used to determine the surface composition of a material, typically within a depth of about 10 nm. It can identify the elemental composition, chemical states of elements and the bond lengths between them. Additionally, XPS provides information on electronic configurations, electron density and the atomic percentages of the elements present. Figure 3.9 and figure 3.10 represents the schematic diagram and digital image of X ray photoelectron spectrometer respectively.

Figure 3.10 *Digital image of X-ray photoelectron spectrometer*

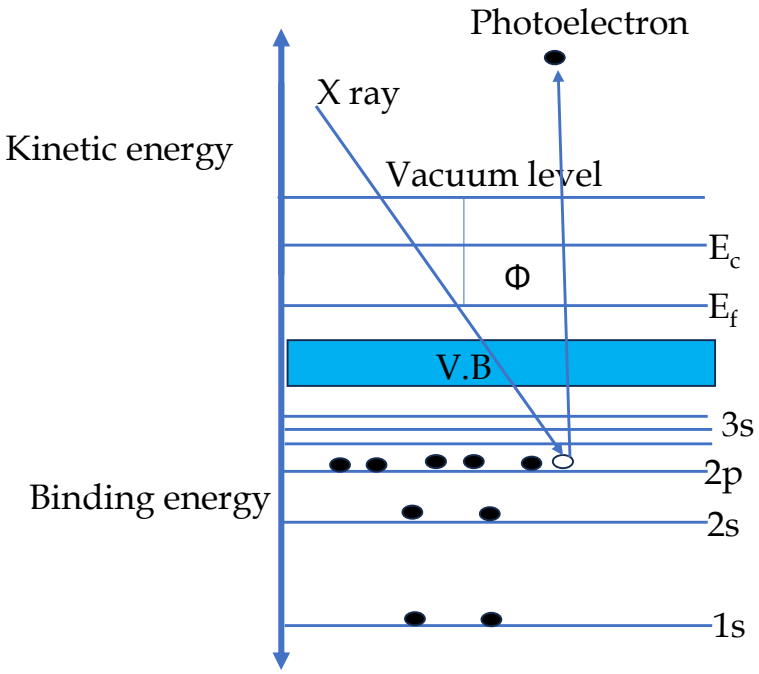

Figure 3.11 *Band diagram of a semiconductor under XPS measurement condition*

Typically, X-rays (such as Al Kα X-rays) with an energy of 1486.7 eV irradiate the material's surface. The instrument measures the kinetic energy of the resulting photoelectrons emitted from the material. Since the kinetic energy is known, the binding energy of each electron can be determined using the following photoelectric equation.

$$E_{bind} = E_{photon} - E_{k.E} - \Phi$$

Where E_{bind} is the binding energy of the emitted electrons, E_{photon} is the incident energy of X ray, $E_{k.E}$ kinetic energy of the emitted electron and Φ is the work function for the specific surface of the material. Figure 3.11 represents the band diagram of a semiconductor under XPS measurement condition. The XPS plot shows the binding energy of emitted electrons along the X-axis versus the number of emitted electrons counts on the Y-axis. XPS peaks correspond to different characteristic peaks such as 1s, 2s, 2p, 3s, etc., for specific materials. The population of electrons corresponding to each peak is directly proportional to the amount of the element present in the material. In this way, atomic percentages are easily determined from XPS data. XPS is typically conducted under ultrahigh vacuum conditions to ensure the accuracy of the data.

3.7 Optical Characterization Techniques

3.7.1 UV-Vis Absorption Spectroscopy

UV-Vis spectrometer is an analytical tool that measures the absorbance and transmittance of a sample under the irradiation of UV-Vis light. Atoms in the material absorb energy when they undergo electronic transitions from the ground state to the excited state through the interaction with UV-Vis light. A UV-Vis spectrometer measures the absorbance of a sample dispersed in a solvent and placed in a cuvette, comparing it to a reference sample or a blank cuvette. The digital photograph of UV-Vis instrument represented in the following figure 3.12

Figure 3.12 *Digital photograph of UV-Vis spectrometer*

The Beer-Lambert law states that absorbance (A) is proportional to the path length of the light (l), the concentration of the absorbing material (c) and the molar absorptivity (ε).

$$A = \varepsilon cl = -log_{10}\left(\frac{I}{I_0}\right)$$

Where I_0 is the incident light intensity and I is the transmitted light intenity.

This procedure can also determines absorption coefficient (α)

$$\alpha\ (cm^{-1}) = \frac{\ln(10)\times A}{l\ (cm)}$$

Optical bandgap of a material can be determined from the plot of $(\alpha h\nu)^{1/2}$ Vs. hν ,which is called Tauc plot. From Diffuse Reflectance Spectra (DRS) measurement optical band gap of a material can alsso be deduce from the plot of $[F(R)\ h\nu]^{1/2}$ Vs. hν

Where F(R) is Kubelka-Munk function

$$F(R) = \frac{(1-R)^2}{2R} = \frac{\alpha}{s}$$

Where R is the measured reflectance of a sample, (α) is the absorption coefficient,S is the scattering coefficient. Tauc plot is suitable for narrow absorption edge , Kubelka-Munk plot is suitable for broader absorption edge.

Figure 3.13 *Digital photograph of AutoLab Metrohm 204 electrochemical workstation*

3.8 Electrochemical Characterization Techniques

The electrocatalytic properties of the samples were analysed using a software-controlled three-electrode system (AutoLab Metrohm 204) in a 0.5 M H_2SO_4 aqueous solution. Figure 3.13 represents the digital photograph of AutoLab Metrohm 204. Techniques such as linear sweep voltammetry (LSV), i-t amperometry, electrochemical impedance spectroscopy (EIS), measurements were employed. Additionally, the electrochemical double layer capacitance of the samples was evaluated using cyclic voltammetry (CV) and EIS tests. These measurements were conducted at room temperature in a conventional three-electrode electrochemical cell (potentiostat AutoLab Metrohm-204), comprising the prepared samples as the working electrode, a saturated Ag/AgCl reference electrode, a graphite rod as counter electrode and 0.5 M H_2SO_4 solution as the electrolyte.

References:

1. Electron Microscopy: Methods and Protocols, Editor: John; Springer Nature Link (2007)
2. Field Emission Scanning Electron Microscopy; New Perspectives for Materials Characterization, Nicolas Brodusch , Hendrix Demers , Raynald Gauvin, Springer Nature Link (2018)
3. Transmission Electron Microscopy, Ludwig Reimer and Helmut Kohl, Springer (2008)
4. Transmission Electron Microscopy; A Textbook for Materials Science, David B. Williams, Second Edition, Springer (2009)

Chapter 4

Tailoring the Sb_2Se_3/rGO heterointerfaces for modulation of electrocatalytic hydrogen evolution performances in acidic media

The chapter discusses the development of Sb_2Se_3/rGO heterointerfaces for hydrogen evolution electrocatalysis as part of the global shift towards clean hydrogen energy. Using a solvothermal approach, these heterostructures demonstrate improved electrocatalytic performance, with a reduced onset potential of -0.32 V and a two-fold decrease in the Tafel slope compared to Sb_2Se_3 alone. The enhanced performance is attributed to improved interfacial electron transport enabled by heterointerface engineering. Density functional theory (DFT) calculations reveal that the interaction between Sb_2Se_3 and rGO lowers the hydrogen adsorption energy at active Se sites, facilitating better hydrogen ion adsorption and charge transfer from acidic media, ultimately boosting the hydrogen evolution reaction (HER) efficiency.

This chapter has been published in ACS Applied Energy Materials.

Sen et al. ***ACS Applied Energy Materials*** **2022 ,6, 58-67.**

4.1. Introduction

Clean energy generation in environmentally compatible and cost-effective route is technologically important and reliable strategy to shift the global energy concern toward renewable energy resources.[1-4] Molecular hydrogen (H_2), having high gravimetric energy density has tremendous potential for utilization as a green fuel for the future energy infrastructure, owing to its capacity to be stored and release on demand via feeding into fuel cells without any environmental impact.[5] Additionally, H_2 has been largely employed as a crucial chemical feedstock in polymer production, ammonia and methanol generation.[1,6–7] Globally, H_2 has been mostly produced via natural gas steam reforming process which releases anthropogenic CO_2 to the environment.[6,8] Water electrolysis is one of the important environmentally sustainable process to shape future energy infrastructure based on H_2 fuel.[6,9–11] However, to deploy water electrolysis as the leading part in hydrogen economy, earth-abundant, highly efficient and stable hydrogen evolution (HER) electrocatalysts are compulsory.[12–14] Although, noble metal Pt is highly efficient HER electrocatalyst but scarcity of Pt and high costs limit its integrability in hydrogen economy.[14]Therefore, enormous research has been employed to develop highly efficient, stable noble metal free HER catalysts. [10,12–14]

Recently, chalcogenides materials, e.g.; MoS_2, $MoSe_2$, WS_2, WSe_2 , NiSe, $ReSe_2$, $RhSe_2$ etc. are drawing attention as promising HER catalysts owing to cost effectiveness and superior electrocatalytic properties.[13,15–18] Notably, antimony selenide Sb_2Se_3 a $V_2{-}VI_3$ binary chalcogenide material have been appealing owing to

their potential applications in diverse area e.g.; photoelectrochemical hydrogen evolution,[9] electrochemical energy storage devices,[19] thermoelectric[20] and photovoltaics[21] etc. owing to superior photocatalytic properties, Na, Li storage, good thermal conductivity, low-band-gap (1.2−1.0 eV) and many other advantageous properties. Predominantly, Sb_2Se_3 is formed by staking $[Sb_4Se_6]_n$ nanoribbons via. van der Waals interaction along the (100) and (010) axes and strong covalent bond along (001) axis.[22] The inherent tendency to grow along Z axis make Sb_2Se_3 as 1D structure which not only offers enormous reaction platform but also offers facile electron/ion transport.[22] Nevertheless, Sb_2Se_3 is not explored for electrocatalytic hydrogen evolution to the best of our knowledge, although constituents are earth abundant, highly stable in harsh acidic or alkaline medium and less toxic.

Heterostructure design is one of the most promising approaches to tune the catalytic activity of the chalcogenides materials by modulating the electron transport properties and enhancing the mass transport properties.[23] Especially, rGO nanosheets are crucial for its superior electronic conductivity as well as superior chemical coupling owing to rich surface functionality which are tremendously effective for a large variety of extremely active heterostructure HER catalysts design.[16,24–26] For example, $MoSe_2$ nanosheets grown on rGO nanosheets, anchoring FeP nanoparticles on graphene sheets,[27] MoS_2 on rGO nanosheets,[26] 2D WS_2 sheets on rGO,[16] $W_xMo_{1-x}S_2$ and Graphene based heterostructures,[24] etc. were extensively investigated for their superior catalytic properties. Notably, Li et al. demonstrated MoS_2 nanoparticles on rGO nanosheets which acts as a conductive

support.[28] Strong chemical and electronic coupling between rGO and MoS_2 lead to substantially increased active edge sites and faster electron transport which necessarily accelerates the catalytic activity of MoS_2.[28] Similarly, in-situ growth of MoS_2 nanoparticles on mesoporous graphene foams creates interconnected conductive skeleton, forming MoS_2/mesoporous graphene foams heterostructure which endorses a high cathodic current density of 100 mA cm^{-2} with substantially less overpotential.[29] Moreover, anchoring heterostructures on conductive substrates could boost the exposure of active sites, facilitating mass transfer.[29] Cai et al. constructed heterointerface of Ni_2P nanosheets and graphene sheets on top of Nickel foam, forming 3D assembly which showed 10 mA cm^{-2} current density at low overpotential.[30] Moreover Ding et al. proposed that the 3D NiFe layered doubled hydroxide/graphite Felt (LDH/GF) electrocatalyst draw attention due to their low overpotential 214 mV at 50 mA cm^{-2} current density.[31] This superior catalytic activity is accomplished owing to largely enhanced active sites and easy mass transfer. Interestingly, constructing heterostructures often enhances the stability of the catalysts which therefore promotes the viability in large-scale hydrogen economy.

In this regard, we have investigated the electrocatalytic properties of Sb_2Se_3 nanorods, grown via simple solvothermal method. Additionally, observed poor catalytic activity of Sb_2Se_3 is modulated by synthesising conductive rGO nanosheets supported Sb_2Se_3 hybrid which produces Sb_2Se_3/rGO heterointerfaces, locally via solvothermal growth approach. Importantly, we employed density functional theory (DFT) to estimate the catalytic active sites for hydrogen evolution reaction and the

corresponding Gibbs free energy of hydrogen adsorption. Our investigation suggests that owing to coupling with rGO, the Gibbs free energy of hydrogen adsorption at the active sites of Sb_2Se_3 reduces significantly. Moreover, Bader charge analysis was performed which also suggests superior HER activity of the Sb_2Se_3 after making heterostructure with rGO.

4.2. Experimental Sections

4.2.1 Materials

All chemicals, including $SbCl_3$, DEG, ammonia, sodium sulfite, selenium powder, graphite powder, NaCl, H_2SO_4 and $KMnO_4$, were of analytical grade (Merck) and used without any further purification.

4.2.2 Synthesis of Sb_2Se_3 nanorods

A typical solvothermal procedure was adopted for preparing Sb_2Se_3.[32] Here antimony source, $SbCl_3$ (0.086 gm) was dissolved in 75.8 ml DEG and then ammonia was added under magnetic stirring. Subsequently, 0.095 gm sodium sulphite and 0.048 gm Se powder were added into the solution. After 15 min stirring, the as prepared mixture was transferred into a 100 ml teflon-lined stainless-steel autoclave followed by heating in a conventional oven at 180 ℃ for 22 hours. After that, the autoclave was cooled down to room temperature naturally. Finally, the products were filtered by vacuum filtration and washed with deionized water followed by absolute ethanol. After vacuum filtration and washing step, the product was collected and dried in vacuum oven at 80 ℃ overnight for further use.

4.2.3 Synthesis of GO

GO was synthesized from graphite powder in a three steps approach.[33] In first step, 2 g graphite powder was mixed with 30 g NaCl and grinded well. NaCl particles are brittle and harder than graphite, acting as milling agents which chop graphite particles. Then the fine powder was dispersed in 200 mL of distilled water under continuous stirring for 30 minutes. After that, the dispersion was filtered and washed with distilled water thoroughly to remove the residual NaCl. In the second step, the collected graphite powder was mixed into 46 mL concentrated H_2SO_4 in a glass beaker and stirred continuously for at least 72 hours. Here, H_2SO_4 was used as an intercalating agent. In third step, glass beaker was placed on an ice bath. Then 6 g of $KMnO_4$ was added slowly into the solution under continuous stirring (400 rpm) for 4 hours. The beaker was then transferred on a hot plate at temperature 60 °C. After 1 hour, the beaker was kept on another magnetic stirrer and 20 mL of distilled water was added into it, under continuous stirring for 15 minutes. Then 8 mL of H_2O_2 (30 %) was added to reduce residual $KMnO_4$ to soluble manganese sulfate ($MnSO_4$) in an acidic medium.

$$2KMnO_4 + 5H_2O_2 + 3H_2SO_4 \rightleftharpoons 2MnSO_4 + K_2SO_4 + 8H_2O + 5O_2 \quad (1)$$

The obtained solution was centrifuged at 6000 rpm at least 4 times with a mixture of 46 mL concentrated HCl and 456 mL of distilled water for removing the metal sulfate ions. After that, the solution was neutralized by multiple centrifugation process (8000 rpm) with distilled water. To obtain graphene oxide, exfoliation of the as obtained graphite oxide was performed by prob sonication for at least 2 hours.

Finally, graphene oxide was collected by drying the supernatant solution as obtained via centrifugation process.

4.2.4 Synthesis of Sb_2Se_3/rGO

We successfully synthesized Sb_2Se_3/rGO via solvothermal method (figure 4.1). First, as prepared GO was mixed in DMF for 5 hours by probe sonication to obtain a homogeneous GO dispersion. Subsequently, GO dispersion was mixed in the Sb_2Se_3 precursor and was transferred into Teflon lined autoclave. Temperature of the autoclave was maintained at 180 °C for 22 hours. After cooling down to room temperature, the as prepared products were filtered by vacuum filtration. After that filtrate was washed with deionized water and ethanol. Finally, the products were dried in vacuum oven at 80 °C for 10 hours.

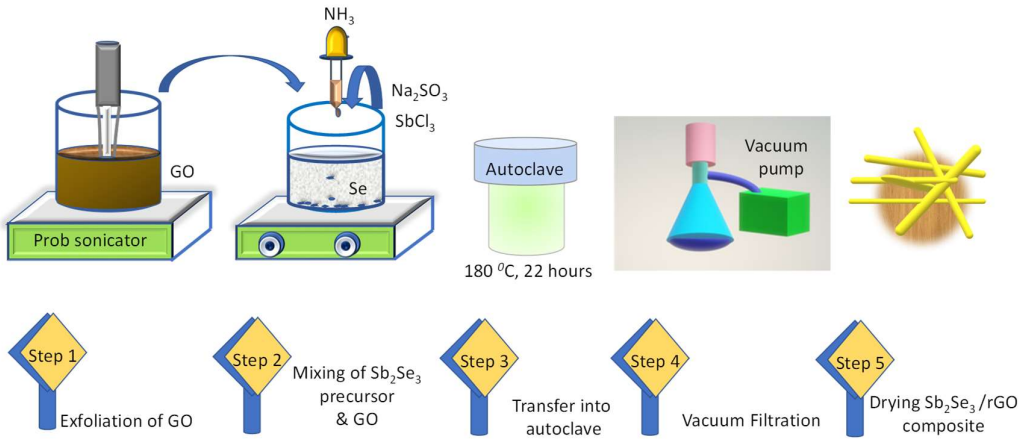

Figure 4.1. *Schematic of the synthesis procedure of Sb_2Se_3/rGO hybrid*

4.3. Electrode Preparation

To prepare catalyst ink, first 1.25 mg catalyst was dispersed in 250 µL N, N dimethylformamide (5 mg/mL). Then 6.25 µL 5 wt. % nafion was added into the mixture and ultrasonicated for 30 min. Subsequently, 3 µL of homogeneous catalyst ink was drop casted onto the glassy carbon electrode (catalyst loading of 0.207 mg/cm^2) and dried in vacuum at 60 ℃. Same mass loading was maintained throughout the whole experiment.

4.4. Electrochemical Measurements

All electrochemical measurements were carried out in a three-electrode system (Autolab Metrohm M-204 electrochemical work station) with Ag/AgCl (saturated in 3 M KCl) as reference electrode, graphite rod as counter electrode and catalyst ink modified glassy carbon as the working electrode (3 mm diameter). Electrocatalytic activity was measured in 0.5 M H_2SO_4 aqueous electrolyte solution at 25 ℃. Before starting the measurement high -purity N_2 gas was purged for 30 min to inhibit the incorporation of oxygen and other impurities in water.

HER activity of the bare Sb_2Se_3, rGO and Sb_2Se_3/rGO heterostructure was measured and analyzed by performing cyclic voltammetry (CV) and linear sweep voltammetry (LSV) at a scan rate of 10 mV/s, chronoamperometry and electrochemical impedance spectroscopy (EIS). Nernst equation is employed to calibrate the potential from Ag/AgCl to RHE (Reversible Hydrogen Electrode)

$$E_{RHE} = E_{appl} + 0.059 * pH + E^{\circ}_{Ag/AgCl} (0.197\ V) \quad (2)$$

4.5 Characterizations

The phase of the as synthesized samples was confirmed by X-ray diffraction (XRD). XRD study was performed using Cu Kα radiation, having a wavelength λ = 1.54 Å (Rigaku ultima III X-ray diffractometer). Raman spectroscopy (Witech) was executed to study the purity and attachment of rGO on Sb_2Se_3. Field emission scanning electron microscopy (FESEM, Hitachi, S-4800) and high-resolution transmission electron microscopy (HRTEM, JEOL-JEM 2100) were employed to study the morphology of the samples. Chemical compositions and valance states were determined by X-ray photoelectron spectroscopy (XPS, SPECS, HAS 3500), with Al Kα X-ray source having an energy of 1486.6 eV. In addition, the XPS spectra were analysed by Origin Pro 8.0 software with Shirley background correction. The high-resolution XPS spectra were fitted by Gaussian functions.

4.6 Theoretical Methods

The first-principles calculations were carried out using Vienna ab initio simulation packages (VASP)[34–37] and Projector-augmented-wave (PAW)[38] approach. To study the Exchange-Correlation contribution we have used PBE functional within GGA approximation. Γ centered (1×1×1) k-points grid was implemented during the geometry optimizations of the sufficiently large supercell as 2x9 and 3x10 of rGO to agree with the lattice parameters of (230) and (001) plane of Sb_2Se_3 respectively. a-axis rGO is rotated along (210) direction to make the hetero-structures with these planes of Sb_2Se_3. Lattice parameters of rGO after this rotation become 4.31 Å and 2.49 Å along a-axis and b-axis respectively. The strains induced

along a axis and b axis while making heterostructure with (230) and (001) plane of Sb_2Se_3 are represented in the Table 4.1

Table 4.1: Strain calculation

System	Strain along a axis	Strain along b axis
(230)-Sb_2Se_3/rGO	0.6 %	2.93 %
(001)-Sb_2Se_3/rGO	5.5 %	0.57 %

PBE+D2 forcefield (Grimme's)[39] method was followed to include van der Walls interaction. Energy cut off for plane wave basis was taken as 500 eV. All the calculations were carried out in spin unrestricted manner. Monolayer of completely reduced graphene oxide (rGO), (230) and (001) surfaces of Sb_2Se_3 and their heterostructure were optimized separately under same conditions. HER activity of reduced graphene oxide (rGO), (230) and (001) surfaces of Sb_2Se_3 along with their heterostructure were studied using the following equation

$$\Delta G = \Delta E + \Delta ZPE - T\Delta S \quad (3)$$

Where ΔE is the change in enthalpy obtained from DFT calculations. ΔS is the change in entropy during the reaction and ΔZPE is the zero-point energy. The values of entropy-temperature term are taken from the standard table for gas-phase molecules.[40] We obtained free energy differences for each reaction step considering final reaction step as a reference. Bader charge analysis was performed to get further insight into HER activity. Charge density difference plot was

calculated using the following equation to understand the electron flow among the fragments in the particular system

$$\Delta\rho = \rho_{AB} - \rho_A - \rho_B \quad (4)$$

where $\Delta\rho_{AB}$ is the charge density of the composite AB, ρ_A and ρ_B are the charge density of A and B respectively.

4.7 Results & Discussion

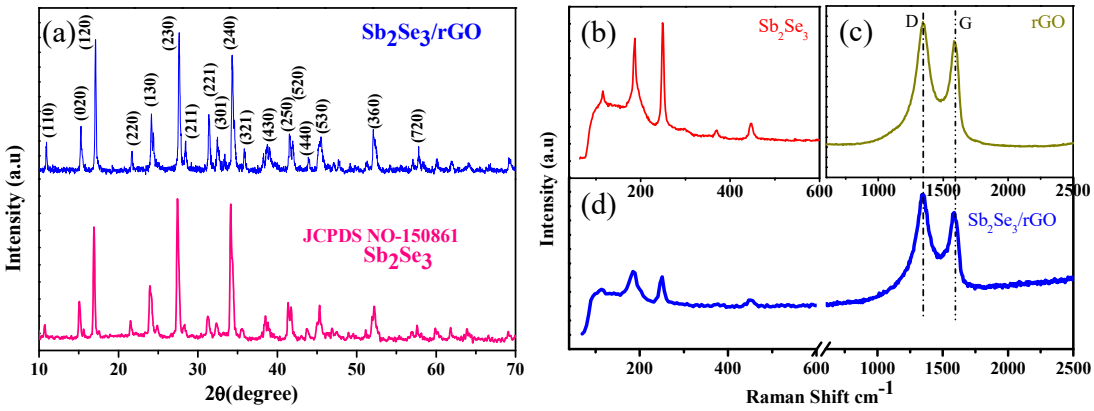

Figure 4.2 *XRD patterns of (a) Sb_2Se_3 and Sb_2Se_3/rGO, Raman spectra of (b) Sb_2Se_3, (c) rGO and (d) Sb_2Se_3/rGO*

The phase purity of the as synthesized Sb_2Se_3 and Sb_2Se_3/rGO hybrid are confirmed by XRD study. Figure 4.2(a) display XRD patterns of both Sb_2Se_3 and its hybrid with rGO. Strong diffraction peaks at 2□ = 10.7° (110), 15.0° (020), 16.9° (120), 21.5° (220), 23.9° (130), 27.4° (230), 28.3° (211), 31.2° (221), 32.3° (301), 34.1° (240), 35.6° (321), 38.5° (430), 41.3° (250), 43.7° (440), 45.3° (530), 52.2° (360) and 57.6° (720) illustrate the polycrystalline nature of as synthesized Sb_2Se_3 nanorods, corresponding to orthorhombic phase with space group *Pbnm (62)* (JCPDS card No.15-0861). However, no detectable XRD intensity of rGO is found which might be

due to the low content of rGO as well as the loss of stacking order of rGO nanosheets. Principally, during growth of the hybrid Sb_2Se_3/rGO samples, the Sb_2Se_3 nanorods are intercalated in between the rGO layers which destroys the stacking order of the rGO layers. [41-43]

Raman spectra of pristine Sb_2Se_3, rGO and Sb_2Se_3/rGO are shown in the Figure 4.2(b), 4.2(c) and 4.2(d) respectively. In the Raman spectrum (Figure 4.2b) of Sb_2Se_3 prominent peaks at 115, 187, 251, 369 and 446 cm^{-1} are clearly observed which indicate the formation of phase pure Sb_2Se_3 in the solvothermal synthesis route.[44-48] The peak at 115 cm^{-1} is associated with the vibrational mode of Se-Se bond. The Raman peak at 187 cm^{-1} is related to the Sb-Se heteropolar stretching vibrational mode in the $Sb_2Se_{3/2}$ pyramids. Whereas peak at 251 cm^{-1} correspond to the Sb-Sb bond in (Se_2Sb-$SbSe_2$) structural unit. The Raman shifts at 369 and 446 cm^{-1} are attributed to the Sb-Se stretching vibrations. Nevertheless, the Raman spectrum of bare of rGO (Figure 4.2c) exhibits two broad peaks centered at 1347 and 1593 cm^{-1} which are identified to be D and G band respectively confirming the formation of rGO.[49] D and G bands are associated with disordered induced and high frequency E_{2g} first order mode.

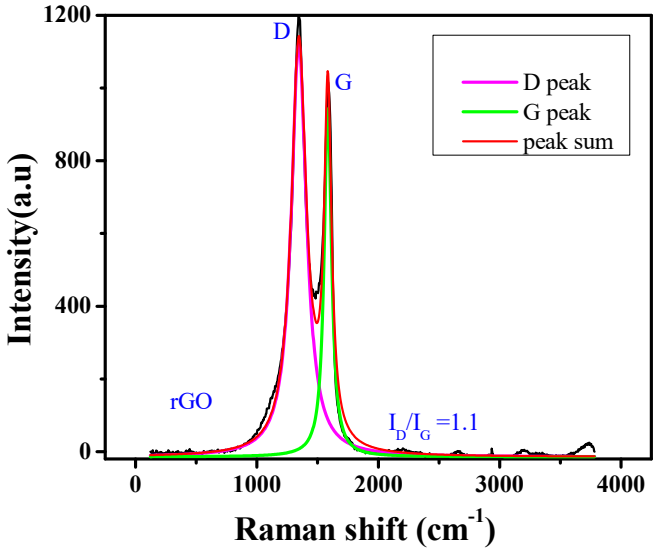

Figure 4.3 *Deconvoluted D and G band of rGO*

The I_D/I_G intensity ratio of rGO is calculated to be 1.1. which is the signature of the good reduction of GO (Figure 4.3).[50-51] Raman spectrum of Sb_2Se_3/rGO (Figure 4.2d) displays the above-mentioned peaks of Sb_2Se_3 along with well-known D (1347cm^{-1}) and G (1593 cm^{-1}) bands of rGO confirming the successful formation of hybrids.

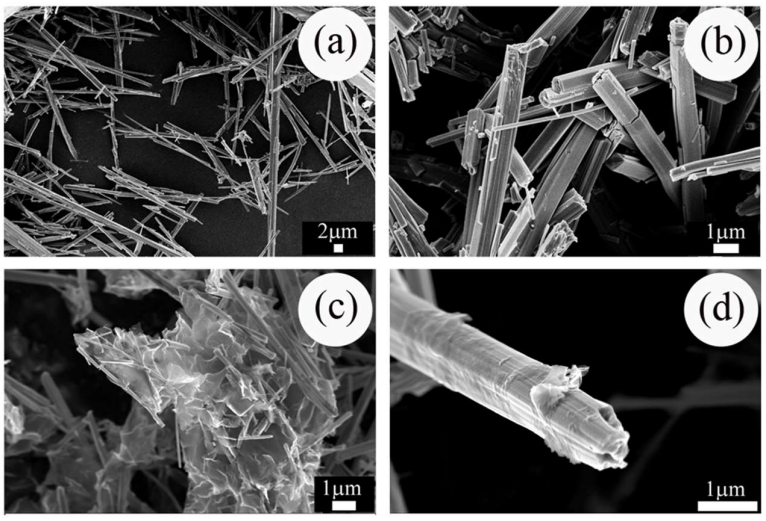

Figure 4.4. *High and low magnification FESEM images of (a, b) bare Sb_2Se_3 nanorods and (c, d) Sb_2Se_3/rGO*

Figure 4.4(a-b) display the FESEM micrographs in low and high magnification, demonstrating 1D rod like structure of as prepared Sb_2Se_3. The Sb_2Se_3 nanorods are well separated and not agglomerated to each other. The length and diameter of the rods are ~ 25 μm, 700 nm respectively. The conductive nanosheets of rGO in Sb_2Se_3/rGO hybrid are prominent in FESEM image in figure 4.4(c). It is evident that rGO makes interconnected conductive network, creating heterointerfaces with Sb_2Se_3 nanorods. The magnified view of FESEM micrograph of Sb_2Se_3/rGO (Figure 4.4(d)) evinces attachment of rGO with Sb_2Se_3 nanorods, demonstrating heterointerface formation between the pristine rGO layers and Sb_2Se_3 nanorods.

In addition to the FESEM study, TEM images also display the formation of hybrid structure of Sb_2Se_3/rGO (Figure 4.5). A closer observation of figure 4.5(a) shows the intimate attachment between layered nanosheet and Sb_2Se_3 nanorod. The separation between the consecutive layers of the nanosheet is found to be ~ 0.334 nm,

confirming the formation of rGO layers. HRTEM image (Figure 4.5(b)) shows the lattice spacing ~ 3.025 nm corresponding to the (211) plane of orthorhombic phase of Sb_2Se_3. Inset of the figure 4.5(b) represents the selected area electron diffraction (SAED) pattern of Sb_2Se_3 nanorod where (440) and (211) planes are observed which corroborates with the polycrystalline Sb_2Se_3 in XRD pattern.

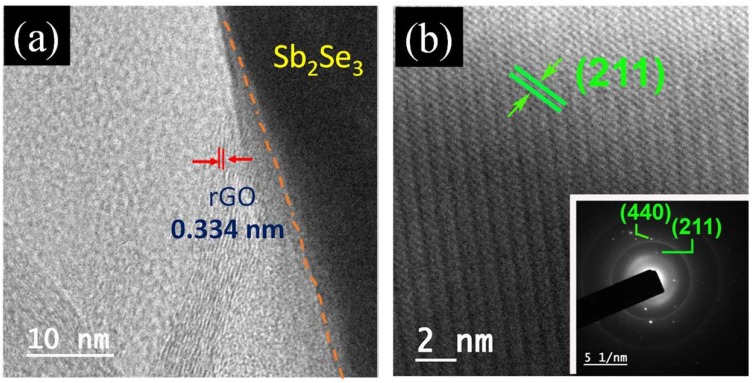

Figure 4.5. *(a) TEM image of Sb_2Se_3/rGO hybrid and (b) HRTEM image of Sb_2Se_3/rGO [inset: SAED pattern]*

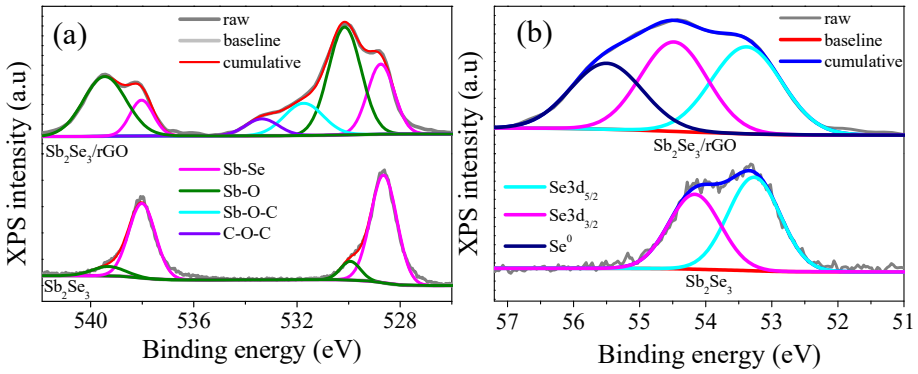

Figure 4.6. *XPS core level spectra of (a) Sb 3d and (b) Se 3d of Sb_2Se_3 and Sb_2Se_3/rGO hybrid respectively*

XPS study was employed to determine chemical constituents of the samples and their chemical oxidation state. The deconvoluted core level spectrum of Sb in figure 4.6(a) display Sb-$3d_{3/2}$ and Sb-$3d_{5/2}$ peaks at 537.9 and 528.6 eV, respectively which indicates +3 oxidation state of Sb element in Sb_2Se_3 nanorods.[52–55] Moreover, oxide peaks appear at 539.3 and 529.7 eV owing to the surface oxidation of hybrid sample, which are also accompanied with core level spectrum of O 1s (Figure 4.7(a)).[52–55]However, in XRD pattern and Raman spectrum analysis, no oxide peak is detected which indicates small quantity of surface oxides. Moreover, we have deconvoluted the Se 3d core level spectrum (Figure 4.6(b)) of Sb_2Se_3 which shows Se $3d_{5/2}$ (53.3 eV) and Se $3d_{3/2}$ (54.2 eV) doublets, corresponding to -2 oxidation states of Se. Additionally, small quantity of residual Se is detected at 55.5 eV in the Sb_2Se_3/rGO hybrid which might be corelated to surface oxidation of Sb species.[54] However, there is no oxidation peak of Se (Se-O peak) which generally appears beyond 58 eV.[55] Importantly, in Sb_2Se_3/rGO hybrid sample, the core level spectra of Sb 3d and Se 3d are shifted towards higher binding energy, indicating the increased oxidation state of Sb and Se, owing to the hybridization with oxygen-functional group of rGO. Moreover, in case of core level spectra of Sb 3d, mainly in O 1s region of the Sb_2Se_3/rGO hybrid sample we observed two additional peaks in 531.7 and 533.4 eV respectively which is ascribed to the Sb-O-C and C-O-C or C-OH bond respectively.[56]

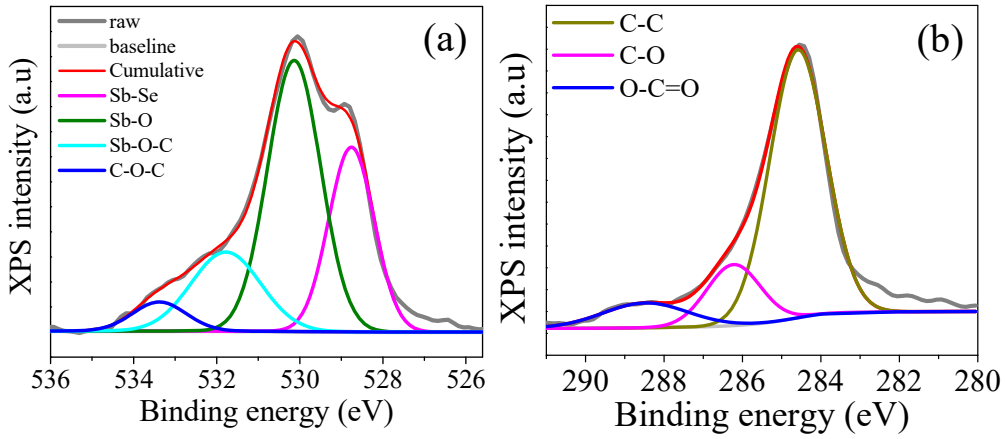

Figure 4.7. *XPS core level spectra of (a) O1s and (b) C1s*

Therefore, electronic interaction between rGO and Sb_2Se_3 in the hybrid samples predominantly attributes to the Sb-O-C bond. The core level XPS spectrum of C 1s (Figure 4.7(b)) also demonstrates the C-C, C-O and O-C-O respectively, which includes the possibility of hybridization via making Sb-O-C bond.[49]

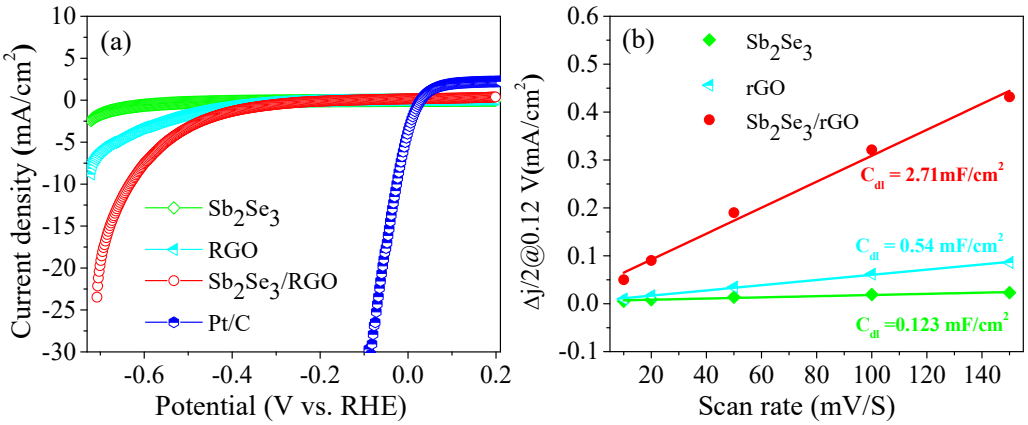

Figure 4.8. *(a) Linear sweep voltammetry curve of as prepared Sb_2Se_3, rGO and Sb_2Se_3/rGO hybrid, (b) Linear fitting of capacitive current as function of scan rate*

LSV measurements of the as synthesized rGO, Sb_2Se_3, Sb_2Se_3/rGO and commercially available standard Pt/C are carried out in 0.5 M H_2SO_4 to compare the electrocatalytic HER performances. Cathodic polarization curves of corresponding samples are represented in figure 4.8(a) which depicts the variation of current density with the applied potential (after iR correction) in the reference scale of reversible hydrogen electrode (RHE). Lower catalytic performances of bare rGO and Sb_2Se_3 nanorods have been observed during LSV measurements compared to their hybrid sample. The electrocatalytic onset potentials for rGO, Sb_2Se_3 are found to be -0.46, -0.64 V respectively. Whereas in case of Sb_2Se_3/rGO hybrids significant reduction of onset potential (-0.32 V) is observed. Here, onset potential is determined by the potential required to detect the first observable current. In addition, Sb_2Se_3/rGO displays a benchmarking current density of -10 mA/cm^2 which is achieved with a 0.63 V overpotential. Although, the bare counterpart of the heterostructure rGO and Sb_2Se_3 could not attain the benchmarking current density in the measured potential window. It is observed from the comparative study of LSV polarization curves that the HER activity becomes superior after attachment of rGO with the Sb_2Se_3 nanorod. Additionally, the HER performances of the Sb_2Se_3/rGO hybrid sample are compared with the literatures based on chalcogenide materials (Table 4.2).

Table 4.2: Comparison table

No.	Catalyst	Mass loaded	Electrolyte	Onset potential	Over potential	Current density	Tafel slope	References
1.	MoS_2	10 µL ink	0.5 M H_2SO_4	-0.23 V vs. RHE	357 mV	-10 mA/cm^2	--	[61]
2.	rGO/MoS_2	20 µg	0.5 M H_2SO_4	-0.13 V vs. RHE	240 mV	-10 mA/cm^2	75 mV/dec	[62]
3.	Carbon nanodot (CD)/MoS_2	--	0.5 M H_2SO_4	-0.50 V vs. RHE	700 mV	-0.5 mA/cm^2	22 mV/dec	[63]
4.	MoS_2/C	252.80 µg/cm^2	0.5 M H_2SO_4	-0.44 V vs. SCE	750 mV	-1.45 mA/cm^2	43 mV/dec	[64]
5.	$NiCo_2S_4$/MoS_2	3 mg/cm^2 (on nickel foam)	0.1 M KCl	-0.40 V vs. RHE	--	--	--	[65]
6.	MoS_2/G	5 µL ink	0.5 M H_2SO_4	-0.11 V vs. RHE	200 mV	-35.50 mA/cm^2	47 mV/dec	[66]
7.	$NiCo_2S_4$/CC	4 mg/cm^2	0.1 M KOH	-0.23 V vs. RHE	263 mV	-50 mA/cm^2	141 mV/dec	[67]
8.	WSe_2-CNF (carbon nanofibers)	--	0.5M H_2SO_4	-0.20 V vs. RHE	158 mV	-10 mA/cm^2	98 mV/dec	[68]
9.	Sb_2Se_3/rGO	3 µL ink	0.5 M H_2SO_4	-0.32 V vs. RHE	630 mV	-10 mA/cm^2	109 mV/dec	This work

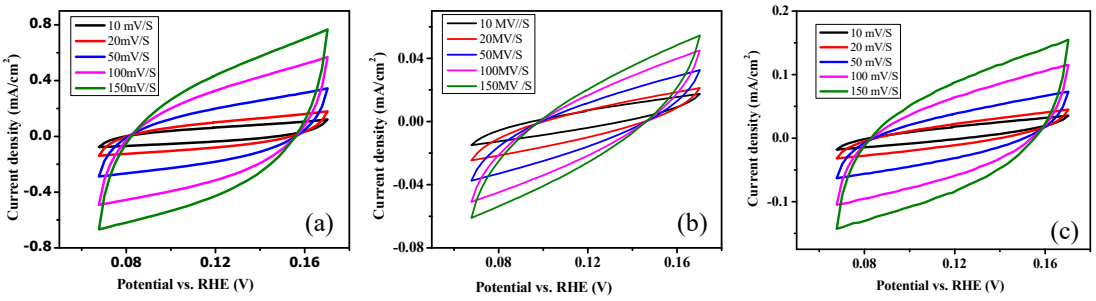

Figure 4.9. *Cyclic voltammetry profile of (a) Sb_2Se_3/rGO (b) Sb_2Se_3 (c) rGO*

Electrochemical active surface area (ECSA) is estimated to get an insight about the improvement of the HER activity of Sb_2Se_3/rGO hybrid. The ECSA is proportional to electrochemical double layer capacitance (C_{dl}) [ECSA= 2*C_{dl}] which is estimated from the linear slope of $\Delta j/2 = (j_a - j_c)/2$ vs. scan rate in figure 4.8(b). Here, j_a and j_c represent anodic and cathodic current density, obtained from the cyclic voltammetry (CV) curve. CV measurements are carried out in the non-Faradic region (voltage window 0.05-0.18 V vs. RHE) at different scan rates 10, 20, 50, 100, 150 mV/s for all the three samples figure 4.9(a), 4.9(b), 4.9(c). The double layer capacitance of rGO, Sb_2Se_3 and Sb_2Se_3/rGO are estimated to be 0.54, 0.123, 2.17 mF/cm^2 respectively. Subsequently, ECSA of Sb_2Se_3 enhances by more than 17 times after synergistic coupling with conductive rGO nanosheets. The heterointerfaces between rGO and Sb_2Se_3 in Sb_2Se_3/rGO offer higher electrochemical active surface area than the intrinsic materials.

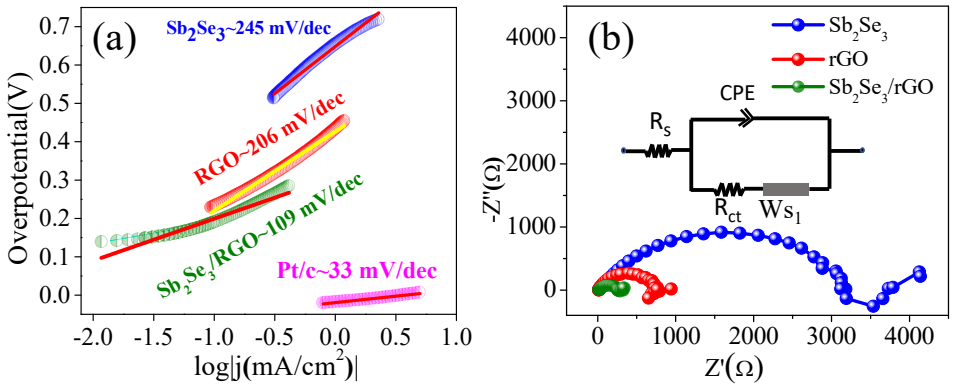

Figure 4.10. *(a) Tafel plot, (b) Electrochemical Impedance Spectroscopy (inset: equivalent circuit model) of as prepared Sb_2Se_3, rGO and Sb_2Se_3/rGO*

To understand the HER reaction kinetics, Tafel plots are derived from the polarisation curves for all the samples (Figure4.10(a)). The reaction pathways can easily be determined from the corresponding Tafel slopes. The Tafel plots in figure 4.10(a) is governed by the Tafel equation [57] which is given as

$$\eta = a + b\,log|j| \qquad (5)$$

The parameters η, a, b & j denote overpotential, intercept, Tafel slope and current density respectively. Tafel slopes are influenced by the reaction kinetics at the electrode-electrolyte interfaces. The values of the Tafel slopes dictate the dominating reaction pathway of HER. The values of the Tafel slopes for Volmer, Heyrovsky and Tafel steps correspond to the Tafel slopes ~ 120, 40, 30 mV/decade.[23] According to our investigation, Sb_2Se_3/rGO demonstrates significant reduction of Tafel slope (109 mV/dec) following Volmer pathway, which is almost two-fold lower than the Sb_2Se_3 nanorods (245 mV/dec) and rGO (206 mV/dec). The values of the Tafel slopes indicate the Volmer is the rate determining step during the HER. Moreover, lower

value of Tafel slope indicates higher catalytic activity and superior type of catalytic active sites, thereby enhancing the HER activity of Sb_2Se_3/rGO.[58]

Table 4.3. EIS parameters of Sb_2Se_3/rGO, rGO, Sb_2Se_3

Name of Sample	**R_s (Ω)**	**R_{ct} (Ω)**	**P1**	**n1**	**Wsr1 ($\mu\Omega^{-1}.cm^{-2}.s^{1/2}$)**	**Wsc1($\mu\Omega^{-1}.cm^{-2}.s^{1/2}$)**
Sb_2Se_3/rGO	11.58	285.94	0.00044	0.60	$2.4*10^{-13}$	5.7
rGO	12	752.74	$7.81*10^{-5}$	0.76	$9.94*10^{-6}$	$9.67*10^{-14}$
Sb_2Se_3	14.21	3290.9	$1.4*10^{-05}$	0.64	$9.6*10^{-14}$	9.95

Moreover, EIS provides further insight regarding the charge transfer at the electrode and electrolyte interfaces. The EIS spectra in figure 4.10(b) are fitted into physically relevant circuit (inset of Figure 4.10(b)) and fitted parameters are provided in Table 4.3. The obtained equivalent series resistances (R_s) are found to be almost equal (12 Ω). Whereas, charge transfer resistances (R_{ct}) of rGO, Sb_2Se_3 and Sb_2Se_3/rGO are 752.74, 3290.9 and 285.94 Ω respectively. Therefore, drastic reduction in R_{ct} of Sb_2Se_3/rGO hybrids promotes facile charge transfer at the interface.

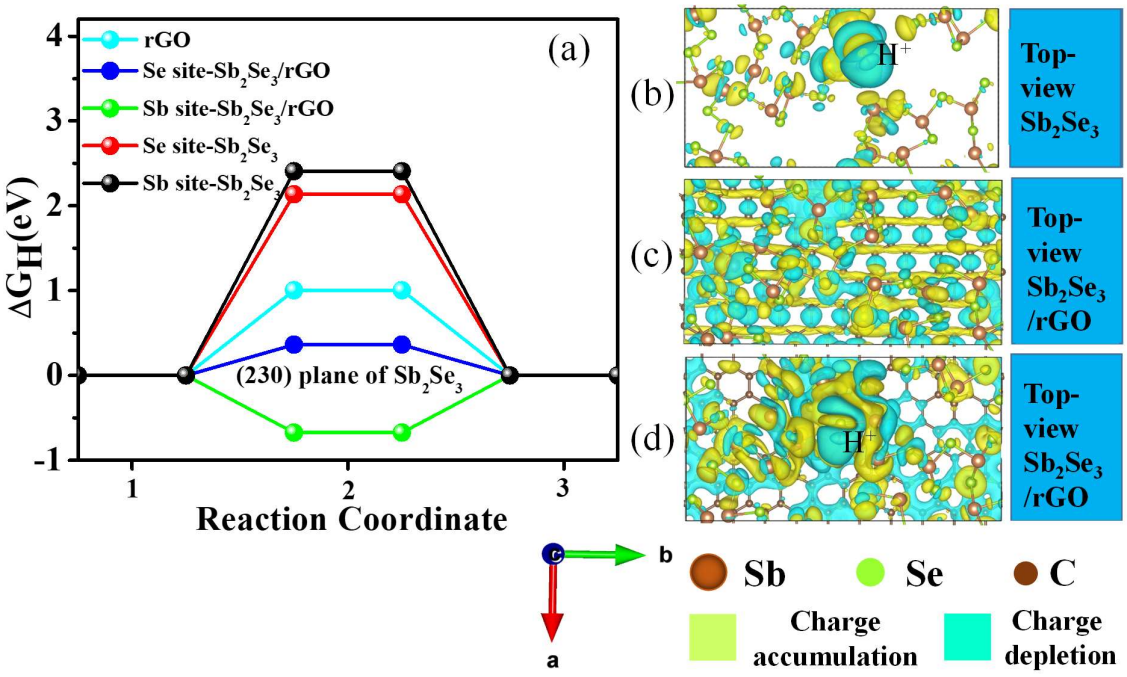

Figure 4.11. *(a) Gibbs free energy diagrams for hydrogen adsorption of rGO, Sb_2Se_3 and Sb_2Se_3/rGO for (230) plane of Sb_2Se_3, Top view of (b) Sb_2Se_3 before H^+ adsorption in Se site, (c) Sb_2Se_3/rGO after H^+ adsorption in Se site, (d) Sb_2Se_3/rGO after H^+ adsorption in Se site*

Fundamental insights of superior HER activity are found from first-principles density functional theory (DFT) calculations. Here, we made heterointerfaces of rGO with (230) and (001) surfaces of Sb_2Se_3, as the (230) peak reflection in XRD pattern is maximum, while anisotropic Sb_2Se_3 offers easier charge carrier migration along (001) direction. [22] Reaction steps of HER activity are as follows-

1) $* + 2H^+ + 2e^- \rightarrow$ 2) $*H + H^+ + e^- \rightarrow$ 3) $* + H_2$, in summary $* + 2H^+ + 2e \rightarrow * + H_2$

Here '*' represents active site of the system for H^+ adsorption. One H^+ ion gets adsorbed to the active site on the electrocatalyst's surface to form a *H configuration, surface adsorbed species and consequently another H^+ interacts with the *H, releasing the H_2 molecule. Gibbs free energy change of hydrogen adsorption (ΔG_H) is

the appropriate descriptor of HER activity and its ideal value in acidic medium is zero. Therefore, the absolute value of Gibbs free energy change of hydrogen adsorption at the specific site of a particular system close to ideal value (i.e., $\Delta G_H = 0$) exhibits efficient electrocatalytic activity for HER. Calculated Gibbs free energy of hydrogen adsorption (ΔG_H) in figure 4.11(a) determines the HER activity of a system. We put forward (230) plane of Sb_2Se_3 and its heterostructure with rGO as (230) Sb_2Se_3 and (230)-Sb_2Se_3/rGO respectively in further detail discussion of HER activity. Our investigation shows that ΔG_H value for Sb sites of (230)-Sb_2Se_3 and (230)-Sb_2Se_3/rGO are 2.40, -0.67 eV respectively, whereas for the Se sites the ΔG_H values are 2.13 eV and 0.36 eV respectively. It is evident that owing to heterointerface formation, we observed significant decrease of the ΔG_H value towards ideal value (i.e., $\Delta G_H = 0$) at individual sites, attributing to improved HER activity of Sb_2Se_3/rGO than the bare Sb_2Se_3. According to the ΔG_H value for hydrogen adsorption in the (230) surface of Sb2Se3/rGO, Sb site (ΔG_H= -0.67 eV) is more thermodynamically favourable than Se site (ΔG_H= 0.36 eV) for H-adsorption, owing to the strong binding of H at Sb site. Therefore, hydrogen evolution reaction is mostly driven by Sb sites and there might be limited interaction at Se sites. It is to be noted that the calculation of the Gibbs free energy in different hydrogen coverage ratio would be helpful in understanding the actual competency between the two sites for HER. [59-60]

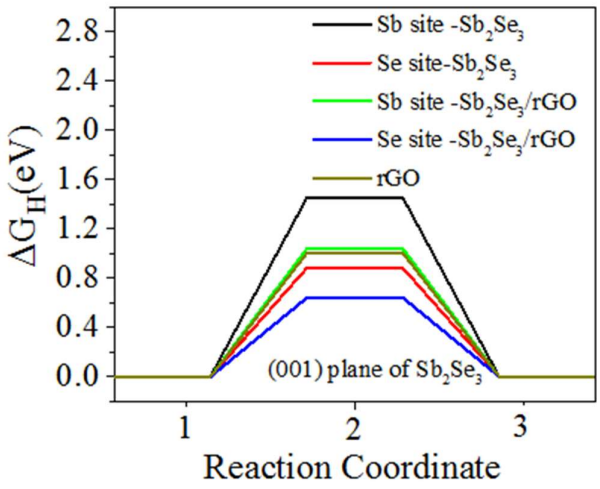

Figure 4.12. *Gibbs free energy diagrams for hydrogen adsorption of rGO, Sb_2Se_3 and Sb_2Se_3/rGO for (001) plane of Sb_2Se_3*

Again, Se site in (001) Sb_2Se_3/rGO (ΔG_H = 0.64 eV) is more active than other sites in (001) plane (Figure 4.12) for hydrogen evolution reaction. Importantly, irrespective of the surfaces, Gibbs free energy of hydrogen adsorption for Se sites are closest to thermoneutral value ($|\Delta G_H|$ for Se Site < $|\Delta G_H|$ for Sb Site). Therefore, one can potentially engineer Se rich surfaces or preferentially expose Se sites for better HER.

The potential of heterointerface design between Sb_2Se_3 and rGO for HER is further demonstrated by Bader charge analysis on selective Se sites. After H atom adsorption on the Se site of (230)-Sb_2Se_3, Se atom and H atom got the Bader charges -0.22524e and -0.05988e respectively that causes columbic repulsive force between the two atoms. In contrast, Se site and H site of (230)-Sb_2Se_3/rGO acquired Bader charges -0.20356e and -0.018238e respectively after H adsorption. This decrease in the values of Bader charges on Se atom and H atom of (230)-Sb_2Se_3/rGO reduces the repulsive force acting between these two atomic sites, which makes ΔG_H value for Se site of (230)-Sb_2Se_3/rGO lower than (230)-Sb_2Se_3 surface. Charge density difference

was studied for (230)-Sb_2Se_3/rGO before and after H^+ adsorption to get charge transfer among its fragments along Z axis of the plane (Figure 4.13 (a-d)).

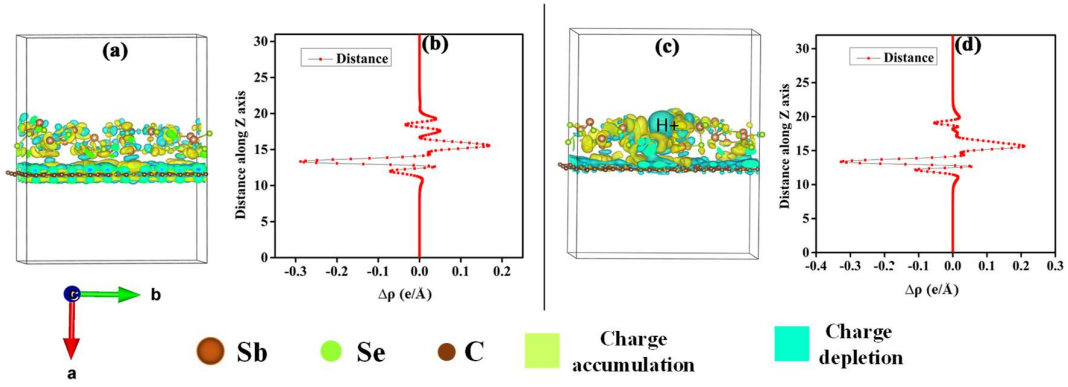

Figure 13. *(a) Charge accumulation and depletion in Sb_2Se_3/rGO before H^+ adsorption (b) Charge density Vs. Distance plot before H^+ adsorption in Sb_2Se_3/rGO (c) Charge accumulation and depletion in Sb_2Se_3/rGO after H^+ adsorption (d) Charge density Vs. Distance plot after H^+ adsorption in Sb_2Se_3/rGO*

We observed that rGO redistributes the charge in the (230)-Sb_2Se_3/rGO system which boosts H^+ adsorption on Se site by reducing charges on these sites and columbic repulsive force. Beside this we also compare charge transfer (top-view in Figure 4.11(b)) difference plots of H^+ adsorbed (230) surface of Sb_2Se_3 and Sb_2Se_3/rGO without and with H^+ adsorption (Figure 4.11(c, d)), which illustrates the charge accumulation and depletion regions. In comparison to (230) plane of Sb_2Se_3, significant amount of electronic charge was depleted at H adsorbed Se site and its neighbouring atoms of the heterostructure indicating the charge transfer to H^+ ion for better adsorption on its surface at Se site. Bader charge analysis was also calculated for the (001)-Sb_2Se_3/rGO to observe the amount of charge transferred to or from H^+ ion adsorbed Sb site and Se site and its nearby atoms before and after H^+

adsorption is listed in Table 4.4 & Table 4.5 (Figure 4.14, 4.15). It is observed that rGO basically reallocates the charges of (001)-Sb_2Se_3 surface and induces HER activity.

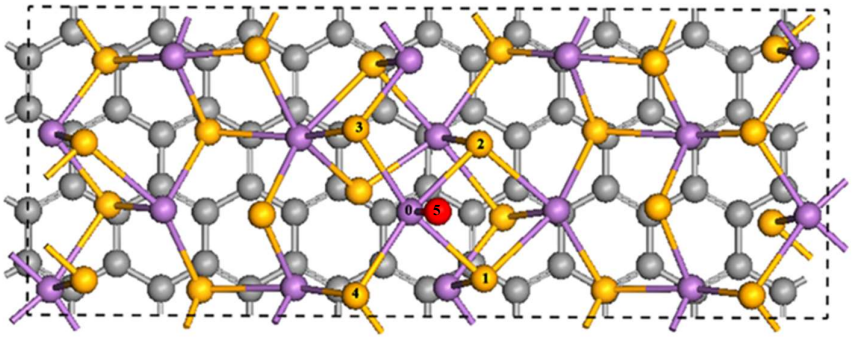

Figure 4.14. *H^+ ion adsorbed on Sb site of heterostructure of Graphene and Sb_2Se_3 where denotes Se atom, denotes Sb atom, denotes C atom and denotes H atom. Bader charge of selected atoms (0, 1, 2, 3 ,4 &5) are shown in the Table 4.4*

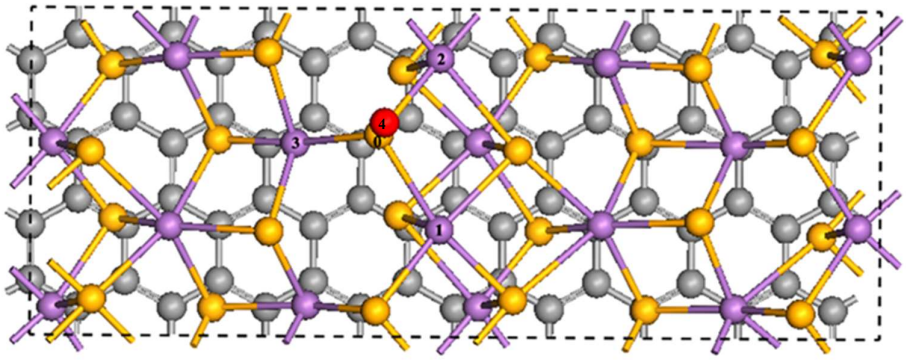

Figure 4.15. *H^+ ion adsorbed on Se site of heterostructure graphene and Sb_2Se_3 where denotes Se atom, denotes Sb atom, denotes C atom and denotes H atom. Bader charge of selected atoms (0, 1, 2 ,3 & 4) are shown in the Table 4.5*

Table 4.4. Bader charge analysis on Sb site before and after H^+ ion adsorption in (001) plane of Sb_2Se_3

Atoms no. denoted in Fig. 4.14	**Bader charges (e) before H^+ ion adsorption on Sb site of heterostructure**	**Bader charges (e) after H^+ ion adsorption on Sb site of heterostructure**
0	0.92	0.95
1	-0.64	-0.62
2	-0.63	-0.62
3	-0.58	-0.58
4	-0.60	-0.59
5	0	-0.27

Table 4.5. Bader charge analysis on Se site before and after H^+ ion adsorption in (001) plane of Sb_2Se_3

Atoms no denoted in Fig. 4.15	Bader charges (e) before H^+ ion adsorption on Se site of heterostructure	Bader charges (e) after H^+ ion adsorption on Se site of heterostructure
0	-0.60	-0.30
1	0.87	0.89
2	0.93	0.80
3	0.92	0.90
4	0	-0.04

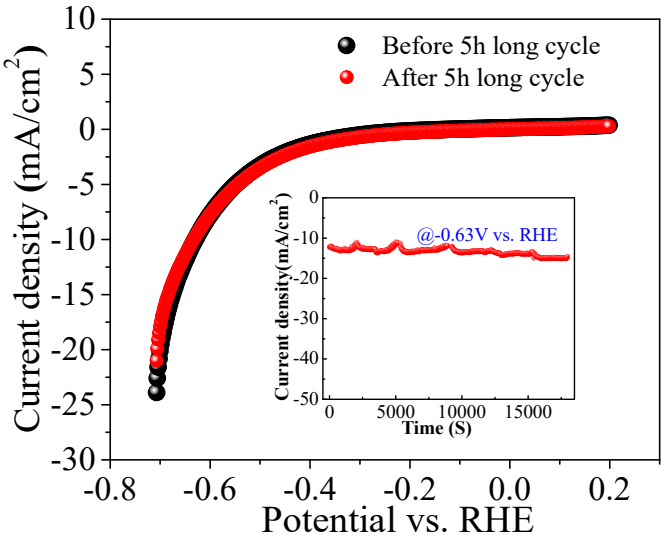

Figure 4.16. *LSV profile of Sb_2Se_3/rGO before and after 5 hours of operation; inset shows the stability of Sb_2Se_3/rGO hybrid by using RDE*

Electrocatalytic activity regarding real life industrial application is mainly investigated by measuring current density variation with time i.e., chronoamperometry or voltage variation with time i.e., chronopotentiometry. Here we performed chronoamperometry in acidic media (0.5 M H_2SO_4) for 5 hours by using rotating disc electrode (RDE) at 1600 rpm. figure 4.16 depicts the faradic current polarization curve of Sb_2Se_3/rGO before and after performing the long cycle. From inset of figure 4.16 it has been clearly observed that no substantial change in faradic current density occurs around the -0.63V versus RHE during long cycle measurement. Chronoamperometry measurement indicates that there is no significant degradation of sample during long cycle.

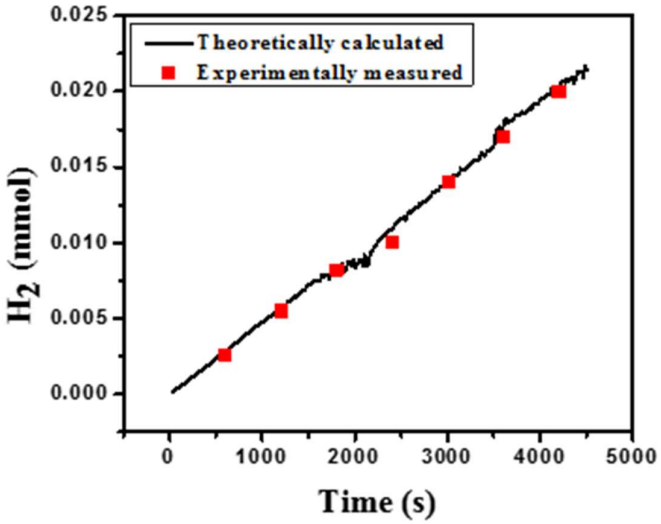

Figure 4.17: *Theoretically calculated and experimentally measured value of H_2 evolution amount*

Importantly, Sb_2Se_3/rGO hybrid offers 96 % Faradaic efficiency (figure 4.17). Moreover, we have performed TEM after 1000 cycle CV cycle which shows that Sb_2Se_3 retains their rod like structure even after 1000 cycle of CV measurement. Also,

HRTEM image shows the (220) plain of Sb_2Se_3, in the Sb_2Se_3/rGO hybrid even after 1000 cycle of CV measurement which corroborates well with the XRD pattern. (Figure 4.18)

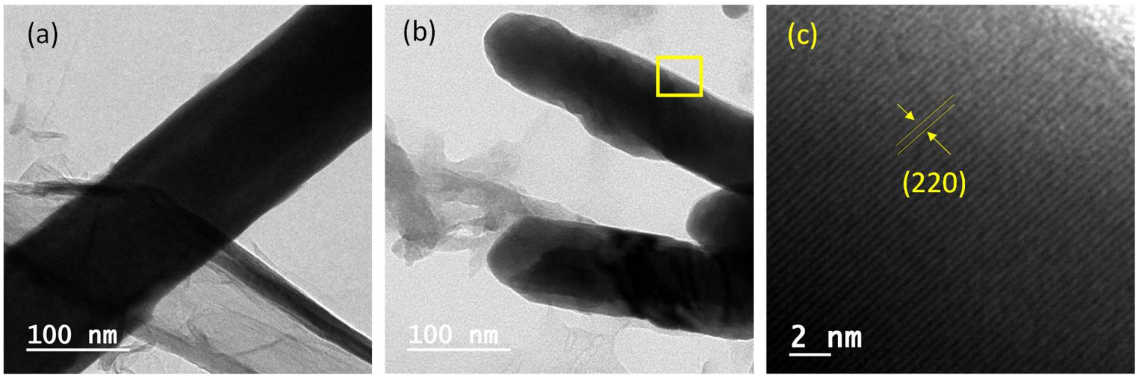

Figure 4.18: *TEM images of (a) Sb_2Se_3/rGO hybrid before 1000 cycle CV measurement, (b) Sb_2Se_3/rGO hybrid after 1000 cycle CV measurement and (c) HRTEM image of Sb_2Se_3/rGO hybrid after 1000 cycle CV measurement*

4.8. Conclusions

In conclusion, we have successfully synthesized Sb_2Se_3/rGO hybrid via one-step solvothermal approach and employed the hybrid as hydrogen evolution electrocatalyst. In this approach, Sb_2Se_3 nanorods grows during the reduction of GO leading to the formation of interconnected conductive rGO network, generating enormous heterointerfaces between the two. It is observed that the hybrid shows significant reduction of the onset potential as low as - 0.32 V with lowering the Tafel slope 109 mV/dec than the pristine samples in the acidic medium. Importantly, heterointerface formation into the hybrid leads to the increase of catalytically exposed active sites and also reduces charge transfer resistance. According to theoretical investigations, the Gibbs free energy of the

H^+ adsorption in the active sites of (001) plane and (230) plane reduces significantly, owing to the reduced coulombic repulsion. Principally, rGO redistributes the charges in the Sb_2Se_3/rGO heterointerfaces which increases H^+ adsorption on Se site by reducing charges on these sites. Hence, the combination of theory and experimental results suggest that heterointerface formation significantly boosts the electrocatalytic HER performances of Sb_2Se_3 nanorods. Therefore, this work promotes future scope of investigating Sb_2Se_3 and similar chalcogenide materials based heterointerfaces to obtain site selective advanced HER catalysts.

References

1. Lim, K. R. G.; Handoko, A. D.; Johnson, L. R.; Meng, X.; Lin, M.; Subramanian, G. S.; Anasori, B.; Gogotsi, Y.; Vojvodic, A.; Seh, Z. W. *ACS Nano* 2020, ***14***, 16140–16155.

2. She, Z. W.; Kibsgaard, J.; Dickens, C. F.; Chorkendorff, I.; Nørskov, J. K.; Jaramillo, T. F. *Science* 2017, ***355***, 146-158.

3. Dai, Z.; Du, X.; Wang, Y.; Han, X.; Zhang, X. Dalton Trans. 2021, **50**, 12301-12307.

4. Du, X.; Ding, Y.; and Zhang, X. *Appl. Surf. Sci.* 2021, **562**, 150227-150239.

5. Liang, G.; Zheng, Z.; Fan, P.; Luo, J.; Hu, J.; Zhang, X.; Ma, H.; Fan, B.; Luo, Z.; Zhang, D. *Sol. Energy Mater. Sol. Cells* 2018, ***174***, 263–270.

6. R, Krishnan.; M, Robert.; L, Stuart. *Solar Hydrogen Generation* Springer, 2008.

7. Ghavam, S.; Vahdati, M.; Wilson, I. A. G.; Styring, P. *Front. Energy Res.* 2021, ***9*** ,

1–19.

8. Fan, L.; Tu, Z.; Hwa, S. *Energy Rep.* 2021, **7**, 8421–8446.

9. Chen, S.; Liu, T.; Zheng, Z.; Ishaq, M.; Liang, G.; Fan, P.; Chen, T.; Tang, J. *J. Energy Chem.* 2022, ***67***, 508–523.

10. Voiry, D.; Shin, H. S.; Loh, K. P.; Chhowalla, M. Nat. Rev. Chem. 2018**, 2**, 0105.

11. Schlapbach, L.; Züttel, A. Nature 2001, ***414***, 353–358.

12. Jin, H.; Guo, C.; Liu, X.; Liu, J.; Vasile, A.; Jiao, Y.; Zheng, Y.; Qiao, S. *Chem. Rev.* 2018, ***118***, 6337−6408.

13. Lv, R.; Robinson, J. A.; Schaak, R. E.; Sun, D.; Sun, Y.; Mallouk, T. E.; Terrones, M. *Acc. Chem. Res.* 2015, ***48***, 1, 56–64

14. Yan, H.; Tian, C.; Wang, L.; Wu, A.; Meng, M.; Zhao, L.; Fu, H. *Angew. Chem.* 2015, ***127***, 6423-6427.

15. Meng, C.; Chen, X.; Gao, Y.; Zhao, Q.; Kong, D.; Lin, M.; Chen, X.; Li, Y.; Zhou,Y. *Molecules* 2020, ***25***, 1136-1154**.**

16. Yan, Y.; Xu, S.; Li, H.; Selvam, N. C.; Lee, J.Y.; Lee, H.; Yoo, P. J. *Chem. Eng. J.* 2021, ***405***, 126728-126736.

17. Yang, J.; Voiry, D.; Ahn, S. J.; Kang, D.; Kim, A. Y.; Chhowalla, M.; Shin, H. S. *Angew. Chem.* 2013, **52**, 13751–13754.

18. Peng, X.; Yan, Y.; Jin, X.; Huang, C.; Jin, W.; Gao, B.; Chu, P. K. Nano Energy. 2020, ***78***, 105234-105257.

19. Tian, Y.; Sun, Z.; Zhao, Y.; Zhang, Y.; Tan, T.; Yin ,F. J. Nanopart. Res. 2019, **21**, 1–15.

20. An, D.; Chen, S.; Lu, Z.; Li, R.; Chen, W.; Fan, W.; Wang, W.; Wu, Y. *ACS Appl. Mater. Interfaces* 2019, ***11***, 27788–27797.

21. Wang, L.; Li, D.; Li, K.; Chen, C.; Deng, H.; Gao, L.; Zhao, Y. Nat. Energy 2017, **2**, *17046*-17055.

22. Song, H.; Li, T.; Zhang, J.; Zhou, Y.; Luo, J.; Chen, C.; Yang, B. Adv. Mater. 2017, **29**, *1700441-1700448*.

23. Zhao, G.; Rui, K.; Dou, S. X.; Sun, W. *Adv. Funct. Mater.* 2018, **28**, *1803291*-1803317.

24. Lei, Y.; Pakhira, S.; Fujisawa, K.; Wang, X.; Iyiola, O. O.; Elías, A. L.; Rajukumar, L. P.; Zhou, C.; Kabius, B.; Alem, N.; Endo, M.; Lv, R.; Mendoza-cortes, J. L.; Terrones, M. *ACS Nano* 2017, ***11****(5)*, 5103–5112.

25. Yang, Z.; He, R.; Wu, H.; Ding, Y.; Mei, H. *Int. J. Hydrogen Energy* 2020, ***46****(15)*, 9690–9698.

26. Wang, Y.; Lu, F.; Su, K.; Zhang, N.; Zhang, Y.; Wang, M.; Wang, X. *Chem. Eng. J.* 2020, ***399***, 126018.

27. Chung, D. Y.; Jun, S. W.; Yoon, G.; Kim, H.; Yoo, J. M.; Lee, K.; Shin, H.; Sinha, A. K.; Kwon, S. G.; Kang, K.; Hyeon, T.; Sung, Y. *J. Am. Chem. Soc.* 2017, ***139***, 6669–6674.

28. Li, Y.; Wang, H.; Xie, L.; Liang, Y.; Hong, G.; Dai, H. *J. Am.Chem.Soc.* 2011**, *133*,** 7296–7299.

29. Liao, L.; Zhu, J.; Bian, X.; Zhu, L.; Scanlon, M. D.; Girault, H. H. *Adv. Funct. Mater.* 2013, ***23***, 5326-5333.

30. Cai, Z.; Song, X.; Wang, Y.; Chen, X. *ChemElectroChem* 2015, ***2***, 1665–1671.

31. Ding, P.; Meng, C.; Liang, J.; Li, T.; Wang, Y.; Liu, Q.; Luo, Y.; Cui, G.; Asiri, A.M.; Lu, S.; Sun, X. Inorg. Chem. 2021, ***60***, 12703-12708.

32. Wang, D.; Yu, D.; Mo, M.; Liu, X.; Qian, Y. J. Cryst. Growth 2003, ***253***, 445–451.

33. Jili, W.; Xiaoping, S.; Lei, J.; Kun,W.; Kangmin, C. Appl. Surf. Sci. 2010, ***256***, 2826-2830.

34. Kresse, G.; Furthmiiller, J.; Hafner, J. *Phy. Rev. B* 1994, ***50***, 181–185.

35. Kresse, G.; Furthmiiller, J. Comput. Mater. Sci., ***6***, 15–50.

36. Kresse, G.; Furthmüller, J. *Phy. Rev. B* 1996, ***54***, 11169-11186.

37. Kresse, G.; Hafner, J. *Phy. Rev. B* 1993, ***47***, 558-561.

38. Du, Y.; Ouyang, C.; Shi, S.; Lei, M.; Du, Y.; Ouyang, C.; Shi, S.; Lei, M. J. Appl. Phys. 2010, ***107***, 093718.

39. Grimme, S.; Chemie, T. O.; Münster, O. I. D. U. Semiempirical GGA-Type J. Comput. Chem. 2006, ***27***, 1787-1799.

40. Nørskov, J.K.; Rossmeisl, J.; Logadottir, A.; Lindqvist, L.R.K.J.; Kitchin, J.R.; Bligaard, T.; Jonsson, H. J. Phys. Chem. B 2004, ***108***, 17886-17892.

41. Liu, J.; Bai, H.; Wang, Y.; Liu, Z.; Zhang, X.; Sun, D.D.. *Adv. Funct. Mater.* 2010, ***20***, 4175-4181.

42. Dong, P.; Wang, Y.; Cao, B.; Xin, S.; Guo, L.; Zhang, J.; Li, F. Appl. Catal., B 2013, ***132***, 45-53.

43.Jiang, G.; Lin, Z.; Chen, C.; Zhu, L.; Chang, Q.; Wang, N.; Wei, W.; Tang, H. *Carbon* 2011, ***49***, 2693-2701.

44. Vidal-fuentes, P.; Guc, M.; Alcobe, X.; Jawhari, T.; Placidi, M. *2D Mater.*2019, ***6***, 045054-045066.

45. Kong, P. P.; Sun, F.; Xing, L. Y.; Zhu, J.; Zhang, S. J.; Li, W. M.; Liu, Q. Q.; Wang, X. C.; Feng, S. M.; Yu, X. H.; Zhu, J. L.; Yu, R. C.; Yang, W. G.; Shen, G. Y.; Zhao, Y. S.; Ahuja, R.; Mao, H. K.; Jin, C. Q. *Sci. Rep.* 2014, ***4***, 6679-6703.

46. Tao, J.; Hu, X.; Xue, J.; Wang, Y.; Weng, G.; Chen, S.; Zhu, Z.; Chu, J. Sol. Energy Mater. Sol. Cells 2019, ***197***, 1–6.

47. Shongalova, A.; Correia, M. R.; Vermang, B.; Cunha, J.M.V.; Salome, P.M.P.; Fernandes, P.A. MRS Commun. 2018, ***8***, 865–870.

48. Fleck, N.; Hobson, T. D. C.; Savory, C. N.; Buckeridge, J.; Veal, T. D.; Correia, M. R.; Scanlon, D. O. *J. Mater. Chem. A* 2020, ***8***, 8337–8344.

49. Yang, Z.; Li, W.; Zhang, G.; Wang, J.; Zuo, J.; Xu, Q.; Shan, H.; He, X.; Lv, M.; Hu, J.; Huang, W.; Zhang, J.; Li, X. *Nano Energy* 2022, ***93***, 106764-106776 .

50. Sarkar, S.; Howli, P.; Das, B.; Das, N.S.; Samanta, M.; Das, G.C.; Chattopadhyay, K.K. *ACS Appl. Mater. Interfaces* 2017, **9**, 22652-22664.

51. Fang, S.; Huang, D.; Lv, R.; Bai, Y.; Huang, Z.H.; Gu, J.; Kang, F. RSC Adv. 2017**, *7***, 25773-25779.

52. Liu, X.; Chen, J.; Luo, M.; Leng, M.; Xia, Z.; Zhou, Y.; Qin, S.; Xue, D.; Lv, L.; Huang, H.; Niu, D.; Tang, J.. *ACS Appl. Mater. Interfaces* 2014, ***6***, 10687–10695.

53. Prabhakar, R. R. ; Septina, W.; Siol, S.; Moehl, Thomas.; Wick-Joliat, R.; Tilley, S.D. *J. Mater. Chem. A.* 2017, **5**, 23139–23145.

54. Wang, C.; Lu, S.; Li, S.; Wang, S.; Lin, X.; Zhang, J.; Kondrotas, R.; Li, K.; Chen, C.; Tang, J. *Nano Energy* 2020, ***71***, 104577-104588.

55. Wen, S.; Yin, X.; Xie, H.; Guo, Y.; Liu, J.; Liu, D. *J. Adv. Dielectr.* 2020, ***10***, 2050016-2050022.

56. Ou, X.; Yang, C.; Xiong, X.; Zheng, F.; Pan, Q.; Jin, C.; Liu, M.; Huang, K. A Adv. Funct. Mater. 2017, ***27***, 1606242-1606252.

57. Maity, S.; Das, B.; Samanta, M.; Das, B.K.; Ghosh, S.; Chattopadhyay, K.; ACS Appl. Energy Mater. 2020, ***3***, 5067-5076.

58. Fan, Ke.; Chen, H.; Ji, Y.; Huang, H.; Martin, P. C.; Daniel, Q.; Philippe, B.; Rensmo, H.; Li, F.; Luo, Yi.; Sun, L. *Nat. Commun*. 2016, **7**, 11981-11990.

59. Seh, Z. W.; Fredrickson, K. D.; Anasori, B.; Kibsgaard, J.; Strickler, A. L.; Lukatskaya, M. R.; Gogotsi, Y.; Jaramillo, T. F.; Vojvodic, A. *ACS Energy Letters* 2016, **1**, 589−594.

60. Mou, J.; Gao, Y.; Wang, J.; Ma, J.; Ren, H. *RSC Adv.* 2019, **9**, 11755–11761.

61. Ravikumar, C.H.; Nair, G.V.; Muralikrishna, S.; Nagaraju, D.H.; Balakrishna, R.G. *Materials Letters*, 2018, ***220***, 133-135.

62. Liu, Y.; Liu, J.; Li, Z.; Fan, X.; Li, Y.; Zhang, F.; Zhang, G.; Peng, W.; Wang, S. *Int. J. Hydrogen Energy*, 2018, ***43****(30)*, 13946-13952.

63. Canton-Vitoria, R.; Vallan, L.; Urriolabeitia, E.; Benito, A.M.; Maser, W.K.; Tagmatarchis, N. *Chem. Eur. J.*, 2018, ***24****(41)*, 10468-10474.

64. Rowley-Neale, S.J.; Ratova, M.; Fugita, L.T.; Smith, G.C.; Gaffar, A.; Kulczyk-Malecka, J.; Kelly, P.J.; Banks, C.E. *ACS Omega*, 2018, ***3****(7)*, 7235-7242.

65. Jia, Y.; Ma, Y.; Lin, Y.; Tang, J.; Shi, W.; He, W. *Electrochim. Acta*, 2018, ***289***, 39-46.

66. Zhang, X.; Zhang, Q.; Sun, Y.; Zhang, P.; Gao, X.; Zhang, W.; Guo, J. *Electrochim. Acta*, 2016, ***189***, 224-230.

67. Liu, D.; Lu, Q.; Luo, Y.; Sun, X.; Asiri, A.M. *Nanoscale*, 2015, **7***(37)*, 15122-15126.

68. Zou, M.; Chen, J.; Xiao, L.; Zhu, H.; Yang, T.; Zhang, M.; Du, M. *J. Mater. Chem. A*, 2015, ***3****(35)*, 18090-18097.

Chapter 5

Strong non-linear optical response of Sb_2Se_3 nanorods suspension based on spatial self-phase modulation and their all-optical photonic device applications

In this work, spatial self-phase modulation (SSPM) experiments have been conducted using the emerging anisotropic layered material Sb_2Se_3 in a liquid suspension, aiming for applications in all-optical diodes and all-optical switching. The third-order broadband nonlinear optical susceptibility (χ (3) ~ 10^{-9} esu) and nonlinear refractive index (n_2 ~ 10^{-6} cm^2/W) of Sb_2Se_3 were measured using a 671 nm laser beam. The exploration of nonlinear optical phenomena in Sb_2Se_3 is the key focus of this chapter.

This chapter has been published in Nanoscale.

Sen, Nabanita, et al. *Nanoscale* 2023, 15, 19671-19680

5.1. Introduction

The future of optical communication depends on the use of all-optical modulation technology. [1-3,4] Optical modulation refers to the alteration of an optical signal's phase, amplitude and other parameters through physical means. This can be done either directly from the light source or through an external electric or optical field. [1,5-7] The strength of optical modulation is influenced by both the materials' nonlinear properties and the propagation path. [1,5-7] It is necessary to investigate the nonlinear properties of new quantum materials, specifically the nonlinear refractive index (n_2) and third-order nonlinear susceptibility $\chi^{(3)}$, to create photonic devices with the best possible functions.[1,5-7] Nonlinear optical responses are commonly investigated by different methods like the Z-scan method [8-9] four-wave mixing [10-11] and spatial self-phase modulation (SSPM) [12-13] etc. The SSPM, also known as the optical Kerr effect, is a nonlinear optical phenomenon where nonlocal and intraband carriers of the material oscillate at an optical frequency of 10^{14} Hz, forming diffraction ring patterns through self-focusing.[4] SSPM is a simple and straightforward technique compared to other methods requiring complex experimental setup or data fitting. [12-13] This can create the diffraction ring pattern in the far field. [4, 12-13] SSPM diffraction ring pattern was first obtained in liquid crystals by Durbin et al. [14-15] and third-order nonlinear susceptibility was obtained by Wu et al. [16] by employing the SSPM method in exfoliated graphene. Following this, there was a significant increase in research attention towards investigating the nonlinear properties of 2D layered materials using the SSPM technique due to its ability to facilitate strong light-matter interaction, effective

bandgap modulation and superior optoelectronic properties.[1,17-19] It is essential to note that the SSPM diffraction ring pattern originates from the external electric field associated with the strong laser beam, which is explained by electron coherence theory.[4,20-22] Origin of SSPM diffraction ring pattern in 3D TaAs attributed to laser induced hole coherence.[23] We have made daily progress in observing SSPM experiments in various quantum materials, including different nanostructures such as nanowires, nanoparticles, colloidal nanocrystals and 2D flakes. Scientists have also obtained nonlinear parameters during these observations. [24-26] Wu et al. have demonstrated the first all-optical switching based on SSPM with two-colour intraband coherence in gapped quantum materials.[4] SSPM method has been successfully applied by various groups in diverse applications, such as energy conversion and photonic diodes. [27-31] There is a significant opportunity to discover SSPM effects in new quantum materials and utilize them in developing photonic devices for practical use.

Recently, low dimensional chalcogenides semiconducting materials, e.g., MoS_2, $MoSe_2$, InSe, TaSe, Bi_2Te_3, etc., are mostly investigated through the SSPM method due to their ultrathin nature and advantageous electronic and optoelectronic properties. [1, 27-31] The spatial self-phase modulation due to the intense laser beam, multiple diffraction ring patterns are formed at the far field for the liquid suspension of these semiconducting materials. The nonlinear refractive index and third-order nonlinear susceptibilities of these materials are determined by their strong electron coherence interaction with the laser intensities. Sb_2Se_3 is a promising semiconductor for optoelectronics or photonics due to its high absorption coefficient

(>10^5 cm^{-1}) in the visible region and decent carrier mobilities (μ_e~15 and μ_h ~42 $cm^2V^{-1}s^{-1}$). Also, it has a narrow band gap ranging from 1-1.2 eV. [32] Importantly, Sb_2Se_3 possesses a simple binary composition with a single and stable orthorhombic phase in which $[Sb_4Se_6]n$ nanoribbons are linked through van der Waals interaction along the x (100) and y (010) axes. In addition, the strong covalent bond along the z (001) axis causes Sb_2Se_3 nanostructures to grow intrinsically in a one-dimensional manner. However, owing to the dissimilar binding strength along the x, y and z axis (z>>x>y), Sb_2Se_3 possesses strong physical anisotropy and structure could be manipulated from bulk to either 1D or 2D by altering physical condition. [32-34] Concurrently, it possesses strong optical anisotropy and polarization sensitivity. Owing to the multifunctional properties, Sb_2Se_3 nanostructures offer enormous applications in a diverse area, e.g., photovoltaics, [35] photodetectors [36], photoelectrochemical (PEC) water splitting [37], thermoelectric [38] etc. The potential use of Sb_2Se_3's nonlinear optical properties in all-optical modulation technology has not been fully investigated.

Here, Sb_2Se_3 is identified as a promising candidate for investigating the nonlinear optical properties through the strong light-matter interaction, followed by a successful demonstration in all-optical device applications. SSPM experiments have performed with 1D Sb_2Se_3 nanorods to study their nonlinear optical properties and simultaneously implement them in all-optical device applications. After the interaction of the 671, 532 and 407 nm continuous laser beam through the Sb_2Se_3 nanorods suspension, concentric diffraction ring patterns are observed at the far field on the screen. With the help of the 'Wind-Chime' model, we explain the

formation and collapse process of the diffraction rings formed during this SSPM experiment. Additionally, SnS_2 nanosheets are utilized for their reverse saturable absorption properties in showcasing an optical diode alongside Sb_2Se_3.The laser beam undergoes propagational symmetry-breaking when combined with Sb_2Se_3 and SnS_2 (Sb_2Se_3/SnS_2 → forward and SnS_2/Sb_2Se_3 → reverse direction), resulting in non-reciprocal propagation of light and formation of an all-optical diode. An all-optical logic function, specifically an OR logic gate, has been successfully demonstrated using Sb_2Se_3 by manipulating the self-phase modulation (SPM) of two lasers with wavelengths of 671 nm and 532 nm.

5.2 Experimental Sections

5.2.1 Synthesis of Sb_2Se_3 nanorods

Sb_2Se_3 was synthesized by a typical solvothermal procedure. [33] First, 0.086 gm of $SbCl_3$ was dissolved in 75.8 ml DEG and then ammonia was added under magnetic stirring. Afterward, sodium sulphite (0.095 gm) and Se powder (0.048 gm) were mixed into the solution under continuous stirring. Then the as prepared mixture was transferred into a 100 ml teflon-lined stainless-steel autoclave and heated 22 hours at 180 ℃. After completing the process, it was cooled down normally and the products were filtered by vacuum filtration method. Then, the sample was consecutively washed with deionized water and absolute ethanol. Finally, the sample was dried in vacuum oven at 80 ℃ overnight for further use.

5.2.2. Synthesis of SnS_2 nanosheets

SnS_2 nanosheets were synthesized by previously reported procedure by Zhang et al. [39] In a typical procedure, $SnCl_4 \cdot 5H_2O$ (220 mg) and thioacetamide (280 mg) were added in 60 mL DI water and stirred unless mixed. After that, the solution was transferred into a 100 mL Teflon-lined autoclave for heating at 180 °C for 24 h. Then the autoclave was naturally cooled down to room temperature before collecting the yellow color samples by centrifugation process (10000 rpm). After collecting, the samples were dried in a hot air oven 80 °C for 6 h and stored carefully before further utilization.

5.2.3 Material Characterizations

Crystallinity of Sb_2Se_3 was obtained by X-ray diffraction at room temperature with Rigaku Ultima III X ray diffractometer using Cu Kα radiation having wavelength 1.54 A°. Raman spectroscopy (Witech) was employed to obtain the characteristic vibrational mode of Sb_2Se_3. Surface morphology was revealed by Field emission scanning electron microscopy (FESEM, Hitachi, S -4800) and high-resolution transmission electron microscopy (HRTEM, JEOLJEM 2100). TEM-EDX (Transmission electron microscopy-energy dispersive X ray spectroscopy) Elemental mapping shows the chemical composition and stoichiometric ratio of Sb_2Se_3. The bandgap was obtained by Kubelka-munk plot, from UV-Visible diffuse reflectance spectroscopy.

5.3. Results & Discussion

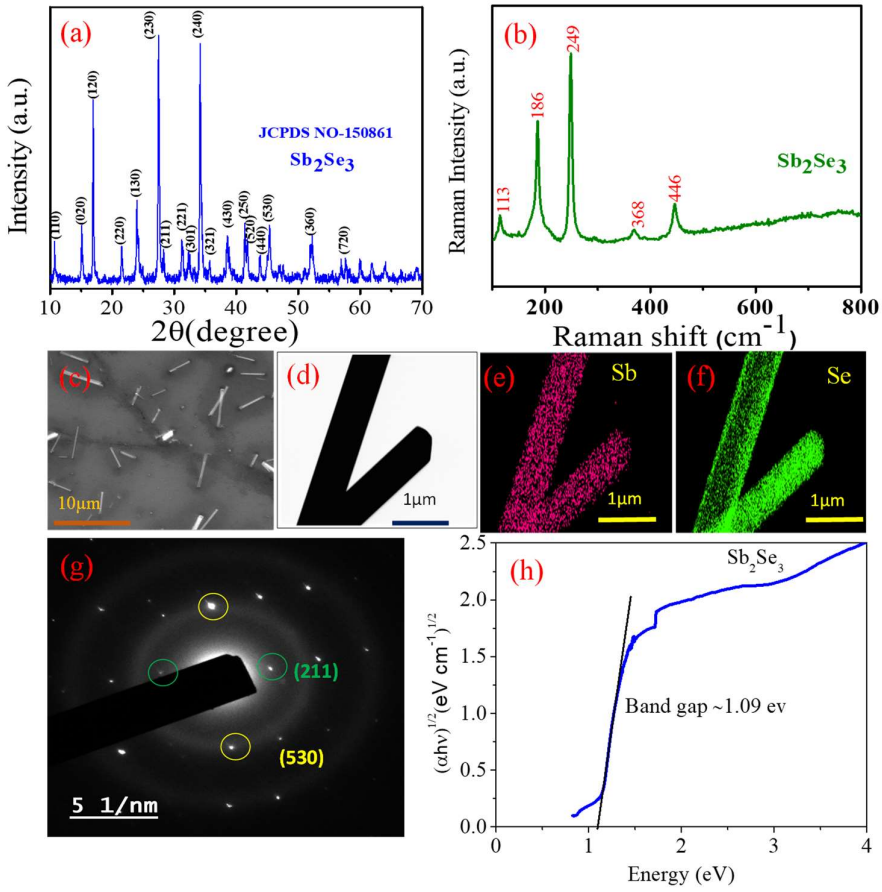

Figure 5.1: *Characterizations of Sb_2Se_3 NRs: (a) XRD pattern, (b) Raman spectra, (c) Scanning electron microscopy image, (d) Transmission electron microscopy image, (e-f) FETEM colour mapping of Sb and Se, (g) Selected area electron diffraction pattern and (h) Kubelka-Munk plot*

XRD patterns in figure 5.1(a) demonstrates highly polycrystalline Sb_2Se_3, corresponding to orthorhombic phase with space group *Pbnm (62)* (JCPDS card No.15-0861). Raman spectrum in figure 5.1(b) evinces prominent peaks at 115, 187, 251, 369 and 446 cm^{-1} which designate the formation of phase pure Sb_2Se_3. [33] The peak at 115 cm^{-1} is accompanying with the Se-Se bond vibration and the peak at 187

cm^{-1} is ascribed to the Sb-Se heteropolar stretching vibrational mode in the $Sb_2Se_{3/2}$ pyramids. [33] The Sb-Sb bond vibration in (Se_2Sb-$SbSe_2$) structural unit arises at 251 cm^{-1} whereas Sb-Se stretching vibrations are originated at 369 and 446 cm^{-1}. [33] The FESEM micrograph (Figure 5.1(c)) shows Sb_2Se_3 NRs with diameter < 1 μm and length < 10 μm. Again, surface morphology is probed by TEM (Figure 5.1(d)) which corroborate well with FESEM image. Further, FETEM micrographs in figure 5.1(e-f) suggest that Sb and Se elements are uniformly distributed throughout the nanorods. Figure 5.1(g) displays the selected area electron diffraction (SAED) pattern, verifying the (211) and (530) planes in agreement with the XRD pattern of the Sb_2Se_3 nanorods. Moreover, Sb_2Se_3 possesses indirect bandgap ~1.09 eV as obtained by Kubelka-munk plot in figure 5.1(h) which is therefore sensitive to electronic excitation of laser beams employed for our investigation.

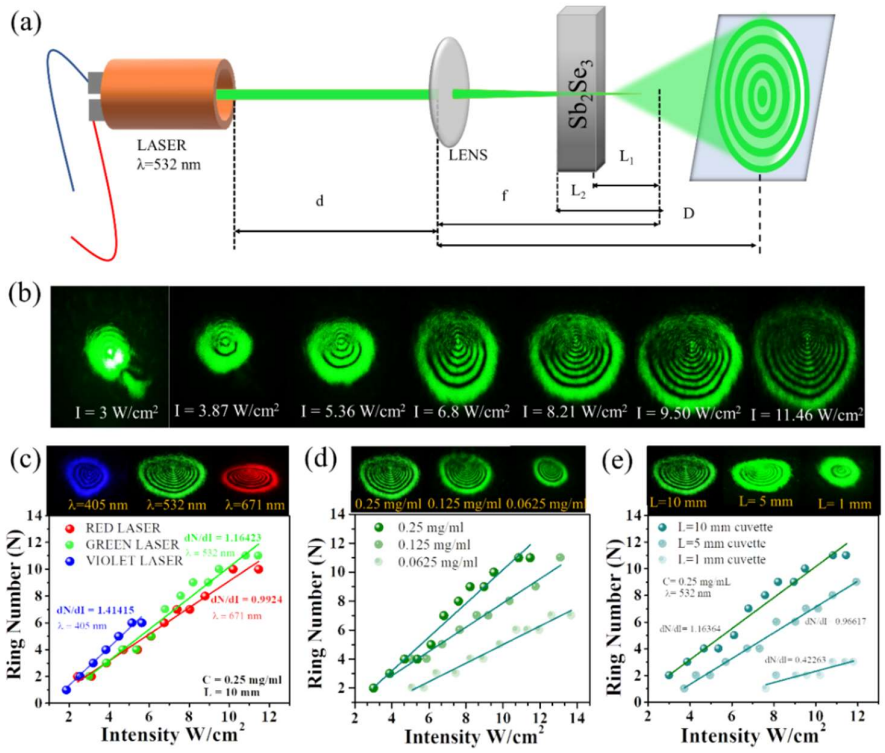

Figure 5.2: *Schematic of SSPM experiment at various condition: (a) Schematic diagram of experimental setup of Spatial Self-Phase Modulation (SSPM), (b) The real image of SSPM diffraction pattern of 532 nm laser beam (c) SSPM ring number variation with intensities at excitation of continuous laser beam of wavelength λ= 671, 532, 405 nm. (d) The diffraction ring number vs intensity of laser (λ =671 nm) with various concentrations of Sb_2Se_3 (0.25 mg/ml, 0.0625 mg/ml and 0.03125 mg/ml) (e) The variation of diffraction ring numbers with incident laser (λ = 671 nm) intensity with cuvette lengths of 1, 5 and 10 mm*

5.3.1 SSPM effect dominated by nonlinear Kerr effect: nonlinear refractive index

Figure 5.2(a) displays a brief schematic of our experimental setup, where a coherent and continuous laser with different wavelengths (405, 532 and 671 nm) has been

focused onto the suspended solution of Sb_2Se_3 by a lens with a focal length of 200 mm. Focused laser light illuminates the suspended Sb_2Se_3 inside the quartz cuvette, and the strong nonlinearity of the material induces the self-focusing effect and forms a concentric diffraction ring at the far field. These diffraction rings appear due to the optical Kerr effect, where a phase shift of the coherent laser beam has been observed during the propagation through the Sb_2Se_3 suspension. Due to the thermal effect, these concentric diffraction rings are distorted and vertically collapsed and became stable after some time. A digital camera has been placed behind the white screen to capture this continuous variation of this diffraction rings formation, collapse and steady state. According to the optical Kerr effect, the refractive index (n) of the materials has a strong dependence on the intensity (I) of the incident laser light and the relation between them has been presented as $n = n_0 + n_2 I$; where n_0 and n_2 are the linear and nonlinear refractive index of the material, respectively. [40] The phase shift ($\Delta\psi(r)$) of the incident gaussian laser beam ($\psi(r)$) has strong dependence upon the n_2 of the material in the SSPM experiment, and it can be expressed by, [41]

$$\Delta\psi(r) = \frac{2\pi}{\lambda} \int_0^{L_{eff}} n_2 \, I(r,z) dz \qquad (1)$$

Where, $r \in [0, \infty)$ is the radial co-ordinate, λ is the wavelength of the incident laser beam and L_{eff} is the effective propagation path passing through the Sb_2Se_3 dispersion. For a Gaussian light beam, the central light intensity (I (0, z)) is twice the value of average light intensity(I). This phase modulation of the output beam is proportional to the incident intensity (I(r,z)) of the laser beam. The diffraction ring number (N) can be expressed as. [16]

$$\Delta\psi(r_1) - \Delta\psi(r_2) = 2M\pi \quad (2)$$

Where M is the integer number, and odd or even value of M corresponds to the dark or bright diffraction pattern, respectively. From the following equation L_{eff} of the laser beam can be determined, [42-43]

$$L_{eff} = \int_{L_1}^{L_2}(1 + \frac{z^2}{z_0^2})^{-1}dz = z_0\, tan^{-1}\left[\frac{z}{z_0}\right]_{L_1}^{L_2} \quad (3)$$

where, $z_0 = \pi\omega_0^2/\lambda$; L_1, L_2 are the distance from the focus (f) to the side of the quartz cuvette; z_0 is the diffraction length, $\omega_0 = 1/e^2$ beam radius. Therefore, the nonlinear refractive index of Sb_2Se_3 can be determined from the formula, [31]

$$n_2 = \frac{\lambda}{2n_0L_{eff}}\frac{dN}{dI} \quad (4)$$

subsequently, the third order nonlinear susceptibility $\chi^{(3)}_{total}$ of Sb_2Se_3 can be determined as, [29,31]

$$\chi^{(3)}_{total} = \frac{cn_0^2}{12^{\ 2}}10^{-7}n_2 \text{ (esu)} \quad (5)$$

Where c is the velocity of light in free space. As, Sb_2Se_3 is a layered material, nonlinear susceptibility of a single layer has a significant role and can be determined by [29,31]

$$\chi^{(3)}_{total} = \chi^{(3)}_{singlelayer} \times N_{eff}^2 \quad (6)$$

Here N_{eff} is the effective number of charge carrier layers present in the material and calculation of effective number of charge carrier layers are in the following.

5.3.2. Calculation of N_{eff}

The number of effective layers is estimated in the following based on the calculation of [23]

Total number of molecules in solution of cuvette of volume V, is $N_{tot} = \rho * V * N_A$

Where, ρ = concentration of the solution in mol/L,

V = volume of the cuvette in L, N_A= Avogadro's number ($6.023*10^{23}$)

There are four effective number of molecules per unit cell of Sb_2Se_3 so,

Total number of unit cell of Sb_2Se_3 in solution of cuvette of volume V, is

$N_{unit} = N_{tot} / 4$.

Thus, a single effective layer contains, m = S/(a*c) unit cell.

Where, S = area of the plane of the cuvette which is perpendicular to the direction of light propagation in cm^2. (a = 11.63 A°, b = 3.97 A°, c = 11.78 A°, are the lattice constant of Sb_2Se_3). Then the layer number is $N_{cell} = N_{unit}/m$. The number of charge carrier layers that the incident laser beam encounter is $N_{eff} = 2* N_{cell}$. (there are two effective charge carrier layers per unit cell).

Figure 5.2(b) shows the variation of the diffraction ring numbers as a function of the intensity of the incident laser beam (532 nm). Each picture presented is taken after sufficient time of laser incident on the sample, and the corresponding images present their steady condition. The results show that the number of rings and their diameter

increases with the increase of the laser beam intensity, which arises due to the strong nonlinear response of Sb_2Se_3. To quantify this nonlinear response, the experimental results for all wavelengths (405, 532 and 671 nm) are also presented in figure 5.2(c). The solid points represent our experimental data, and the straight line is fitted linearly based on the experimental data, and the corresponding slopes (dN/dI) are 0.9924, 1.1642, 1.4142 for wavelength λ= 671, 532, 405 nm, respectively. Figure 5.2(c) 's upper panel displays the respective diffraction images at the highest intensity for all three incident laser lights. The nonlinear refractive index ($n_2=7.12*10^{-6}$ cm^2/W) and third-order nonlinear susceptibility ($\chi^{(3)}$ =0.00343 esu) have been determined using the equation (4) -(5) for λ= 532 nm. The n_2 and $\chi^{(3)}$ for other wavelengths are also calculated and presented in table 5.1.

Table 5.1. Representing nonlinear refractive index and third order nonlinear susceptibility of Sb_2Se_3 under different experimental conditions.

Experimental condition	λ (nm)	L (mm)	C (mg/ml)	$\frac{dN}{dI}$ (cm^2/W)	n_2 (in 10^{-6} cm^2/W)	$\chi^{(3)}_{total}$ [esu]	$\chi^{(3)}_{singlelayer}$ [in 10^{-9} esu]
Wavelength variation	671	10	0.25	0.9924	6.67	0.00423	1.05
	532	10	0.25	1.16423	7.12	0.00343	0.85
	405	10	0.25	1.41415	9.12	0.00228	0.57
Concentration variation	532	10	0.2500	1.16423	7.12	0.00343	0.85
	532	10	0.1250	0.8372	7.05	0.00179	1.55
	532	10	0.0625	0.641	5.39	0.00137	4.73
Cuvette thickness variation	532	10	0.25	1.16423	7.12	0.00343	0.85
	532	5	0.25	0.96617	16.2	0.00414	3.58
	532	1	0.25	0.42263	35.6	0.00907	198

Therefore, it is evidenced that the slope increases as the wavelength decreases, conclusively showing that higher photon energy produces higher SSPM effects which corroborate well with previous investigations of different semiconducting materials, and a comparison has been presented in the table 5.2. [1, 27]

Table 5.2. Third order optical susceptibilities of reported materials.

Materials	Dimensions	Solvent	Concentrations	Laser parameters	$X^{(3)}_{monolayer}$	References
$MoSe_2$	2D	NMP	$7.1*10^{-4}$ mol/L	532 nm CW Laser	10^{-9} esu	[44]
MoS_2	2D	Acetone	0.14 g/L	532 nm CW Laser,400 nm and 800 nm ultrafast lasers	10^{-9} esu	[4]
$MoTe_2$	2D	NMP	0.1 g/L	473 nm,532 nm, 750 nm and 801 nm CW Lasers	10^{-9} esu	[22]
Black phosphorus	2D	NMP	$4.03*10^{-3}$ mol/L	350- 1160 nm femtosecond Lasers	10^{-8} esu at multiple wavelengths.	[42]
Graphite	3D	NMP	0.075 mg/L	532 nm CW Laser	$2.2*10^{-9}$ esu	[20]
Graphene	2D	NMP	-	532 nm CW Laser	10^{-7} esu	[16]
$Ti_3C_2T_x$	2D	-	-	800 nm femtosecond Laser and 1064 nm picosecond Laser	10^{-15} esu at 800 nm and 10^{-7} esu at 1064 nm	[47]
TaAs	3D	NMP	0.2 g/L	532 nm laser	$9.9*10^{-9}$ esu	[23]
Te NTs	1D	-	0.25 mg/mL	532 nm laser	-	[48]
Te@ BiQDNTs	1D@0D	-	0.25 mg/mL	532nm laser	-	[48]
Sb_2Se_3	1D	NMP	0.25 mg/mL	671 nm laser	$1.05*10^{-9}$ esu	This Work

The diffraction patterns are formed due to the SSPM, which depends on the active material's concentration and the laser beam's effective path length. [31] To observe the above dependency, we further validate the SSPM experiments with different concentrations (C: 0.25, 0.125, 0.0625 mg/ml) of the active Sb_2Se_3 NRs suspension in a fixed cuvette length (L=10 mm) and also various cuvette thicknesses (L: 10, 5, 1 mm) with a fixed concentration of Sb_2Se_3 NRs (0.25 mg/ml). The experiment above was performed with the λ=532nm laser, and the corresponding results are presented in figure 5.2(d) and 5.2 (e), respectively. The corresponding stable diffraction patterns at maximum intensity are presented on the top panel of figure 5.2(d) & 5.2 (e). The calculated nonlinear refractive index (n_2) and third-order nonlinear susceptibility $\chi^{(3)}$, along with the concentration of active material and cuvette thickness variation, are enlisted in table 5.1. The results indicate that effective path length is vital during diffraction ring formation. As effective path length increases either by decreasing dispersion concentration or by increasing cuvette thickness, the slopes dN/dI also increase (see Table 5. 1), which necessarily alters the nonlinear properties of the active Sb_2Se_3 NRs dispersion. Again, N_{eff} also depends on the number of molecules present in the cuvette i.e concentration. Lesser concentration along with thinner cuvette width make layers number in cuvette less, and less N_{eff} make $\chi^{(3)}_{singlelayer}$higher, which are listed in table 5.1.

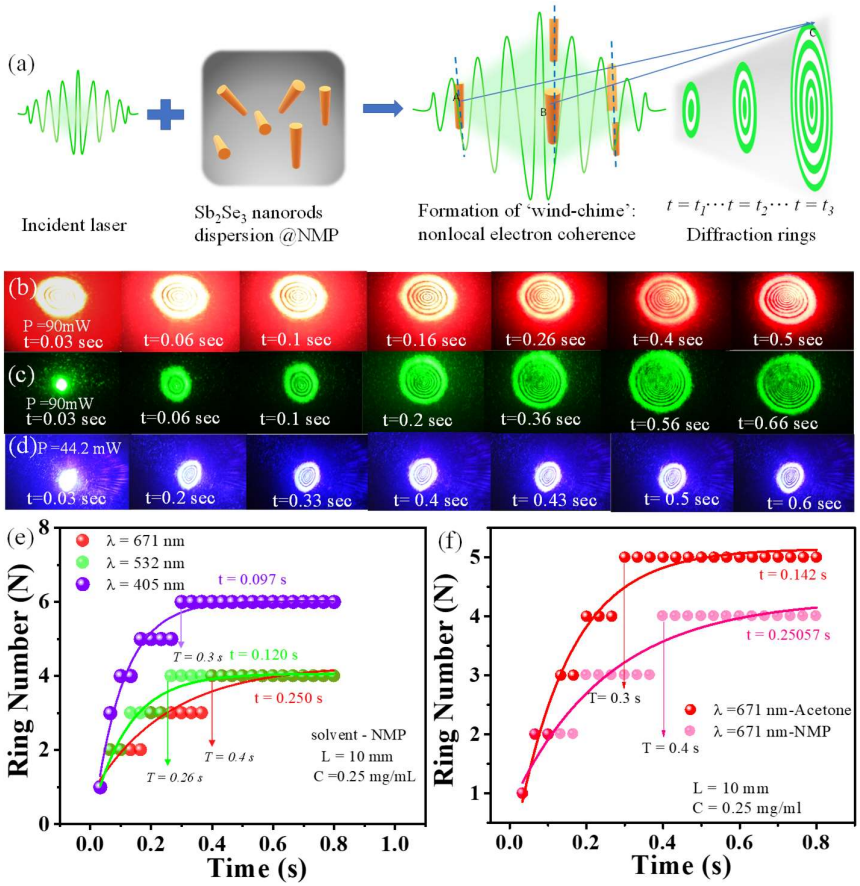

Figure 5.3: *Experimental verification of 'Wind-chime' model: (a). Schematic illustration of 'Wind-Chime model' showing the mechanism of light matter interaction and related diffraction pattern (b-d) Diffraction ring pattern appeared on the screen as a function of time for wavelength 671, 532 and 405 nm respectively. Time evolution of diffraction ring: (e) Diffraction ring numbers vs. time at intensity I = 5.36,5.36,5.62 W/cm² for wavelength 671,532 and 405 nm and (f) Effect of different viscous medium (NMP and acetone) for wavelength 671 nm*

5.3.3. Wind Chime Model

By manipulating laser light, Sb_2Se_3 NRs in a homogeneous NMP solution produce diffraction rings, whose origin is effectively explained by the 'Wind-Chime' model.[4] Wind-Chime' model is complete with the validation of electronic origin and ring formation time. When an optical electromagnetic wave (10^{14} Hz) interacts with atomic charged particles (electrons and holes), they undergo forced oscillations and respond by re-emitting the wave at the same frequency. Quasiparticles which are subjected to forced oscillation are coherent to incoming E.M. wave and they are mutually coherent with one another. The intensity of re-radiation depends on how freely the charged particles oscillate in response to the incoming wave. The primary limitation to these oscillations arises from the material's tendency for its electronic distribution to return to its preferred state. However, a balance exists between this restoring force and the extent to which the particles can be driven by the electromagnetic wave. This behaviour is quantitatively described by charged particles mobility. Sb_2Se_3 is a p-type material, and its $\chi^{(3)}_{singlelayer}$shows a strong correlation with its hole mobility (μ_h ~42 $cm^2V^{-1}s^{-1}$, μ_e ~15 $cm^2V^{-1}s^{-1}$) [29] as illustrated in figure 5.4. The data aligns well with an empirical relationship, highlighting the dominant role of hole coherence in generating the diffraction ring pattern.

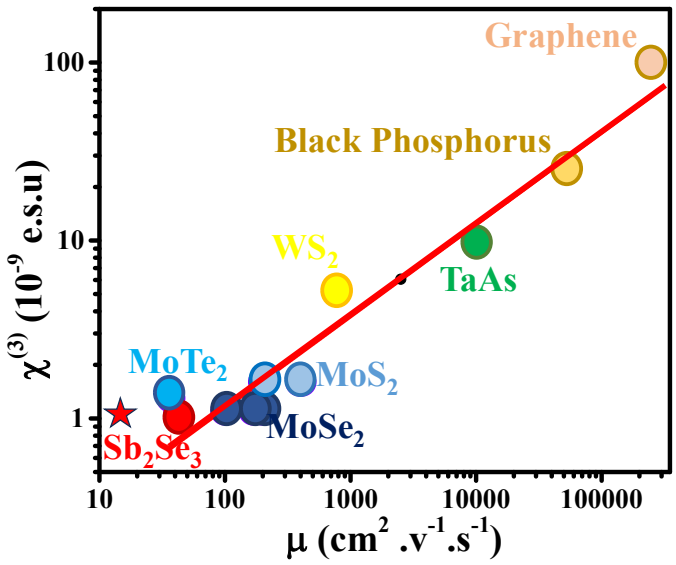

Figure 5.4. *Linear relation between* $\chi^{(3)}_{singlelayer}$ *and carrier mobility μ for 2D layered materials, 3D TaAs and* Sb_2Se_3 *Red star and red circle depict electron and hole mobility of* Sb_2Se_3 *respectively. All the values of* $\chi^{(3)}_{singlelayer}$ *except* Sb_2Se_3 *are adapted from ref [4],[22],[20],[47],[44]. All the values of μ are adapted from ref [49-59]*

As hole mobility is not much greater in Sb_2Se_3 than electron mobility, the electronic contribution in the origin of coherence is inevitable. In plane carrier mobilities are profoundly dominated in 2D materials. Sb_2Se_3 possesses anisotropic carrier mobility due to its van der Waals bond along x and y axis and covalent bond along z axis. However, for distinctive carrier mobilities along different direction it exhibits torque. Hence alignment of Sb_2Se_3 NRs takes some time to form ring pattern formation. The dielectric environment and refractive index are attributed to the time required for the ring formation. Figure 5.3(a) represents schematic illustration of 'Wind-Chime

model'. According to the 'Wind-Chime' model, the time required to attain the maximum diameter of the ring is the time required to fully align of all the Sb_2Se_3 NRs with the field direction. This phenomenon has been experimentally observed for all three laser sources (671, 532, 405 nm) and the snap-shots at different times during the dynamic of ring formations are presented in figure 5.3(b-d). The evolution time of ring formation follows the exponential model as below [4, 43]

$$N = A\left(1 - e^{-\frac{t}{t_c}}\right) \quad (7)$$

Where N is the number of rings, t_c is the rising time for the ring formation and A is a constant. Figure 5.3(e) shows the ring number vs. time graph which is fitted with the above function. The rising time of diffraction pattern for the λ= 671, 532 and 405 nm lights are estimated to be 0.25, 0.12 and 0.09 s respectively. Also, from the 'Wind-Chime' model, the time required for aligned most of the nanodomains inside the viscous medium has been presented as $T = \frac{\epsilon\pi\eta\xi RC}{1.72(\epsilon-1)Ih}$ where ϵ is the relative dielectric constant of Sb_2Se_3, η is the co-efficient of viscosity of the solvent, R is the Sb_2Se_3 domain radius, h is the thickness of Sb_2Se_3 and I is the laser intensity. The minimum time required to reach the highest number of rings for wavelengths 671, 532 and 405 nm has been experimentally determined to be T = 0.4, 0.26 and 0.3 s, respectively. Here, the intensities considered for the ring formation have been considered to be I= 5.36, 5.36 and 5.62 W/cm^2 for λ = 671, 532 and 405 nm, respectively. In addition, T also depends on the viscosity of the solvent and related experimental results are provided in figure 5.3(f). The value of τ in solvent NMP (η = 1.65*10^{-3} Pa s) and acetone (η = 3.2*10^{-4} Pa s) are 0.4 and 0.3 s respectively for

wavelength 671 nm. According to the 'Wind-Chime' model, time T is proportional to the viscosity of the solvent. Hence experimental results validate the 'Wind-Chime' model.

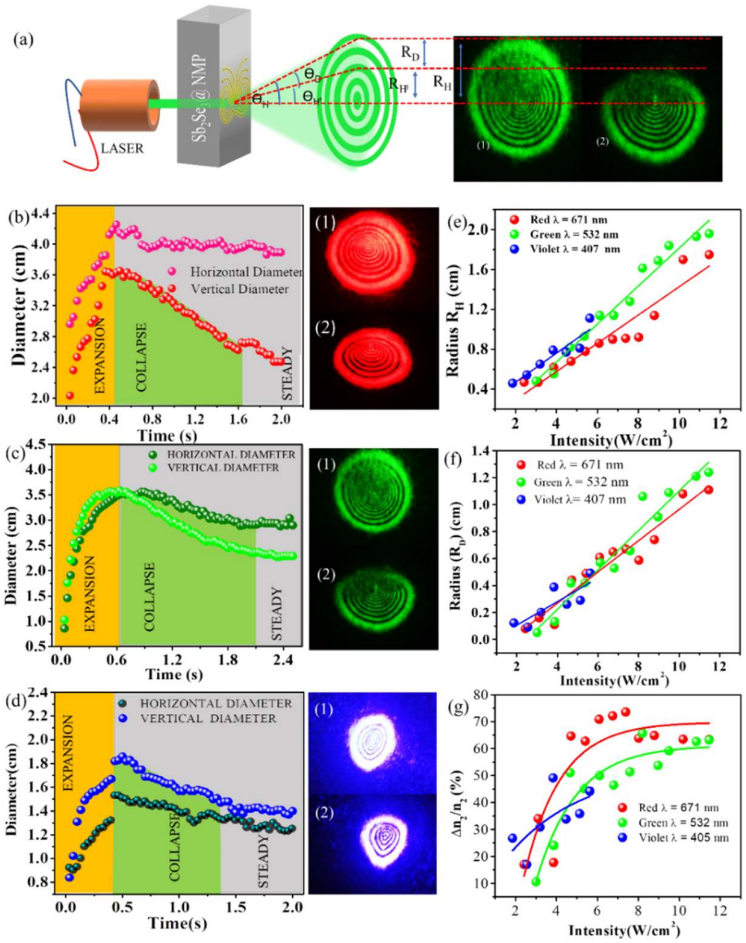

Figure 5.5*: Evolution of diffraction rings in SSPM: (a) Schematic illustration of collapse phenomenon. (b)-(d) Horizontal and vertical ring diameter evolution over time and their corresponding real SSPM patterns at maximum and distorted conditions for wavelength 671, 532, 405 nm respectively. (e) Maximum radius (R_H) versus incident laser intensity at maximum ring evolution condition and (f) Distorted radius (R_D) versus incident laser intensity at distorted ring condition for different laser beam wavelength 671, 532, 405 nm (g) Relative change in the nonlinear refractive index with incident laser light intensity for wavelength 671, 532 and 405 nm*

5.3.4. Dynamics of collapse phenomena of the SSPM diffracted laser beam

The diffraction patterns are spread to perfect concentric rings and reach their maximum condition through the 'Wind-Chime' alignment of the Sb_2Se_3 NRs with the laser's electric field. Due to the thermal effect, especially vertical thermal convection, a concentration gradient of Sb_2Se_3 has been established along the optical path. [40] Therefore, the vertical upper half of the diffraction patterns is distorted compared to the lower half. Figure 5.5(a) shows the schematic and experimental results of the distortion. This collapse process has due to thermal convection, and it must depend upon the energy of the photons and the intensity of the incident laser beam. Details study in formation and collapse process of diffraction ring is in figure 5.6.

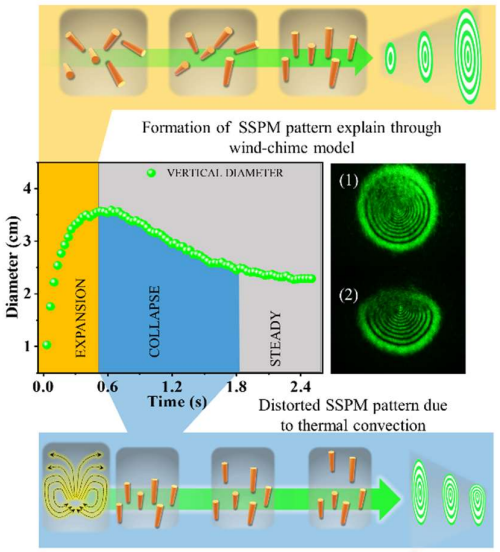

Figure 5.6. *Formation and distortion of SSPM pattern through wind-chime model and thermal convection respectively*

5.3.4.1 Formation of SSPM pattern

As the laser light passed through the sample, diffraction rings appeared and continued to increase in size. This was due to the reorientation of Sb_2Se_3 nanomaterials layers. The process occurred as follows: when the laser hit the material, electrons and holes were excited and moved in opposite directions, causing polarization of the layered nanomaterial. This polarization caused the layered structure to realign itself parallel to the electric field to minimize the system's energy. The time taken for the diffraction rings to form is equal to the time required for the layered nanomaterial to reorient itself. The formation time of the diffraction rings is dependent on several factors, including the size and permittivity of the material, the

viscosity of the solvent and the intensity of the incident laser light. This wind chime model provides a clear understanding of the formation process.

5.3.4.2 Distortion of SSPM pattern

Once the diffraction ring reaches its maximum diameter, the upper half of the ring becomes distorted due to thermal convection. As laser light passes through the solvent, it heats the liquid, creating a vertical thermal convection. This convection causes a decrease in the effective nonlinear refractive index n2 in the lower region, resulting in a lower number of polarized Sb_2Se_3 molecules in the lower part compared to the upper part. The distortion area of the SSPM pattern is opposite to the refractive index distribution. As a result, the upper part of the diffraction rings becomes distorted compared to the lower part.

we have measured the dynamic change of the vertical and horizontal diameters for all the lasers at their highest intensities. Figure 5.5 (b)-(d) presents the diameter's change during the expansion, collapse and stable condition for λ = 671, 532 and 405 nm, respectively. The side panel of the respective figures shows the maximum expansion and stable condition. From the above data, the collapse time is obtained as 1, 1.534 and 0.9s for 671 nm (I=11 W/cm^2), 532 nm (I=11 W/cm^2) and 405 nm (I=5.5 W/cm^2), respectively. Also, this dynamic collapse process can be quantified by the half cone angle (θ_H) of the diffraction pattern formed by the laser beam (Figure 5.5(a)) using the following expression, as [44]

$$\theta_H = n_2 I \left[-\frac{8rL}{\omega_0^2} exp\left(-\frac{2r^2}{\omega_0^2} \right) \right]_{max} \quad (8)$$

Where $\left[-\frac{8r}{\omega_0^2}exp\left(-\frac{2r^2}{\omega_0^2}\right)\right]$ is a constant =K and r $\in$ [0, ∞). So, θ_H is proportional to the nonlinear refractive index. During the collapse process, due to thermal convection, the concentration gradient of Sb_2Se_3 NRs changes between the upper and lower half of the optical path, which breaks the diffraction patterns' axial symmetry. As a result, the nonlinear refractive index has also been changed from n_2 to n_2'.

Therefore, the relative change in the nonlinear refractive index has been expressed by the collapsed angle θ_D as

$$\theta_D = (\theta_H - \theta_{H'}) = (n_2 - n_2')IK = \Delta n_2 IK \quad (9)$$

Using the above expressions, θ_D/θ_H can be expressed as the $\Delta n_2/n_2$.

Using simple trigonometry, the half angles are converted to the radius of the diffraction rings and the relative change in the nonlinear refractive index can be expressed as $\frac{\Delta n_2}{n_2} = \frac{\Delta\theta_D}{\theta_H} = \frac{R_D}{R_H} = \frac{R_H - R_{H'}}{R_H}$.[45-46] Figure 5.5(e-f) has been represented as the experimentally measured maximum vertical radius (R_H) before the collapse process and the radius after the collapse (R_D) as a function of the intensity of the incident laser for all the wavelengths. Moreover, figure 5.5(g) depicts the relative change in the nonlinear refractive index $\Delta n_2/n_2$ of Sb_2Se_3 NRs with the intensity of the incident laser, which has obtained to be 69% (for 11 W/cm^2) 60% (for 11 W/cm^2) and 42% (for 5.55 W/cm^2) for red, green and violet laser respectively.

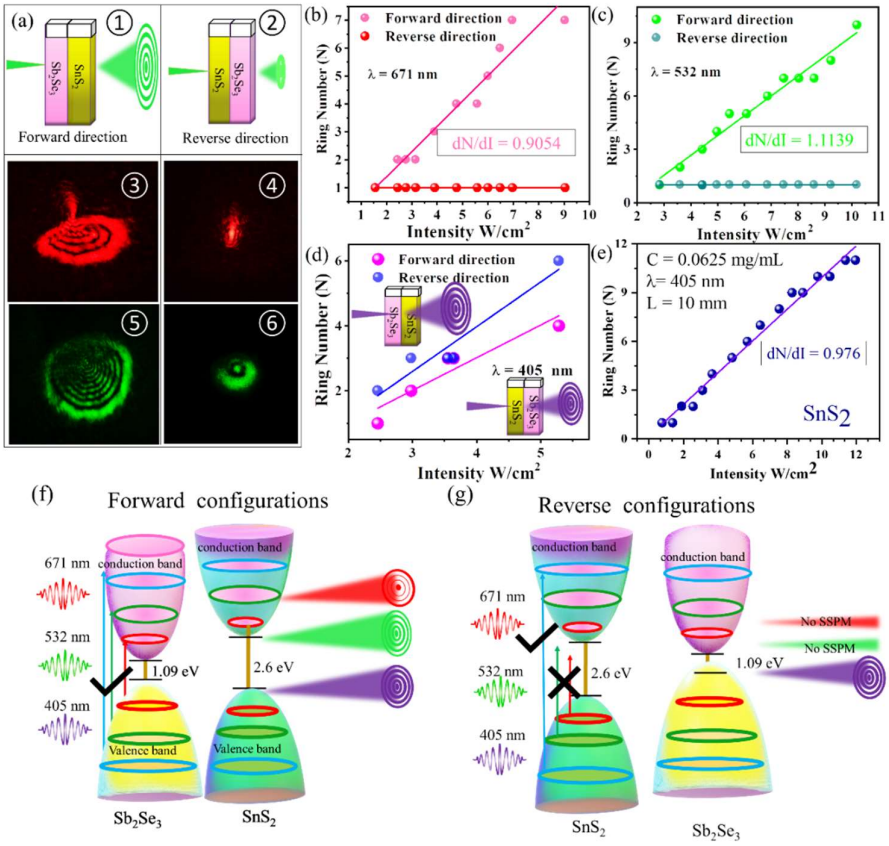

Figure 5.7: *All-optical diode application: (a) (1-2) Schematic presentation of nonreciprocal light propagation in forward and reverse direction [(3-4) Diffraction patterns obtained for 671 nm wavelength in forward and reverse condition respectively (5-6) Diffraction patterns obtained for 532 nm wavelength in forward and reverse condition respectively] The experimental results obtained for nonlinear photonic diode of hybrid structure Sb_2Se_3/SnS_2 for incident laser intensity of wavelength (b) 671nm and (c) 532 nm (d) Experimentally obtained intensity Vs. diffraction ring number for the photonic diode Sb_2Se_3/SnS_2 for wavelength 405 nm (e) intensity Vs. diffraction ring number for SnS_2 for wavelength 405 nm. Schematic presentation of band diagram model for (f)forward configuration of Sb_2Se_3/SnS_2 (g)reverse configuration of Sb_2Se_3/SnS_2*

5.3.5. Demonstration of all-optical diode (Sb_2Se_3↔SnS_2)

Sb_2Se_3 NRs possess a strong optical Kerr effect and show a high nonlinear refractive index and third-order nonlinear susceptibility as compared to other chalcogenide-based 2D materials. This nonlinear property has been used to construct Sb_2Se_3 NRs/ SnS_2 hybrid structure for an all-optical diode application. Initially, Sb_2Se_3 NRs and SnS_2 with the same concentration were dispersed in an NMP solution and put in two different cuvettes placed side-by-side to construct an all-optical diode. These two cuvettes are placed in front of the optical path of the coherent laser light. Laser light has been passed through two configurations. One is first through Sb_2Se_3, then SnS_2, and another configuration is first through SnS_2 and then Sb_2Se_3. Compared to the electronic diode structure, the first configuration is referred to as the forward configuration, while the latter is called the reversed configuration. Both configurations schematically have been presented in figure 5.7(a) ① and ②, respectively. As the name suggested, in forward configuration, the SSPM phenomena have been occurring and the diffraction rings are observed on the screen for the laser of wavelength 671 and 532 nm (Figure 5.7(a)③, ⑤). Similarly, no SSPM has happened in the reverse configuration and no diffraction rings are observed at the far field (Figure 5.7(a)④, ⑥). This all-optical diode for 671 and 532 nm is observed for the entire intensity range, and results are presented in figure 5.7(b) and 5.7(c), respectively. This diode response has not been observed for the 405 nm laser light. Both the forward and reverse configurations have shown the SSPM, and the diffraction ring variation with intensity is presented in figure 5.7(d). The above effect is attributed due to the reverse saturation absorption property of SnS_2. [31] The

bandgap of SnS_2 is 2.6 eV, which is larger than the forbidden bandgap range corresponding to the wavelength 671 and 532 nm. However, a 405 nm laser can create SSPM in SnS_2; the results are presented in figure 5.7(e). Hence, 671 and 532 nm laser does not create any interaction with the SnS_2, and as a result, in reverse configuration, all lights are absorbed by the SnS_2, and the remaining light does not have enough intensity to interact with Sb_2Se_3 to create SSPM. From the band diagram model, we present schematically both forward and reverse configurations in figure 5.7(f) and 5.7(g), respectively.

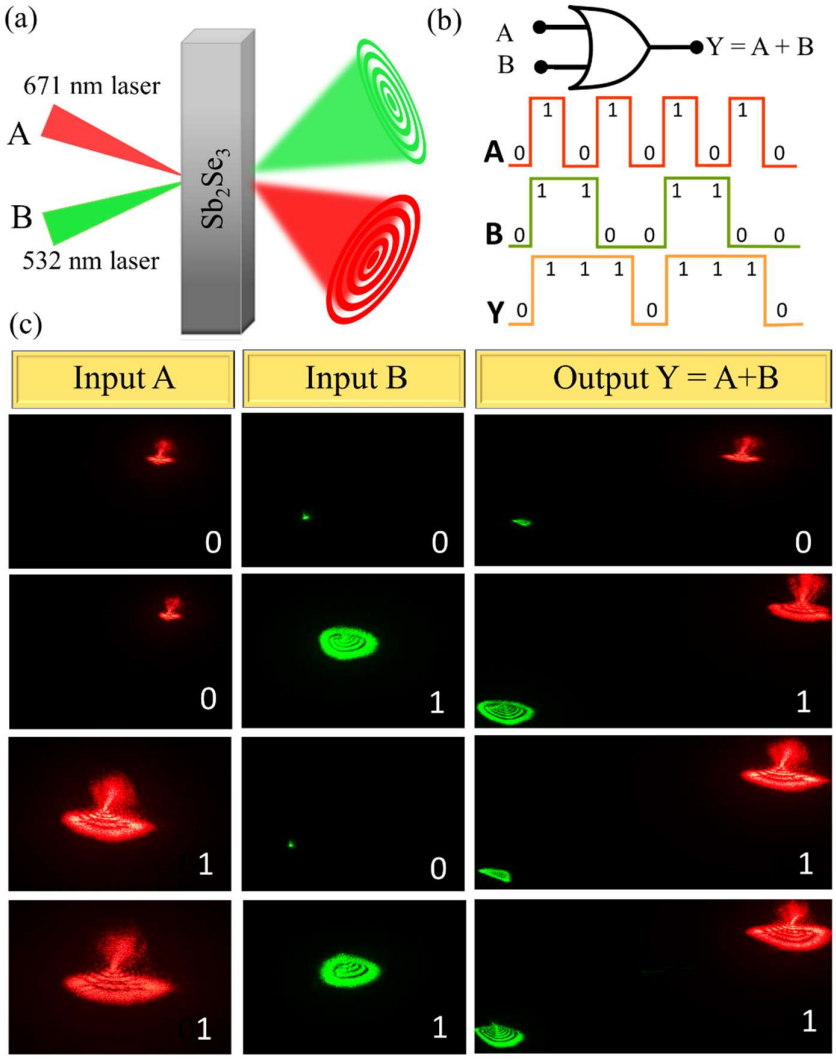

Figure5.8: *All-optical logic application: Realization of all-optical modulation by self-phase modulation and demonstration of OR logic function (a) Schematic of light-light modulation system, (b) Two input OR gate: input and output waveform of OR logical operation, (c) Experimental results of OR logical operation with 671 and 532 nm laser beam*

5.3.6. Sb_2Se_3 optical modulator /switcher- based on SSPM

Taking advantage of the strong optical Kerr effect, Sb_2Se_3 NRs can be used not only in all-optical diode but it can be used for all-optical logic function like OR gate using the self-phase modulation (SPM) technique. Here, a relatively strong laser light has been employed to modulate the propagation of another laser light with relatively weak intensity. The experimental setup for this light-light modulation technique has been schematically presented in figure 5.8(a). Here, the SPM technique has been employed between the 671 and 532 nm laser sources when they interact through the Sb_2Se_3 NRs. Low and high intensity of the lasers are considered to be as a "0" and "1" state in input, and the diffraction ring due to SPM (when both the laser shows diffraction rings) has to be considered to be "1", otherwise the output be "0". Figure 5.8(b) shows the symbolic and wavefront presentation of the OR logic gate. Two inputs, "A" and "B", are considered 671 and 532 nm laser, respectively. When both the laser is low intensity, they can't create any diffraction ring patterns on the screen, so for "0", "0" input, we get "0" output. Again, when both the lasers are at the highest intensities, they create diffraction rings on the screen. This state can be attributed as "1", "1" input, and we have got "1" as output. But interestingly, when any of one has low power and the others have high power, we also get the diffraction rings for both lasers in output. This happens due to the SPM of lights passing through the Sb_2Se_3 NRs. As a result, the output is "1" whenever anyone's input is "1". This function is typically an OR logic function. The experimental results are presented in a truth table format in figure 5.8(c). In summary, these two laser lights can achieve mutual modulation using the strong optical Kerr effect of Sb_2Se_3 NRs.

5.4. Conclusions

In summary, after the measurement and calculation, we found that the Sb_2Se_3 NRs could obtain a narrow bandgap material to excite strong nonlinear optical responses, especially high nonlinear refractive index (n_2) and third-order nonlinear susceptibility $\chi^{(3)}$, for the first time using the SSPM technique. Due to the strong light-matter interaction between the intense laser light (λ= 671, 532, 405 nm) and Sb_2Se_3 NRs, results in diffraction ring patterns in the far field. These nonlinear properties are strongly depending upon the wavelength of the laser, the concentration of NRs and the effective optical path lengths. The 'Wind-Chime' model was used to analyze the formation process of these diffraction rings, and the thermal convection through suspended NRs has explained the distortion of diffraction rings. By taking advantage of the strong optical Kerr effect and reverse saturation absorption properties of Sb_2Se_3 and SnS_2, we have demonstrated an all-optical diode for 671 and 532 nm laser sources. Furthermore, a novel, all-optical logic function, the OR logic gate, has been demonstrated by taking advantage of SPM, where a weak light can be modulated in the presence of a strong light due to the strong nonlinear response of Sb_2Se_3 NRs. Therefore, exploring the nonlinear optical properties of Sb_2Se_3 NRs and demonstrating all-optical diode and logic applications could pave the way for developing future devices utilizing all-optical signal processing.

References

1. L. Wu, X. Yuan, D. Ma, Y. Zhang, W. Huang, Y. Ge, Y. Song, Y. Xiang, J. Li, H. Zhang, *Small,* 2020, **16**, 2002252.
2. D. Pacifici, H. J. Lezec, H. A. Atwater, Nat. *Photonics,* 2007, **1**, 402.
3. M. Hochberg, T. Baehr-Jones, G. Wang, M. Shearn, K. Harvard, J. Luo, B. Chen, Z. Shi, R. Lawson, P. Sullivan, A. K. Y. Jen, L. Dalton, A. Scherer, *Nat. Mater.,* 2006, **5**, 703.
4. Y. L. Wu, Q. Wu, F. Sun, C. Cheng, S. Meng and Jimin Zhao, Proc. Natl. Acad. Sci. U. S. A., 2015, **112**, 11800.
5. E. Wong, K. L. Lee, T. B. Anderson, J. Lightwave Technol., 2007, **25**, 67.
6. Q. Bao, H. Zhang, Y. Wang, Z. Ni, Y. Yan, Z. X. Shen, K. P. Loh, D. Y. Tang, Adv. Funct. Mater., 2009, **19**, 3077.
7. Y. Wang, W. Huang, C. Wang, J. Guo, F. Zhang, Y. Song, Y. Ge, L. Wu, J. Liu, J. Li, H. Zhang, Laser Photonics Rev., 2019, **13**, 1800313.
8. Y. Xu, W. Wang, Y. Ge, H. Guo, X. Zhang, S. Chen, Y. Deng, Z. Lu, H. Zhang, Adv. Funct. Mater., 2017, **27**, 1702437.
9. Z. Guo, H. Zhang, S. Lu, Z. Wang, S. Tang, J. Shao, Z. Sun, H. Xie, H. Wang, X.-F. Yu, P. K. Chu, Adv. Funct. Mater., 2015, **25**, 6996.
10. S. A. March, D. B. Riley, C. Clegg, D. Webber, X. Liu, M. Dobrowolska, J. K. Furdyna, I. G. Hill, K. C. Hall, ACS Photonics, 2017, **4**, 1515.
11. S. K. Turitsyn, A. E. Bednyakova, M. P. Fedoruk, S. B. Papernyi, W. R. L. Clements, Nat. Photonics, 2015, **9**, 608.

12. L. Lu, Z. Liang, L. Wu, Y. Chen, Y. Song, S. C. Dhanabalan, J. S. Ponraj, B. Dong, Y. Xiang, F. Xing, D. Fan, H. Zhang, Laser Photonics Rev., 2018, **12**, 1700221.
13. L. Lu, X. Tang, R. Cao, L. Wu, Z. Li, G. Jing, B. Dong, S. Lu, Y. Li, Y. Xiang, J. Li, D. Fan, H. Zhang, Adv. Opt. Mater., 2017, **5**, 1700301.
14. S. D. Durbin, S. M. Arakelian, Y. R. Shen, Opt. Lett., 1981, **6**, 411.
15. S. D. Durbin, S. M. Arakelian, and Y. R. Shen, Phys. Rev. Lett., 1981, **47**,1411.
16. R. Wu, Y. Zhang, S. Yan, F. Bian, W. Wang, X. Bai, X. Lu, J. Zhao, and E. Wang, Nano Lett., 2011, **11**, 5159.
17. S. Yu, X. Wu, Y. Wang, X. Guo, and L. Tong, Adv. Mater., 2017, **29**, 1606128.
18. Y. Gao, Y. Hu, C. Ling, G. Rui, J. He and B. Gu, *Nanoscale*, 2023, **15**, 6225.
19. J. E. Q. Bautista, C. L. A. V. Campos, M. L. da Silva-Neto, Cid B. de Araujo,́ Ali M. Jawaid, R. Busch, R. A. Vaia, and A. S. L. Gomes, ACS Photonics, 2023, **10**, 484.
20. Y.L. Wu, L.L. Zhu, Q. Wu, F. Sun, J.K. Wei, Y.C. Tian, W.L. Wang, X.D. Bai, X. Zuo, J. Zhao, *Appl. Phys. Lett.*,2016, **24**, 108.
21. W. Wang, Y. Wu, Q. Wu, J. Hua, J. Zhao, Sci. Rep., 2016 ,**6(1),**22072.
22. L. Hu, F. Sun, H. Zhao, J. Zhao, *Opt. Lett.*, 2019, ***44*(21)**, 5214-5217.
23. Y. Huang, H. Zhao, Z. Li, L. Hu, Y. Wu, F. Sun, S. Meng, J. Zhao, *Adv.Mater.*,2023 ***35*(11)**, 2208362.

24. C. Wang, S. Xiao, X. Xiao, H. Zhu, L. Zhou, Y. Wang, X. Du, Y. Wang, Z. Yang, R. Duan, M. Zhong, H. Rubahn, G. Zhang, Y. Li, and J. He, *J. Phys. Chem. C.,* 2021, 125, **28**, 15441.

25. R. Zamiri, A. Zakaria, M. B. Ahmad, A. R. Sadrolhosseini, K. Shameli, M. Darroudi, M. A. Mahdi, Optik, 2011, **122**, 836.

26. X. Wang, Y. Yan, H. Cheng, Y. Wang, J. Han, Mater. Lett., 2018, **214**, 247.

27. Y. Liao, C. Song, Y. Xiang, and X. Dai, Ann. Phys. (Berlin) ,2020, **532**, 2000322.

28. Y. Liao, Y. Shan, L.Wu, Y. Xiang, and X. Dai, Adv. Optical Mater., 2020, **8**, 1901862.

29. Y. Shan, L. Wu, Y. Liao, J. Tang, X. Dai and Y. Xiang, J. Mater. Chem. C, 2019, **7**, 3811.

30. Y. Jia, Y. Liao, L. Wu, Y. Shan, X. Dai, H. Cai, Y. Xiang and D. Fan, Nanoscale, 2019, **11**, 4515.

31. K. Sk, B. Das, N. Chakraborty, M. Samanta, S.Bera, A. Bera, D. S.Roy, S. K. Pradhan, K. K. Chattopadhyay, and M. Mondal, Adv. Optical Mater., 2022, **10**, 2200791.

32. K. Zeng, D. J. Xue and J. Tang, Semicond. Sci. Technol., 2016, **31**, 063001.

33. N. Sen, A. Das, S. Maity, S. Ghosh, M. Samanta, and K. K. Chattopadhyay, ACS Appl. Energy Mater., 2023, **6**, 58.

34. H. Song, T. Li, J. Zhang, Y. Zhou, J. Luo, C. Chen, B. Yang, C. Ge, Y. Wu, J. Tang, Adv. Mater., 2017, **29**, 1700441.

35. A. Mavlonov, T. Razykov, F. Raziq, J. Gana, J. Chantana, Y. Kawano, T. Nishimura, H. Weie, A. Zakutayev, T. Minemoto, X. Zua, S. Li, L. Qiao, Solar Energy, 2020, **201**, 227.

36. T. Zhai, M. Ye, L. Li, X. Fang, M. Liao, Y. Li, Y. Koide, Y. Bando, D. Golberg, Adv. Mater., 2010, **22**, 4530.

37. S. Chen, T. Liu, Z. Zheng, M. Ishaq, G. Liang, P. Fan, T. Chen, J. Tang, J. Energy Chem., 2022, **67**, 508.

38. T. Y. Ko, M. Shellaiah, K. W. Sun, *Sci. Rep,* 2016, **6**, 35086.

39. J. Zhang, G. Huang, J. Zeng, Y. Shi, S. Lin, X. Chen, H. Wang, Z. Kong, J. Xi, Z. Ji, J. Am. Ceram. Soc., 2019, **102**, 2810.

40. G. Wang, S. Zhang, F. A. Umran, X.Cheng, N. Dong, D. Coghlan, Y. Cheng, L. Zhang, W. J. Blau, and J. Wang, Appl. Phys. Lett., 2014, **104**, 141909.

41. Y. Jia, Y. Shan, L. Wu, X. Dai, D. Fan, Y. Xiang, Photonics Res., 2018, **6**, 1040.

42. J. Zhang, X. Yu, W. Han, B. Lv, X. Li, S. Xiao, Y. Gao, J. He, Opt. Lett., 2016, **41**, 1704.

43. S. Xiao, Y.-l. He, Y.-l. Dong, Y.-d. Wang, L. Zhou, X.-j. Zhang, Y.-w. Wang, J. He, Front. Phys., 2021, **9**, 212.

44. G. Wang, S. Zhang, X. Zhang, L. Zhang, Y. Cheng, D. Fox, H. Zhang, J. N. Coleman, W. J. Blau, J. Wang, Photonics Res., 2015, **3**, A51.

45. L. Wu, Z. Xie, L. Lu, J. Zhao, Y. Wang, X. Jiang, Y. Ge, F. Zhang, S. Lu, Z. Guo, J. Liu, Y. Xiang, S. Xu, J. Li, D. Fan, H. Zhang, Adv. Opt. Mater., 2018, **6**, 1700985.

46. M. Zidan, M. El-Daher, M. Al-Ktaifani, A. Allahham, A. Ghanem, Optik ,2020, **219**, 165275.

47. J. Li, Z. Zhang, J. Yi, L. Miao, J. Huang, J. Zhang, Y. He, B. Huang, C. Zhao, Y. Zao, S. Wen, Nanophotonics, 2020, **9(8)** 2415-2424.

48. L. Wu, Z. Ye, Y. Xixi, Z. Feng, H. Weichun, M. Dingtao, Z. Jinlai, et al. Appl. Mater. Today, 2020, **19** 100589.

49. L. Cheng, L. Yuanyue, *J. Am. Chem. Soc., 2018,* **140(51)**,17895-17900.

50. S. V. Morozov, K. S. Novoselov, M. I. Katsnelson, F. Schedin, D. C. Elias, J. A. Jaszczak, A. K. Geim, Phys. Rev. Lett., 2008, **100**, 016602.

51. M. Orlita, C. Faugeras, P. Plochocka, P. Neugebauer, G. Martinez, D. K. Maude, A-L. Barra et al. Phys. Rev. Lett., 2008, **101**, 267601.

52. SL. Li, K. Tsukagoshi, E. Orgiu, P. Samorì., Chem. Soc. Rev., 2016, **45**,118-151.

53. S. Das, H-Y. Chen, A. V. Penumatcha, J. Appenzeller., *Nano Lett., 2013,* **13**, 100-105.

54. M. M. Perera, M-W. Lin, H-J. Chuang, B. P. Chamlagain, C. Wang, X. Tan, M. M-C. Cheng, D. Tománek, Z. Zhou., *ACS Nano*, 2013, **7**, 4449-4458.

55. N.R. Pradhan, D. Rhodes, Y. Xin, S. Memaran, L. Bhaskaran, M. Siddiq, S. Hill, P. M. Ajayan, L. Balicas, *ACS Nano, 2014,* **8**, 7923-7929.

56. N.R. Pradhan, D. Rhodes, S. Feng, Y. Xin, S. Memaran, B-H. Moon, H. Terrones, M. Terrones, L. Balicas. *ACS Nano, 2014,* **8**, 5911-5920.

57. I.G. Lezama, A. Ubaldini, M. Longobardi, E. Giannini, C. Renner, A. B. Kuzmenko, A. F. Morpurgo, 2D Mater., *2014,* **1**, 021002.

58. G.Long, D. Maryenko, J. Shen, S. Xu, J. Hou, Z. Wu, W. K. Wong et al.,Nano Lett., 2016, 16,7768-7773.

59. K. Zeng, D.-J. Xue, J. Tang, Semicond. Sci. *Technol.*, 2016, **31**, 063001.

Chapter 6

Efficient light to heat conversion in Sb_2Se_3 nanorods and the role of macro-channel imprinted Sb_2Se_3 loaded hybrid membrane for superior desalination performance

The study demonstrates promising light-to-heat conversion efficiencies of Sb_2Se_3 for red (671 nm) and green (532 nm) lasers, through customized water droplet experiments. Hybrid PVDF(M)/Sb_2Se_3 NRs membranes were developed for solar desalination, with heat generation driven by electron/hole-acoustic phonon scattering. However, the hydrophobic Sb_2Se_3 NRs layer limits water diffusion to hot zones, reducing solar evaporation efficiency. To address this, a novel strategy of mechanically imprinting macro-channels in the membranes was introduced, enhancing water transport to hot zones and offering a solution for hydrophobic materials in desalination applications. This chapter has been published in the journal *Small*

Sen. Nabanita et al. *Small, 2024* e2408293.

6.1. Introduction

The facile utilization of solar energy has effectively addressed the scarcity of potable water on earth, highlighting the interconnected role of two natural resources. [1-2] The implementation of solar energy in steam and clean water generation from seawater or contaminated water is recognized as a promising, green and sustainable processes in the era of water scarcity. [3-5] However, common solar to vapor generation yields only 30 to 45% photothermal conversion efficiency, a consequence of inadequate solar light absorption and significant heat losses in bulk water. [6-7] This drawback impedes practical applications. A team of scientist has devised an enhanced light absorption system known as a volumetric heating module, achieved through the dispersion of light absorbing nanoparticles in bulk water. [8-10] While this volumetric heating system enhances light absorption, the substantial heat loss persists owing to the coexisting bulk water. [11-14] Subsequently, an interfacial solar evaporation system has emerged. It consists of a bulk water reservoir in the bottom, followed by a polystyrene foam, a hydrophilic substrate and light absorbing materials on the top. [11-14] The hydrophilic substrate receives water through capillary force. The incident solar light generates heat on the top absorbing materials. As a results, water molecules which diffuse in the surface evaporates easily. [11-14] Additionally, the inclusion of polystyrene foam serves to mitigate bulk heat loss. [11,12]

The accomplishment of efficient freshwater production through interfacial solar evaporation system stands as a notable success. Identification of potential photothermal materials and engineering are crucial for development of this system. [15-22] Within the pool of materials science, photothermal materials exhibit notable efficiency in effectively harnessing the entire solar spectrum. Their capacity for converting light into heat demonstrates a high efficiency. Diverge categories of materials, including carbonaceous materials, plasmonic nanoparticles, semiconductors and polymers delineate the landscape of solar absorber materials. [20,23-35] These materials generate heat through distinct mechanisms: thermal vibration of molecules, plasmonic localized heating and electron- hole generation and relaxation respectively. [20,23-26,1,2,14,27-30] In addition to these methods, diverse microscopic and macroscopic structural configurations are utilized to attain heat localization on the evaporative surface for faster evaporation process.[1] The incorporation of distinct one-dimensional (1D), two-dimensional (2D), and three-dimensional (3D) pathways for water molecules allows for precise control over the supply of optimized water which minimizes heat loss and improves water evaporation rates. [36,37] The conventional theory emphasizes that only hydrophilic solar absorbers are suitable for solar water evaporation. [38] Recently, a combination of a top hydrophobic absorber along with a hydrophilic substrate beneath the former yields 94% efficiency under 5 kW m^{-2} solar irradiation. [39] Hence, both the utilization of photothermal materials and the precise adjustment of the dimensions of water path channels are equally crucial for enhancing solar water evaporation.

Recently, Sb_2Se_3 has been identified as potential low dimensional materials owing to its structural diversity and fascinating electronic and optoelectronic properties.[40] It is an indirect band gap semiconductor with band gap ranging from 1.0 to 1.2 eV, effectively covering the solar spectrum up to 1200 nm. Moreover, it exhibits a high absorption coefficient of 10^5 cm^{-1} at shorter wavelengths. [41,42] The application of Sb_2Se_3 is not only limited in photovoltaic, photoelectrochemical devices also in electrocatalysis, photodetector, nonlinear photonic devices etc. [43] Importantly, due to nonradiative nature of Sb_2Se_3 it generates phonon and it possess low thermal conductivity k ~ 0.36–1.9 W m^{-1} $\cdot K^{-1}$. [41,42] These properties are ideal for photothermal heat generation and localization. There are very few literatures available which explore full potential of Sb_2Se_3 as photothermal applications. Likely, Chen et. al., reported UV-vis photothermal response of Sb_2Se_3 nanowires in differential calorimetric approach. [44] Zhou et. al., demonstrated Sb_2Se_3 nanosheets in photonic cancer theranostics utilizing 808 nm laser. [45] However, full potential of Sb_2Se_3 is yet to be unlocked. Subsequently, we propose Sb_2Se_3 as a top solar absorbing hydrophobic material combined with hydrophilic PVDF membrane positioned underneath to obtain substantial solar water evaporation. Initially, we assess the light-to-heat conversion efficiency by carefully designing a laser heating experiment utilizing Sb_2Se_3 NRs suspended in water droplets. The outcomes reveal notable light-to-heat conversion efficiencies, reaching ~ 57.8% and 58% for lasers with wavelengths of 671 and 532 nm, respectively. These findings underscore the superior photothermal properties of Sb_2Se_3. After integration in desalination device, we found intrinsic hydrophobic surface limits the faster water evaporation owing to

the delay of supply to the hot zones. Consequently, it restricts higher mass evaporation rate. So, creatively we imprint macro-channel on top Sb_2Se_3 layer for easy water transport through the channel region. Subsequently, the hybrid membrane with channel shows higher mass evaporation rate, attaining 2.37 kg m^{-2} h^{-1} with an efficiency of 148% under mercury vapor lamp of 1000 W m^{-2} intensity. Moreover, we extend the desalination performance in outdoor sunlight and a commendable efficiency of 112% is found under an average irradiance of 950 W m^{-2}. Elevating the mass of Sb_2Se_3 as an absorber leads to a heightened evaporation rate, particularly in conditions characterized by a high degree of salinity. The substantial sustainability demonstrated across various pH levels establishes Sb_2Se_3 as a promising material in the realm of light-to-heat conversion.

6.2. Materials and methods

6.2.1. Synthesis of Sb_2Se_3

Sb_2Se_3 was synthesized through a conventional solvothermal synthesis approach, described in our earlier work. [46] Initially, 0.086 gm of $SbCl_3$ was dissolved in 75.8 ml of diethylene glycol (DEG), followed by the addition of ammonia with continuous magnetic stirring. Subsequently, a mixture of sodium sulfite (0.095 gm) and Se powder (0.048 gm) was introduced into the solution under constant stirring. The resulting mixture was then transferred into a 100 ml teflon-lined stainless-steel autoclave and subjected to 22 hours of heating at 180 ℃. Upon completion of the reaction, the system was allowed to cool, and the resulting products were separated using vacuum filtration. The obtained sample was subsequently washed with

deionized water and absolute ethanol. Finally, the sample was dried in a vacuum oven at 80 ℃ overnight for subsequent use.

6.2.2. Fabrication of M/Sb_2Se_3 hybrid membrane

Utilizing vacuum filtration method, a thin membrane of Sb_2Se_3 was fabricated. Various masses (1.5 mg, 3 mg, 4.5 mg, 6 mg) of Sb_2Se_3 in an aqueous solution were subjected to filtration through a hydrophilic PVDF membrane (Merck Millipore, 0.22 micrometres). This process yielded a thin layer of Sb_2Se_3 deposited onto the PVDF membrane. Following the vacuum filtration method, the deposition of Sb_2Se_3 on the bare membrane results in a transition from a white color to black.

6.2.3. Characterizations

The phase of the synthesized sample was verified through X-ray diffraction (XRD) analysis. The XRD measurement was carried out utilizing Cu Kα radiation with a wavelength of 1.54 Å, using a Rigaku Ultima III X-ray diffractometer. Raman spectroscopy (Witech) was conducted to examine the purity of Sb_2Se_3. Field-emission scanning electron microscopy (FESEM, Hitachi, S-4800) and high-resolution transmission electron microscopy (HRTEM, JEOL-JEM 2100) was utilized to investigate the morphology of the sample. The reflectance spectra of the prepared samples were recorded using a UV-Vis-NIR spectrophotometer (Shimadzu, UV-3600) in the range of 200 to 2000 nm. The surface temperature of our interfacial system was rigorously analysed using an infrared RAY CAM1886 camera. Inductively coupled plasma-mass spectrometry (ICP-MS, PerkinElmer model Avio-200) was employed to measure the ion content of the salt water before desalination

and the condensed water after desalination, imaging characterizations of macro channel was recorded by 3D optical microscope HIROX HR-01.

6.2.4. Theoretical methods

First principles calculations regarding electronic, vibrational and thermodynamic properties of Sb_2Se_3 are performed using the CASTEP (CAmbridge Serial Total Energy Package), based on density functional theory (DFT).[47,48] To describe the electron-ion interactions, norm conserving plane-wave pseudopotentials are deployed.[49] The exchange-correlation energy between different electrons is described by the Perdew–Burke–Ernzerhof (PBE) functional under the generalized gradient approximation (GGA) [50] including Koeling-Harmon relativistic treatment. [51] The electronic band-structure, electronic density of states (DOS), phonon dispersion, density of phonon states and thermodynamic properties are calculated against a $2 \times 7 \times 2$ k-point mesh, where the cut-off energy is limited to 440 eV. Both the shape and volume of the initial unit cell are optimized accompanying the relaxation of all atomic positions. In these calculations, convergence thresholds for energy, maximum displacement, maximum force and stress are chosen as 5 μeV/atom, 5.0×10^{-4} Å, 0.01 eV/Å and 0.02 GPa, respectively.

We performed the first principles calculations using Vienna ab-initio simulation package (VASP) [52-54]. The projector augmented wave (PAW) [55] method as implemented in VASP was applied for the all-electron frozen core calculations with plane wave basis set cut-off 500 eV. The Perdew−Burke−Ernzerhof (PBE) [56] functional was utilized to treat the exchange-correlation terms of the Hamiltonian

within the scope of generalized gradient approximation (GGA). The structural optimizations were carried out with the energy and force convergence criteria of 10^{-5} eV/ atom and 0.02 eV/Å respectively. K point mesh of (4×2×1) was implemented during the structural optimization of the surface slab with and without the adsorbate species. A vacuum slab of 20 Å perpendicular to the surface slab was considered during all the calculations to avoid any spurious interaction from the periodic images. All the calculations were carried out in spin unrestricted manner and the contribution of dispersive forces were taken into account using DFT+D3 Grimme's method [57].

The adsorption energy of adsorbate species on the Sb_2Se_3 surface slab was calculated using the following equation:

$$E_{Ads} = E_{S+A} - E_S - E_A$$

Where, E_{S+A}, E_S and E_A are the ground state energies of (Sb_2Se_3 surface + adsorbate), bare Sb_2Se_3 surface and a free unit of the adsorbate species respectively. The lower the value of E_{Ads}, the stronger is the adsorption. The values of E_A for NaCl, H_2O, Na and Cl was calculated by considering cubic $Fm\bar{3}m$ NaCl, an isolated H_2O molecule, trigonal $R\bar{3}m$ Na and an isolated Cl_2 molecule respectively as reference.

6.3. Results and discussion

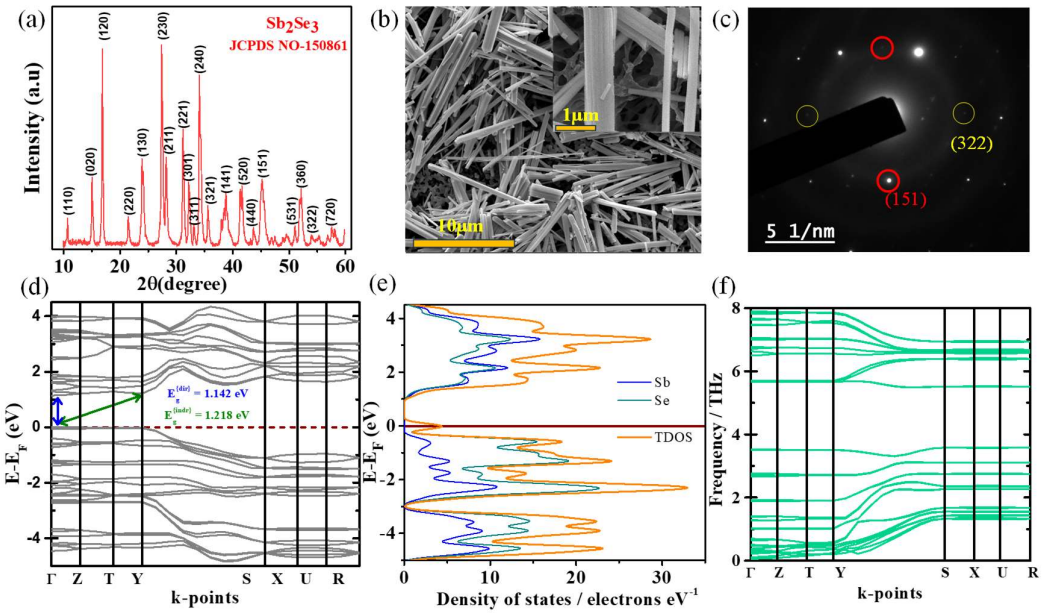

Figure 6.1. *(a) XRD (X-ray diffraction) pattern, (b) SEM (scanning electron microscope) image of Sb_2Se_3 nanorods on PVDF membrane; inset: higher magnification image of the same. and (c) SAED (selected area electron diffraction) pattern of Sb_2Se_3 nanorods, (d) electronic band-structure (direct and indirect band-gaps are indicated with blue and olive-coloured arrows, respectively), (e) total and projected density of states (TDOS and PDOS) with atomic contributions, (f) phonon dispersion of Sb_2Se_3*

Milligrams-level Sb_2Se_3 are synthesized via solvothermal method (See methods). The crystallinity and phase purity of the yielded are confirmed by the X-ray diffraction (XRD) pattern in (Figure 6.1(a)). All 2θ positions are well matched with JCPDS card no- 150861 corresponding to space group of Pbnm (62) orthorhombic phase of Sb_2Se_3. Absence of other peak confirms the pure phase of Sb_2Se_3 and peak intensity reflects the nature of high crystallinity. Moreover, Raman

vibrational modes figure 6.2 (a) at 114 for pure Sb vibrations, 186 for Sb-Se heteropolar vibrations, 249 for Sb-Sb bond vibrations, 368 and 447 $cm^{-1}$for Sb-Se stretching vibrations again confirms the pure phase of Sb_2Se_3. [58-62] Morphology of the as synthesized Sb_2Se_3 is examined by field emission scanning electron microscope (FE-SEM) image in (Figure 6.1(b)), which evinces rod like structure, having length up to few micrometers and diameter <1 micrometer. Morphology is further confirmed by transmission electron microscopy image figure 6.2 (b-c). The Sb_2Se_3 NRs are randomly stacked in porous PVDF membranes. The higher magnification FESEM image in inset of (Figure 6.1b) shows Sb_2Se_3 laden nano-porous PVDF membrane which shows that after fabrication of vacuum assisted PVDF (M)/ Sb_2Se_3 hybrid membrane, the porous skeleton of PVDF membrane is intact. Furthermore, selected area electron diffraction (SAED) pattern in (Figure 6.1(c)) corroborates well with the XRD results.

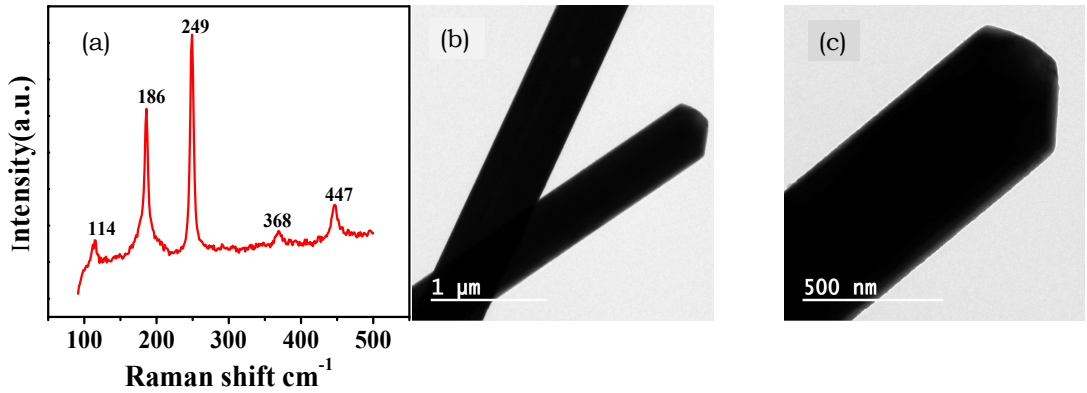

Figure 6.2. *(a) Raman spectra of Sb_2Se_3 nanorods (b) low magnification and (c) high magnification Transmission electron microscope image (TEM) of Sb_2Se_3 nanorods*

Further density functional calculations are performed to understand the band structures and vibrational properties of Sb_2Se_3. Based on the orthorhombic Sb_2Se_3 unit cell as per the *Pnma* space group, the following high-symmetry k-path is chosen for band structure calculations: $\Gamma \rightarrow Z \rightarrow T \rightarrow Y \rightarrow S \rightarrow X \rightarrow U \rightarrow R$. The electronic band-structure in this path and DOS are displayed in (Figure 6.1(d-e)). From band-structure, we find the direct gap is, $E_g^{dir} = 1.142$ eV at the Γ −point, while an indirect gap of $E_g^{indr} = 1.218$ eV can also manifest between the valence band maximum (VBM) at the Γ −point and a local conduction band minimum (CBM) at the Y −point.

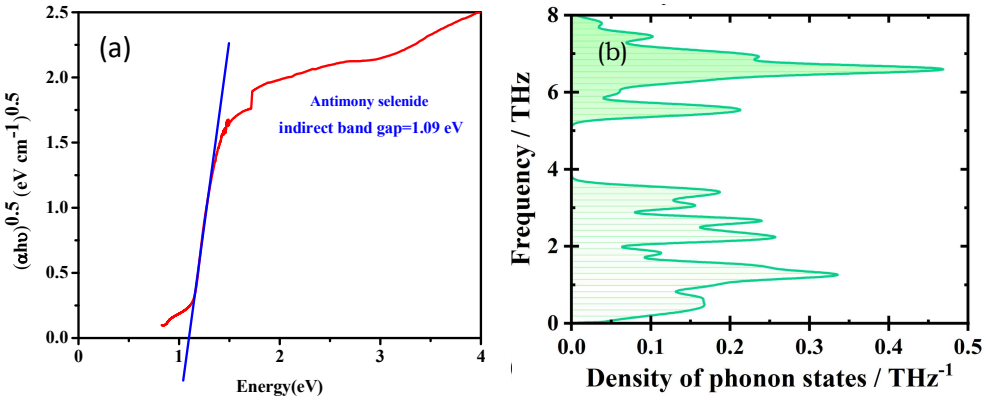

Figure 6.3. *(a) Kubelka-Munk plot (b) Density of phonon states*

Experimentally, in figure 6.3 (a) a little lower indirect gap is detected (1.09 eV), which might be ascribed to surface defects. The projected DOS suggests that, the major contributor in the valence band is the Se atoms, while in the conduction band, Sb atoms contribute slightly higher. Various electronic attributes accord with the previous literature. [63] Standard sunlight (AM 1.5) having average energy (~1.6 eV) excites the carrier of Sb_2Se_3 to a significantly higher energy levels than the band edges. The generated electron-hole pairs above the bandgap relaxes near the band

edges and converts extra energy into heat through photo-carrier thermalization process. Notably, understanding of the photo-carrier relaxation process is quite complicated in nature. So, we further calculate the phonon band structure (Figure 6.1**(**f)) and density of phonon states figure 6.3 (b) following the same symmetry path along with LO-TO splitting.[64] All phonon bands have positive frequency, which means, the system is dynamically stable. The flat branches in phonon dispersion in (Figure 6.1**(**f)) decipher low group velocities of acoustic phonons indicating low thermal conductivity, which is desirable for efficient solar heat capture as it allows the material to maintain a higher temperature. Moreover, a forbidden gap is present at $\sim(4-5)$ THz between a section of optical bands specified in figure 6.3(b), which therefore can suppress phonon-phonon scattering for particular phonon energy.[65] Consequently, the heat generation in Sb_2Se_3 predominantly attributes to the electron/hole- acoustic phonon scattering mechanism which corroborates well with previous findings for low band gap semiconductors.[28] Furthermore, a low phonon DOS at smaller frequencies typically limits the thermal conductivity in Sb_2Se_3.

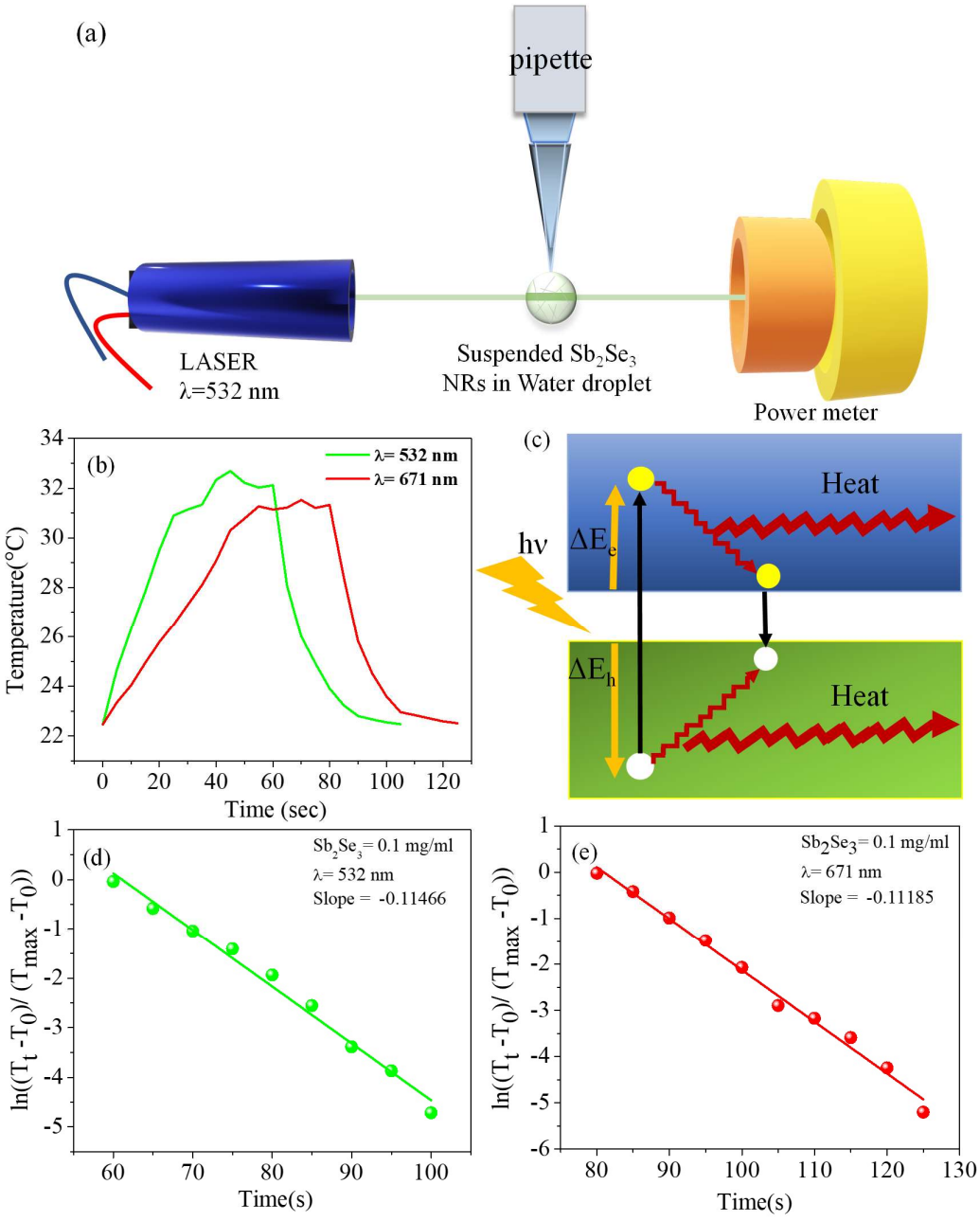

Figure 6.4. *(a) Schematic of Sb_2Se_3 suspended water droplet laser heating experiment for evaluating light-to-heat conversion efficiency; (b) Heating and cooling of water droplet containing Sb_2Se_3 under two lasers, (c) Schematic of heat generation process and (d-e) Determination of slopes from cooling region by $ln\left(\frac{T-T_0}{T_{max}-T_0}\right)$ Vs. time. plot*

6.3.1. Laser heating experiment

Efficient conversion of light to heat is pivotal for the effectiveness of photothermal materials. So, the first attempt is made to investigate the light-to-heat conversion efficiency of Sb_2Se_3 nanorods before proceeding to desalination performance. The conventional assessment of solar-to-heat conversion efficiency in desalination provides a comprehensive overview of the overall conversion process. [66] In contrast, a meticulously controlled experiment (Figure 6.4**(**a)) employing interaction of laser light and Sb_2Se_3 suspended droplet offers a detailed analysis of light-to-heat conversion efficiency at a specific wavelength. A droplet of diameter (2.5 mm) is hung by an PTFE pipette which is illuminated by monochromatic laser beam (671 and 532 nm) with incident laser power 100 mW and laser beam spot size was 0.5 mm in diameter. Consequently, droplet containing Sb_2Se_3 absorbs light and gains heat. The subsequent heat generation in the droplet is quantified using a pre-calibrated infrared camera as shown in figure 6.5.

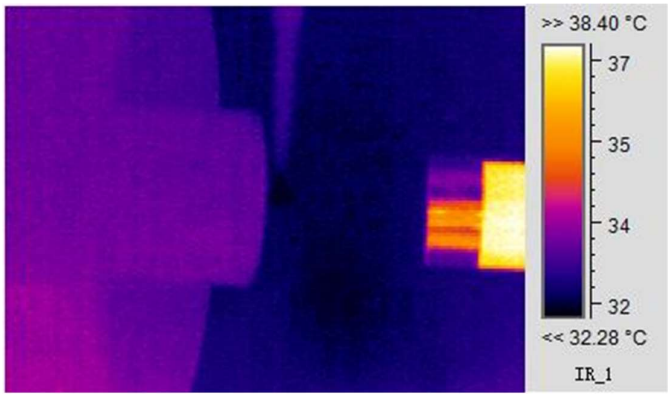

Figure 6.5. *IR image of water droplet (contained Sb_2Se_3 nanorods)-laser experiment*

(Figure 6.4**(**b)) evinces the distinct elevation of temperature for 671 and 532 nm laser. When equilibrium is reached (fluctuation of temperature is less than 1 °C) the

laser beam was shut off. Instantly, droplet starts cooling and the temperature slowly falls down to the room temperature with increase of time scale. In (Figure 6.4(b)), the time of laser shut off for green and red laser was 60 and 80 sec, respectively. The process of heat generation is schematically described in (Figure 6.4(c)), leading to the photothermal effect in Sb_2Se_3 which is called carrier thermalization.[67]

The incident beam of laser absorbed by Sb_2Se_3 comprises of two parts, one part of gaining heat energy is converted to the internal energy of the droplet - Sb_2Se_3 system. This is empirically witnessed in figure 6.4(b), where there is a distinct elevation in the temperature of the droplet followed by reaching a state of equilibrium. The other part of the heat energy gets dissipated to the environment. Hence, the full process is described by the energy balanced equation;

$$P\eta = \frac{dQ_i}{dt} = mc_p \frac{dT}{dt} + \frac{dQ_{ext}}{dt} \quad \ldots\ldots (1)$$

P is the power that is absorbed by the droplet. η is the light-to-heat energy conversion efficiency of the material. Q_i is the gained heat energy of the droplet. m, C_p, T are mass, heat capacity and temperature of the droplet respectively. Q_{ext} is the heat energy that is dissipated to the environment from the droplet. Therefore, the absorbed light power by the droplet is,

$$P = P_{in} - P_{out} = P_{in}\,(1 - 10^{-A_\lambda}) \quad \ldots\ldots (2)$$

$$A_\lambda = -log_{10}\,\frac{P_{in}}{P_{out}} \quad \ldots\ldots (3)$$

Where A_λ is the light absorbance of Sb_2Se_3, P_{in} and P_{out} are the incident and transmitted laser power before and after absorption by the Sb_2Se_3 droplet,

respectively. This procedure is regarded as unaffected by the shapes and size distribution of the materials involved.

6.3.1.1 Cooling stage of laser beam

When equilibrium is reached (fluctuation of temperature is less than 1 °C) the laser beam was shut off. Instantly, droplet starts cooling and the temperature slowly falls down to the room temperature with increase of time scale. In figure 6.4**(**b), the time of laser shut off for green and red laser was 60 and 80 sec, respectively. The energy balance equation during this refrain stage of temperature,

$$mc_p \frac{dT}{dt} + \frac{dQ_{ext}}{dt} = 0 \qquad \text{..... (4)}$$

According to the Newtons cooling law, the heat dissipation is proportional to the difference between droplet temperature and its surroundings;

$$\frac{dQ_{ext}}{dt} = F(T - T_0) \qquad \text{.... (5)}$$

F is the proportional coefficient of heat loss. T is the temperature of the droplet and T_0 is the temperature of the ambient air. Replacing $\frac{dQ_{ext}}{dt}$ by – $mc_p \frac{dT}{dt}$ and integrating the equation (5) from maximum temperature, T_{max} to ambient temperature T_0 we get,

$$T = T_0 + \left(T_{eq} - T_0\right) e^{-\left(\frac{F}{mc_p}\right)t} \qquad \text{... (6)}$$

Where T_{max} has been taken when temperature fluctuation is all about (±1 °C). Finally,

$$F = -\frac{ln\left(\frac{T-T_0}{T_{max}-T_0}\right)}{t} mC_p \qquad \text{..... (7)}$$

(Figure 6.4(d-e)) depict the representative plot of $ln\left(\frac{T-T_0}{T_{max}-T_0}\right)$ vs. time in cooling stage for green and red laser, respectively which are fitted linearly. The corresponding slopes for green and red laser are -0.11466 and -0.11185, respectively. However, Sb_2Se_3 concentrations is very low 0.1 mg mL^{-1} and it presumably does not contribute to the heat capacity of Sb_2Se_3. So, heat capacity C_p of water is 4.2 j g^{-1} and density of the droplet is 0.996 g mL^{-1}. In this calculation water droplet shrinkage is negligibly small. Evaporation induced heat loss are already incorporated in the value F. At equilibrium the energy balance equation can be described as,

$$P\eta = \frac{dQ_i}{dt} = \frac{dQ_{ext}}{dt} \quad \ldots\ldots (8)$$

$$P_{in}(1-10^{-A_\lambda})\eta = F\left(T_{eq}-T_0\right) \quad \ldots\ldots (9)$$

$$\eta = \frac{F(T_{eq}-T_0)}{P_{in}(1-10^{-A_\lambda})} \quad \ldots\ldots (10)$$

Eventually, the light to heat conversion efficiency (η) of Sb_2Se_3 are found 58% and 57.8% for green and red laser respectively. The light-to-heat conversion efficiency (η) is quantified by $\eta = \frac{F(T_{eq}-T_0)}{P_{in}(1-10^{-A_\lambda})}$. Where $F = -\frac{ln\left(\frac{T-T_0}{T_{max}-T_0}\right)}{t} mC_p$; T_{eq} =equilibrium temperature; T_0 = ambient temperature; P_{in} = input power of laser; A_λ = light absorbance of Sb_2Se_3.[66] The details calculations are provided in supporting information. (Figure 6.4(d-e)) depict the representative plot of $ln\left(\frac{T-T_0}{T_{max}-T_0}\right)$ vs. time in cooling stage for green and red laser, respectively which are fitted linearly. Eventually, the light-to-heat conversion efficiency (η) of Sb_2Se_3 are found 58% and 57.8% for green and red laser respectively. The relevant parameters of efficiency calculations are enlisted in subsequent table 6.1.

Table 6.1: Relevant parameters in water droplet experiment.

Wavelength (λ) nm	Concentration (mg/mL)	A λ	T_{equ} (°C)	Time to achieve equilibrium (s)	F (J s^{-1} $°C^{-1}$)	η
671	0.1	0.338	30.82	61.04	0.003825	0.578
532	0.1	0.395	31.50	34.63	0.003921	0.580

6.3.2. Carrier thermalization process

Upon illumination, Sb_2Se_3 absorbs light energy above the bandgap otherwise it transmits the light. For above bandgap illumination, the excess energy distributed between electron and hole in the way, $\Delta E_e = \left(h\nu - E_g\right)(1 + \frac{m_e^*}{m_h^*})^{-1}$ and $\Delta E_h = (h\nu - E_g) - \Delta E_e$.[67] ΔE_e is the energy difference between conduction band bottom and energy of the electron above conduction band bottom. ΔE_h is the energy difference between valence band top and energy levels of holes below the valence band top. E_g is the bandgap of semiconductor. m_e^* and m_h^* is the effective mass of electrons and holes respectively. In the initial stage, prior to illumination, carrier distributions in the semiconductor are not Boltzmann-like. Upon continuous illumination, photo-carriers in the semiconductor exhibit a Boltzmann-like distribution. If photon absorption takes place above the bandgap, the surplus kinetic energy results in electrons and holes residing within kT above the bottom of the conduction band and below the top of the valence band, respectively. Hot carriers, characterized by

electron and hole temperatures surpassing the lattice temperature, undergo relaxation to the conduction band edge and valence band edge, respectively. This relaxation process results in the generation of heat and is commonly referred to as carrier thermalization, signifying the establishment of a thermal distribution.

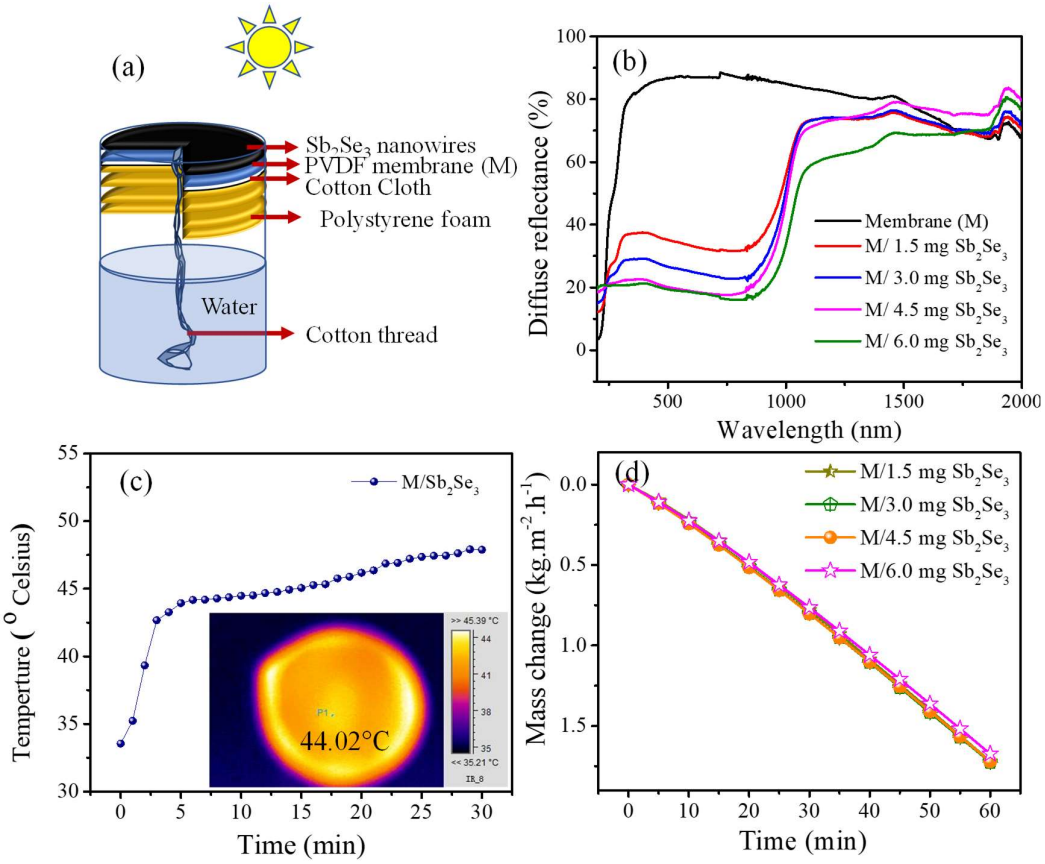

Figure 6.6. *(a) Schematic of photo assisted desalination experimental set-up, (b) Diffuse reflectance spectra of hybrid PVDF membrane (M)/ Sb_2Se_3 membrane with different amount of mass loading (c) Photothermal heat generation of M/ Sb_2Se_3 hybrid membrane under mercury vapor lamp (1000 W/m²) and IR image of the same at an intermediate time (d) Mass loss of 3.5 wt% NaCl saline water for various mass loaded hybrid membranes under illumination of mercury vapor lamp*

6.3.3. Feasibility of photothermal behavior on evaporation system

Driving by promising light-to-heat conversion efficiency, we have integrated Sb_2Se_3 nanorods in solar desalination devices. (Figure 6.6(a)) demonstrates customized experimental set-up for water desalination experiment with specified component similar to described in literatures.[12] Here, solar absorber layer is designed by a uniform Sb_2Se_3 nanorods film deposited on PVDF membrane (pore size 0.22 μm) by vacuum filtration method. The randomly distributed Sb_2Se_3 nanorods modifies the surface of porous network of PVDF membrane (M), retaining its original structure as previously indicated in (Figure 6.1(b)). Thereafter, M/Sb_2Se_3 hybrid membrane with different mass loading of Sb_2Se_3 is used in solar absorber module for studying desalination experiment.

The photothermal conversion efficiency of the hybrid membrane mainly depends on how strong their optical absorption in the range (200-1200 nm) is. Following reflectance measurements (Figure 6.6(b)), it was found that the bare membrane exhibits strong reflection more than 80% over the visible-NIR spectral region. Whereas upon designing of M/Sb_2Se_3 hybrid membrane, there is a drastic reduction of reflectance, owing to strong absorption of visible-NIR light. It is also observed that upon enhancing mass loading the visible-NIR region spectral reflectance is consistently decreasing owing to the enhanced absorbance and 6 mg Sb_2Se_3 loaded membrane shows only 20 % reflectance in VIS -near IR region. Importantly, thicker layer of Sb_2Se_3 leads less reflectance due to its high absorption coefficient 10^5 cm^{-1} at shorter wavelength side. Notably, in solid-air interfaces light suffers more scattering loss than solid-liquid interface. As a consequence of capillary

rise of water, the membranes become wet slowly and suffers less scattering, thus absorbs more light, mainly in IR region. Importantly, M/ 6.0 mg Sb_2Se_3 membrane in wet condition suffers comparatively more scattering loss than 4.5 mg membrane Figure 6.7 which confirms that water distribute more uniformly in 4.5 mg membranes.

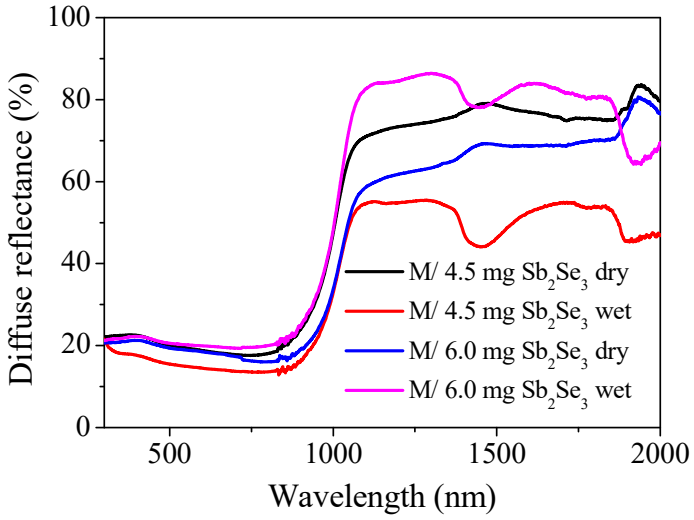

Figure 6.7. *Diffuse reflectance spectra of M/4.5 mg Sb_2Se_3 and M/ 6.0 mg Sb_2Se_3 in dry and wet conditions*

For feasible water evaporation, the surface temperature of the Sb_2Se_3 evaporator module under the mercury vapor lamp with intensity of (1000 W m^{-2}) is recorded by a thermocouple first. As shown in (Figure 6.6©), the surface temperature of M/Sb_2Se_3 hybrid membrane in the evaporator module is elevated from room temperature after a few minutes of illumination, which is progressively

increasing with time, reaches ~ 48 ℃ after 30 minutes. At intermediate time (5 minutes) it evinces a temperature 44.05 ℃ in thermal camera, (inset of (Figure 6.6**(**c)) which corroborates well with thermocouple results. Highest recorded temperature is ~ 59 ℃ represented in figure 6.8.

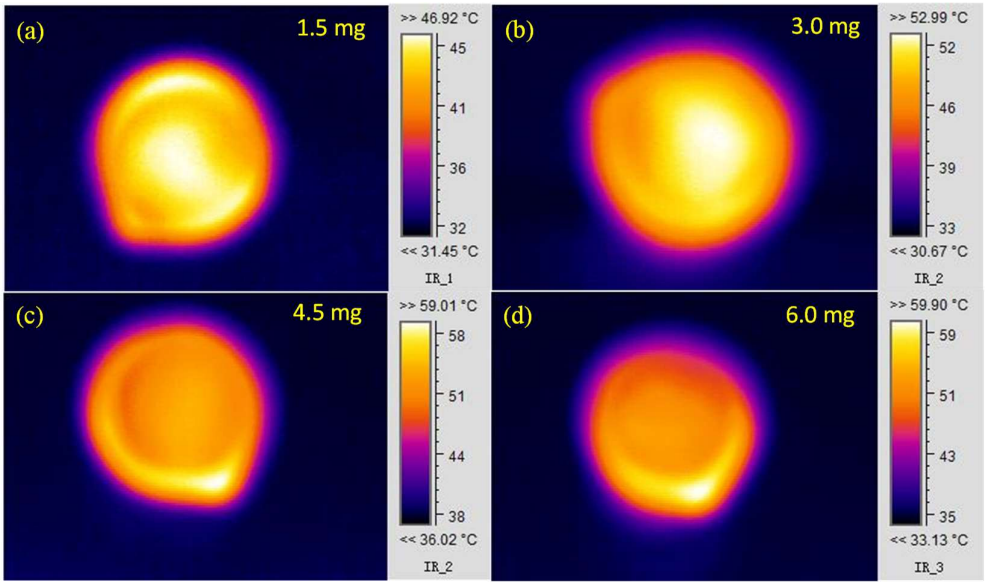

Figure 6.8. *IR image of (a) M/Sb_2Se_3 (1.5 mg), (b) M/Sb_2Se_3 (3.0 mg), (c) M/Sb_2Se_3 (4.5 mg), (c) M/Sb_2Se_3 (6 mg)*

This generated heat then instigates the saline water (3.5 wt% NaCl) evaporation process and finally pure water can be collected by condensation process, retaining the salt at the surface of hybrid membrane figure 6.9 (a). (Figure 6.**3(**d)) provides the overview about the desalination performance of the designed hybrid membranes, showing mass loss of saline water as noted with course of time. It is found that the mass losses for M/ 1.5, 3, 4.5 mg hybrid membranes are quite similar (1.72 kg m^{-2} h^{-1}) in nature. However, for 6 mg Sb_2Se_3 loaded membrane, mass loss is slightly

declining to 1.67 kg m^{-2} h^{-1}. Hence, the desalination performance trend is quite conflicting with mass loading of Sb_2Se_3, although the trend of absorbance (reflectance measurement) and photothermal heat generation are consistently elevated with increase of mass loading; figure 6.8 In principle, the solar evaporation efficiency depends not only on absorption of visible-NIR light and rise in localized temperature but intrinsically connected with the water content supplied timely to the hot zones. In experiment, PVDF membrane (pore size = 0.22 μm.) of the absorbing module supplies water to the hot surfaces efficiently, owing to its porous and hydrophilic nature. However, upon fabrication of hybrid membrane, the top surface turns into hydrophobic nature; figure 6.9(b), which hinders uniform water transport from bottom PVDF membrane to the hot surface of Sb_2Se_3 layer, restricting the faster water evaporation. Thus, increase of mass loading/thickness of Sb_2Se_3 layer further delays the water transport to the hot zones and limits the evaporation rate.

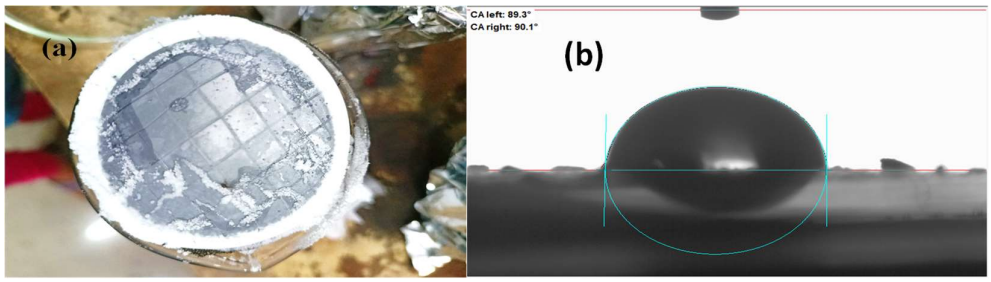

Figure 6.9. *(a) Digital photograph of salt retaining on membrane after 1 hour desalination experiment (b) Contact angle of PVDF (M)/Sb_2Se_3 hybrid film*

To remove the delay of water transport to the hot zones the skeleton of solar absorber module is very important for revealing the best performance of the absorbing material. The limitation is successfully eliminated by introducing the concept of mechanical imprinting of macro-channel over the hybrid membrane. The imprinted channel creates favorable water transport path from bottom PVDF membrane to Sb_2Se_3 layer and therefore evenly distributes the water in hot zones and making evaporation rate much higher. Schematic in (Figure 6.10), presents the brief process of inscribing macro-channel over M/Sb_2Se_3 hybrid membrane where a metal mesh is employed to pattern the channel. By choosing suitable mesh one can easily mimic the process in large scale and vary the channel width and distance simultaneously.

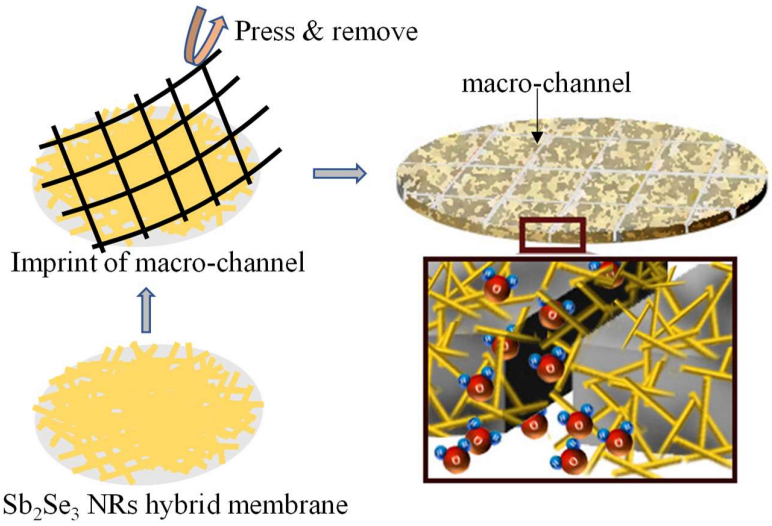

Figure 6.10. *Schematic illustration of macro-channel imprint process in M/Sb_2Se_3 hybrid membrane*

6.3.4. Validation of macro-channel influence in desalination

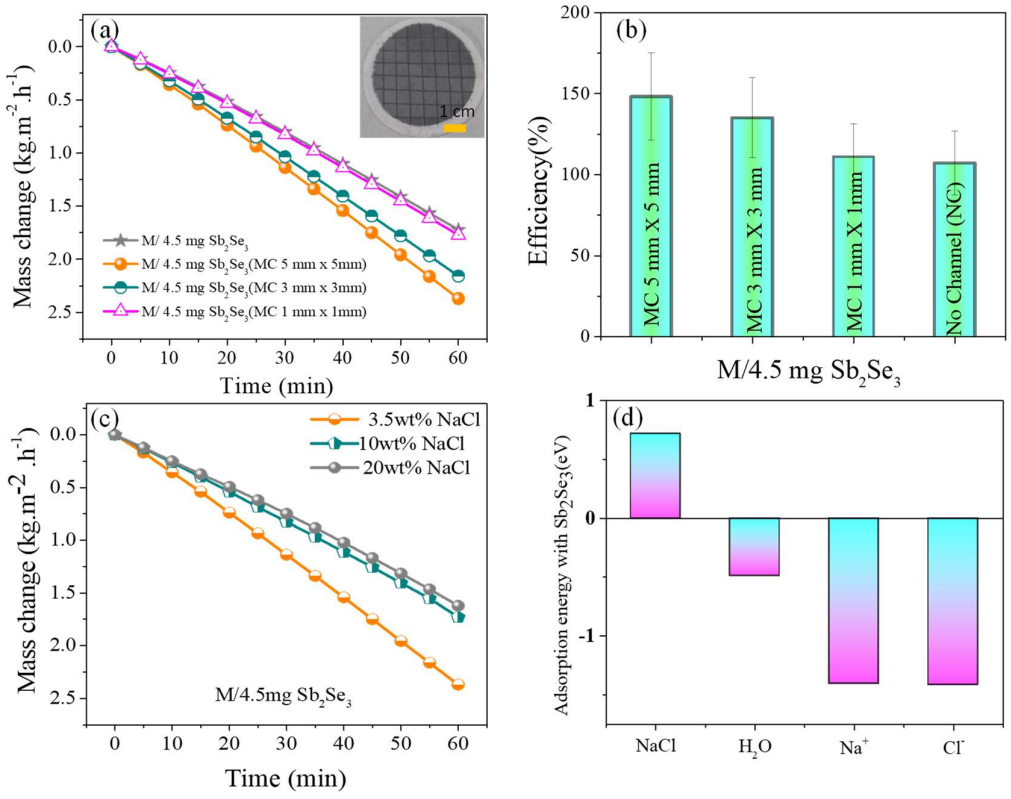

Figure 6.11. *(a) Effect of macro-channel on desalination performance of M/4.5 mg Sb_2Se_3 and corresponding; inset: channel inscribed membrane (b) corresponding evaporation efficiency Desalination performance on salinity variation of (c) M/4.5 mg Sb_2Se_3 and (d) adsorption energy of NaCl, H_2O, Na^+ and Cl^- on (230) surface of Sb_2Se_3*

(Figure 6.11(a)) demonstrates the prominent effect on desalination performance of macro-channel mechanically inscribed in the M/Sb_2Se_3 hybrid membrane. Furthermore, the separation of channels is carefully optimized by choosing different mesh of $1\,mm \times 1\,mm, 3\,mm \times 3\,mm$ and $5\,mm \times 5\,mm$ separation. The dominant effect is found for 4.5 mg M/Sb_2Se_3 hybrid membrane with $5\,mm \times 5\,mm$ channel, displaying maximum mass loss of 2.37 kg m^{-2} h^{-1}, which is elevated from the no channel counterpart (mass loss only 1.72 kg m^{-2} h^{-1}). Solar evaporation efficiency is an important factor for evaluating the performance of the absorber module which is calculated by formula, $\eta = \frac{m.h}{E}$; where η is the receiver efficiency, m is the mass evaporation rate of water and h is the total enthalpy of water transport from the liquid to vapor phase (2260 J g^{-1}).[12] E_{in} (kJ m^2 h^{-1}) is the corresponding power density of the incident light (1000 W m^{-2}). (Figure 6.11(b)) presents the corresponding solar evaporation efficiency of 4.5 mg M/Sb_2Se_3 hybrid membrane with macro-channel. It is found that the solar evaporation efficiency gradually increases from ~ 107 (no channel) to 111 ($1\,mm \times 1\,mm$), 135 ($3\,mm \times 3\,mm$), 148 % ($5\,mm \times 5\,mm$) respectively, establishing the prominent role of endowed macro-channel. Similarly, 1.5, 3 and 6 mg M/Sb_2Se_3 hybrid membrane with $5\,mm \times 5\,mm$ channel, shows improved desalination performance, offering 1.77, 2.04 and 2.09 kg m^{-2} h^{-1} mass loss respectively than the no channel counterpart; figure 6.12. Notably, the evaporation rate of 4.5 mg M/Sb_2Se_3 hybrid membrane (MC $5\,mm \times 5mm$) is better than the rest of the membranes.

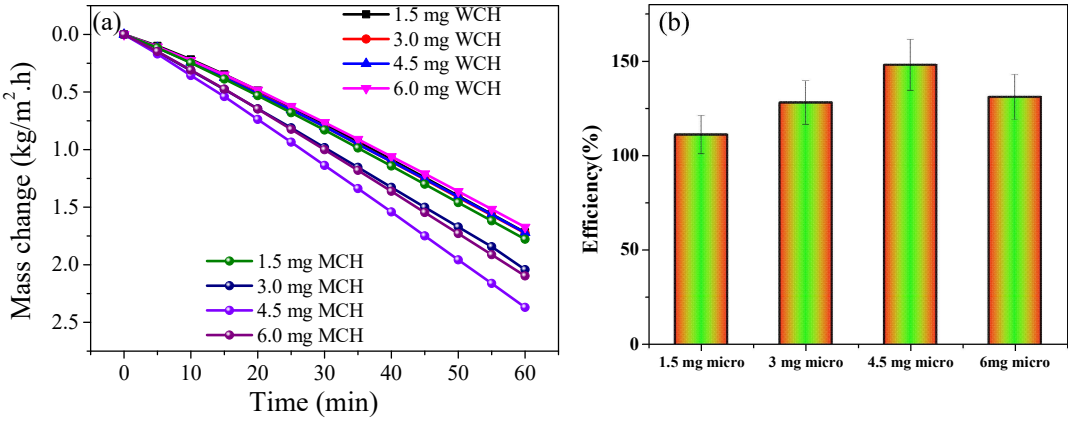

Figure 6.12: *(a) Desalination performance of the hybrid membranes with and without channel and (b) Solar evaporation efficiency of M/ 1.5, 3.0, 4.5 and 6.0 mg Sb_2Se_3 hybrid membranes*

3D optical images of macro-channel are provided in figure 6.13.

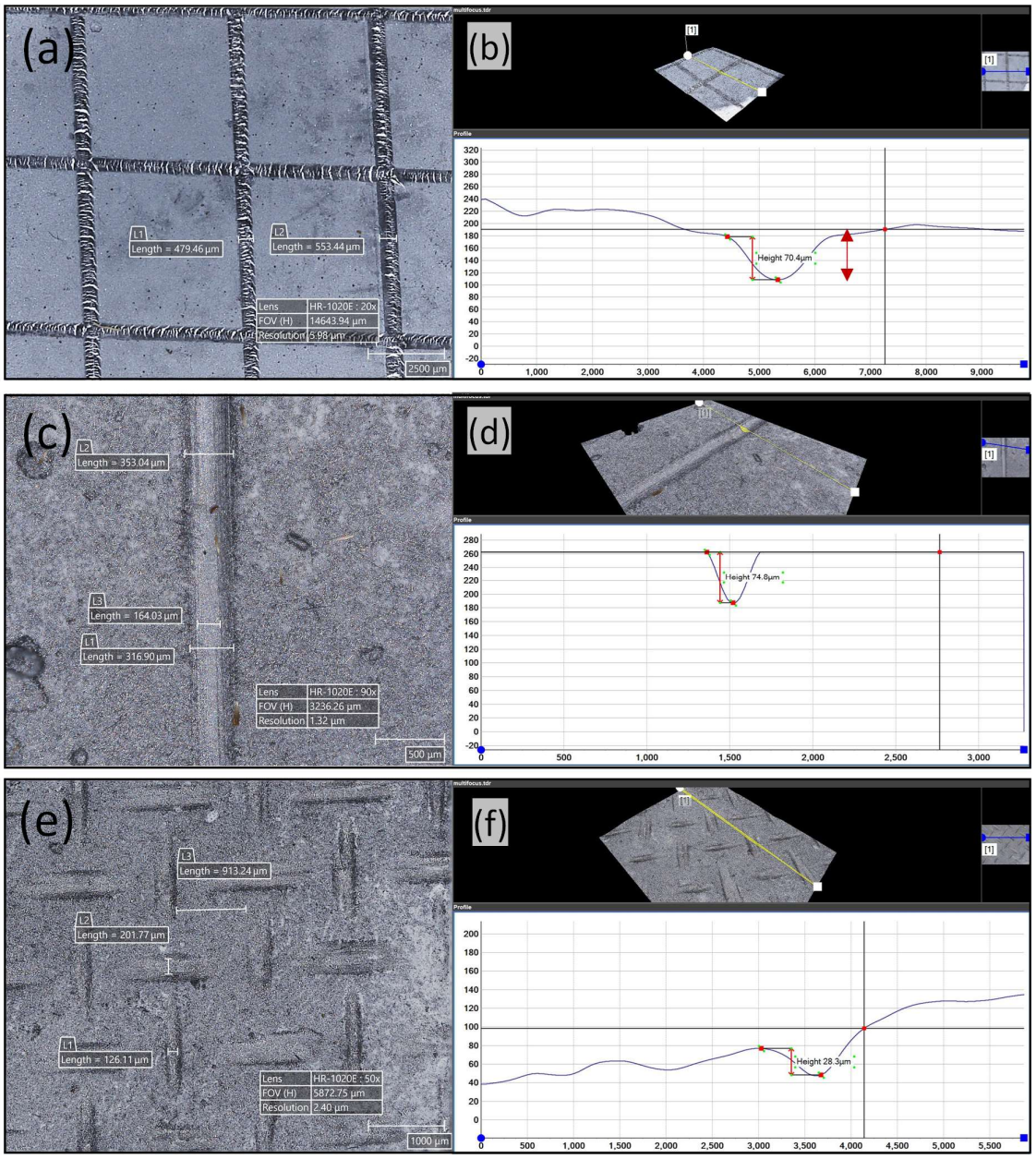

Figure 6.13. *3D microscope images of (a-b) 5mm x5 mm MC, (c-d) 3mm x 3 mm MC and (e-f) 1mm x 1mm MC 4.5 mg hybrid membrane*

The strong electromagnetic absorption capacity, (which was shown in the above absorption curve), increase of localized temperature zone and reinforcement of the

diffusion limited absorber surface by inscribing macro-channel, lead to the better desalination performance. Nevertheless, one of major limitations for profitable vapor generation is the thicker layer of hot zones. In thicker layer, vapor molecule could not escape easily from the membrane, longer time is required. Meanwhile they loss some of its energy and returns back into liquid form. In shallow level, vapor molecule easily escapes from the surface without losing any energy during its travelling path. Therefore, from 4.5 to 6 mg thicker absorber, the corresponding evaporation efficiency drops from 148 % to 131 %. In spite of stronger electromagnetic absorption in 6 mg sample, the decrease in evaporation efficiency is attributed to the increase of thickness of the absorber layers, rendering longer evaporation time. Thus, achieving an optimal sample loading (Figure 6.14) becomes crucial to maintain a balance between light absorbance and water transfer rate.

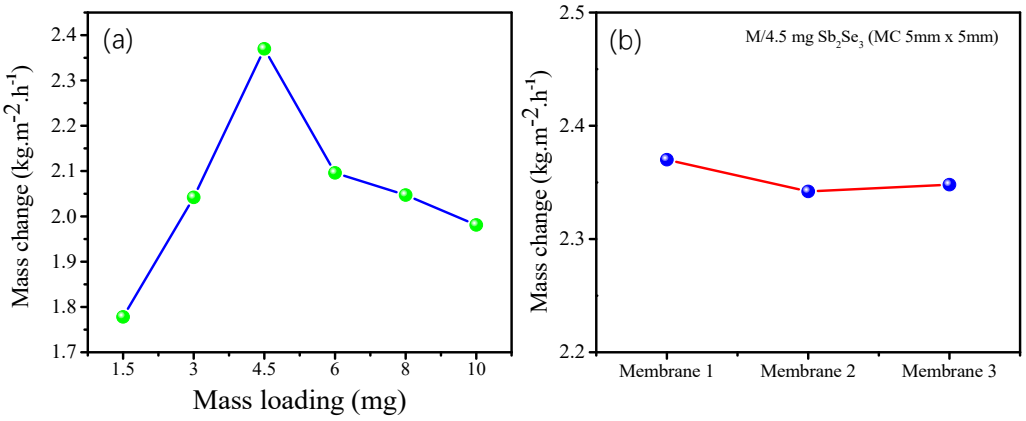

Figure 6.14. *(a) Evaporation rate of different mass loaded hybrid membrane and (b) Evaporation rate after 1hour of light illumination of three different 4.5 mg MC 5 mm x 5mm hybrid membrane*

The outstanding performance in evaporation efficiency of Sb_2Se_3 can be elucidated by energy exchange between the solar evaporator and the surrounding environment. Under white light illumination of intensity (1000 W m^{-2}) the top surface temperature of the absorber is higher than the surrounding environment temperature causes an energy loss to the environment by thermal convection and thermal radiation. The lower temperature of the sidewall of the evaporator module drag temperature from surrounding environment by thermal convection and thermal radiation. The net energy (E_{en}) obtained from the surrounding environment during the water evaporation time can be calculated by [14]

$$E_{environment} = -A_1\epsilon\sigma\left(T_1^4 - T_s^4\right) - A_2\epsilon\sigma\left(T_2^4 - T_s^4\right) - A_1h\left(T_1 - T_s\right) - A_2h\left(T_2 - T_s\right) - E_{conduction} \quad \ldots\ldots (11)$$

Where $E_{environment}$ is the net energy gained from the environment. A_1 (12.56 cm^2) and A_2 (135 cm^2) are the top and sidewall areas of the evaporator module respectively. ϵ is the emissivity of the absorber (0.83) and σ is the Stefan-Boltzmann constant (5.67 $\times 10^{-8}$ W m^{-2} k^{-4}). h is the convection heat transfer coefficient assumed to be (10 W m^{-2} k^{-1}). T_1 (44 ℃) and T_2 (28 ℃) are the top and sidewall evaporation surface temperature respectively during evaporation time. T_s (38 ℃) is the surrounding temperature during evaporation. By calculating environmental energy gain during experiment, the environmental energy gain is 1.958 W and which is conducive to efficiency greater than 100%. A comparison table (Table 6.2) is provided, highlighting key parameters affecting heat gain and environmental heat gain reported in previous studies.

Table 6.2. comparison table highlighting key parameters affecting heat gain and environmental heat gain reported in previous studies

Material	Emissivity	Light	Top surface area	Side area (wall surface)	Top surface temperature (T_1) °C	Side surface temperature (T_2) °C	Surrounding environmental temperature (T_e) °C	Net energy gained	References
HM-MO_5N_6/ MF	0.94	Xenon lamp	3 cm^2	30 cm^2	45 °C	20 °C	27 °C	0.1795 W	[14]
MXene - decorated cellhouse acetate	0.90	CEL-HXF 300-T3 solar simulator	3.88 cm^2	65.94 cm^2	31.2 °C	21.6 °C	23.5 °C	0.1487 W	[75]
V -rGO foam	0.98	CEL-HXUV 300 solar simulator	1.62 cm^2	1.80 cm^2	35.2 °C	28.0 °C	33.1 °C	0.00909 W	[13]
rGO based aerogel sheet	0.90	Solar simulator Newport Oriel	21.23 cm^2	163.2 cm^2	29.2 °C	19.4 °C	25 °C	1.31 W	[76]
Sb_2Se_3 nanorods	0.83	Mercury - Vapor lamp	12.56 cm^2	135 cm^2	44 °C	28 °C	38 °C	1.95 W	This work

6.3.5. Variations in evaporation rate influenced by changes in salinity concentration

While investigating the influence of salinity concentration on evaporation rate, we found that owing to increase of salinity concentration mass evaporation rate decreases consistently. In theory, Raoult's law states $P_{solution} = X_{solvent} \times P_{solvent}$; where $P_{solution}$ = Vapor pressure of the solution, $X_{solvent}$ = mole fraction of the solvent, $P_{solvent}$ = Vapor pressure of the pure solvent. Elevated salt concentration in saline water (3.5 to 10 and 20 wt%) leads to a reduced mole fraction of pure water, consequently resulting in decreased vapor pressure of the solution, thereby lowering the rate of mass evaporation (2.37 to 1.72 and 1.62 kg m^{-2} h^{-1}), shown in figure 6. 11(c). Moreover, binding strength of NaCl, H_2O, Na^+ and Cl^- is very crucial to understand salt adsorption in Sb_2Se_3 surfaces during water evaporation process. Therefore, we further studied the adsorption of an NaCl block, a H_2O molecule, an Na and a Cl atom on the (230) Miller plane of Sb_2Se_3. The adsorption energy of NaCl, H_2O, Na and Cl on the (230) Sb_2Se_3 surface slab was calculated to be 0.72 eV, -0.49 eV, -1.41 eV and -1.42 eV respectively. Na and Cl atoms were found to be coordinated with nearby Se and Sb atoms. The site preference of Na and Cl atoms arises most likely from their electronegativity differences. The H_2O molecule interacts with the Sb_2Se_3 surface only via weak van der Waals interactions. The adsorption energy analysis reveals that the binding strength of H_2O to the Sb_2Se_3 is stronger than NaCl. However, the binding strength of isolated Na^+ and Cl^- ions are significantly higher as prominent from the considerably negative adsorption

energies of Na and Cl atoms on the Sb_2Se_3 surface which instigates to successful separation of salt during water evaporation.

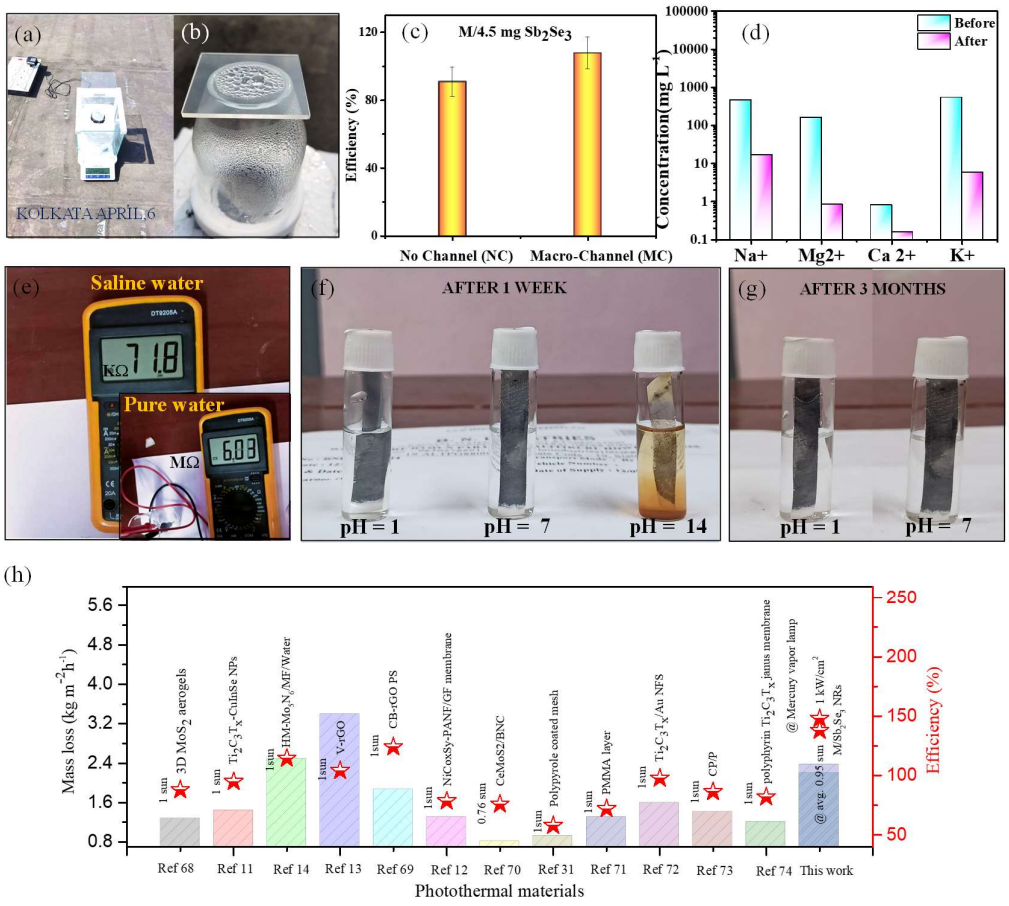

Figure 6.15. *Digital photograph of (a) Desalination experiment in outdoor sunlight with an average intensity 950 W/m², (b) Condensation of water vapor after 2 hours outdoor sunlight irradiation. (c) evaporation efficiency of M/4.5 mg Sb_2Se_3 no channel and macro-channel under outdoor solar intensity of 950 W/m². (d) ICP-MS (Inductively coupled plasma mass spectrometry) data collected before and after desalination experiment (e) Water purification experiment by a multimeter before and after desalination respectively. Digital photographs of M/Sb_2Se_3 exposed to various pH value (f) (pH =1,7,14), (g) (pH =1,7) after 1 week and 3 months respectively. (h) Comparison of M/4.5 mg Sb_2Se_3 hybrid membrane with several best performing hydrophilic and hydrophobic photothermal materials.*

For practical implementation the photothermal evaporation of the absorber is performed in the outdoor sunlight at 36°C, relative humidity 66%. (Figure 6.15(a)) displays the digital photograph of the evaporator module placed on the balance machine under sunlight of average intensity 950 W m^{-2}. The evaporator module comprises of two parts, salt water reservoir container and condensation chamber. In former chamber polyethylene foam was used to resist the heat transfer from membrane towards water. A continuous water transport from the bottom of the water reservoir to the membrane is facilitated by a cotton thread. A thermocol's white cover was utilized to shield against any form of environmental radiation disturbance. Direct sunlight is incident on the membrane through the quartz plate without absorption loss. (Figure 6.15(b)) displays water condensation in the top chamber. Water was collected from the tiny openings in the white segment. In (Figure 6.15(c)) the evaporation efficiency of M/4.5 mg Sb_2Se_3 is 91% when no channel is inscribed over it. Whereas upon mechanical imprint of macro-channel, the efficiency reaches 108% which justify the importance of macro-channel. Moreover, collected ICPMS data in (Figure 6.15(d)) shows the purity of collected water from the condensation chamber. Only nominal 16.97, 0.85, 0.16 and 5.95 mg L^{-1} traces of Na^+, Mg^{2+}, Ca^{2+} and K^+ are found which are in line with the health standards set by the World Health Organization (WHO). These results thus demonstrate the superior desalination performance of the hybrid membrane. Moreover, after desalination the condensed water displays a resistance value ~ 6.03 MΩ which is much higher than the saline water resistance ~ 71.8 kΩ (Figure 6.15 (e)) and the inset). Owing to the removal of salts, the desalination yield water instigates the high resistance. To verify

the stability, few parts of a hybrid membrane are stored in different pH condition for a longer period (Figure 6.15 (f-g)). Eventually, no visible change is observed in pH 1, 7 even after 3 months whereas it degrades in alkaline condition within 3 weeks. Finally, we compare figure 6.15(h) the performance of our hybrid membrane with several other membranes. After careful evaluation it is found that the M/ Sb_2Se_3 hybrid membrane shows one of the high performing materials so far for solar desalination.

6.4. Conclusions

A cost-effective and environmentally friendly solar water evaporator material, Sb_2Se_3 NRs, was synthesized using a straightforward solvothermal approach. The effectiveness of light to heat conversion is demonstrated by unique water droplet experiment which offers a conversion efficiency ~58%. Following this, a desalination experiment is established by designing Sb_2Se_3 NRs loaded PVDF membrane via vacuum assisted process which shows commendable mass loss ~ 1.72 kg m^{-2} h^{-1}. Most importantly, a simple, cost-effective and scalable method of imprinting macro-channel over the hybrid membrane presents a unique approach to elevate the desalination performance of the hybrid membrane. The mass evaporation rate of Sb_2Se_3 attains 2.37 kg m^{-2} h^{-1}, accompanied by an efficiency of 148% when subjected to a mercury vapor lamp with an intensity of 1000 W m^{-2}. In actual sunlight conditions, it consistently sustains a commendable efficiency level of 108% under an irradiance of 950 W m^{-2}. Elevating the mass of Sb_2Se_3 as an absorber leads to a heightened evaporation rate, particularly in conditions characterized by a high degree of salinity. The substantial sustainability demonstrated across various pH

levels establishes Sb_2Se_3 as a promising material in the realm of light-to-heat conversion. The steam produced in the solar thermal heat generation process effectively eliminates heavy metal ions, adhering to the health standards set by the World Health Organization (WHO) for potable water. This work introduces Sb_2Se_3 as a new photothermal material and achieves high-performance solar-steam generation through a simple macro channel strategy, aiming to exploit it for seawater desalination and wastewater purification.

References

1. M. Gao, L. Zhu, C. K. Peh, G. W. Ho, Energy Environ. Sci., 2019, **12(3)**, 841-864.
2. D. H. Seo, S. Pineda, Y. C. Woo, M. Xie, A. T. Murdock, E. Y. Ang, & K. K. Ostrikov, Nat. commun., 2018, ***9*(1)**, 683.
3. M. Elimelech, W. A. Phillip, Science, 2011, ***333*(6043)**, 712-717.
4. L. Zhou, Y. Tan, J. Wang, W. Xu, Y. Yuan, W. Cai, Z. Shining, J. Zhu, Nat. Photonics**,** 2016, ***10*(6)**, 393-398.
5. C. M, A. Yadav, Renew. Sustain. Energy Rev., 2017, **67**, 1308-1330.
6. A. Kaushal, Varun, Renew. sustain. Energy Rev., 2010, ***14*(1)**, 446-453.
7. A. E. Kabeel, S. A. El-Agouz, Desalination, 2011, ***276*(1-3)**, 1-12.
8. O. Neumann, A. S. Urban, J. Day, S. Lal, P. Nordlander, N. J. Halas, ACS Nano, 2013, ***7*(1)**, 42-49.
9. D. Zhao, H. Duan, S. Yu, Y. Zhang, J. He, X. Quan, T. Deng, Sci. Rep., 2015, ***5*(1)**, 17276.

10. G. Ni, N. Miljkovic, H. Ghasemi, X. Huang, S. V. Boriskina, C. T. Lin, & G. Chen, Nano Energy, 2015, ***17***, 290-301.

11. Y. Wang, J. Nie, Z. He, Y. Zhi, X. Ma, P. Zhong, ACS Appl. Mater. Interfaces 2022, ***14*****(4)**, 5876-5886.

12. L. Ying, H. Zhu, H. Huang, X. Qu, C. Wang, X. Wang, F. Duan, S. Lu, M. Du, ACS Appl. Energy Mater., 2021, ***4*****(4)**, 3563-3572.

13. W. Li, X. Tian, X. Li, S. Han, C. Li, X. Z. Zhai, Y. Kang, Z. Z. Yu, J. Mater. Chem. A, 2021, ***9*****(26)**, 14859-14867.

14. L. Wang, J. Shang, G. Yang, Y. Ma, L. Kou, D. Liu, W. Lei, Small 2022, ***18*****(28)**, 2201770.

15. P. Wang, *Environ. Sci. Nano* 2018, ***5*****(5)**, 1078-1089.

16. G. Liu, J. Xu, K. Wang, Nano Energy, 2017,**41**, 269-284.

17. L. Zhu, M. Gao, C. K. N. Peh, G. W. Ho, *Mater. Horiz.* 2018, ***5*****(3)**, 323-343.

18. Z. Deng, J. Zhou, L. Miao, C. Liu, Y. Peng, L. Sun, S. Tanemura, *J. Mater. Chem. A* 2017, ***5*****(17)**, 7691-7709.

19. Z. Liu, H. Song, D. Ji, C. Li, A. Cheney, Y. Liu,.. & Q. Gan, *Global Challenges* 2017, ***1*****(2)**, 1600003.

20. X. Li, W. Xu, M. Tang, L. Zhou, B. Zhu, S. Zhu, J. Zhu, *Proc. the Natl. Acad. Sci.* 2016, ***113*****(49)**, 13953-13958.

21. M. Zhu, Y. Li, G. Chen, F. Jiang, Z. Yang, X. Luo,.. & L. Hu, *Adv. Mater.* 2017, ***29*****(44)**, 1704107.

22. W. Xu, X. Hu, S. Zhuang, Y. Wang, X. Li, L. Zhou, S. Zhu, J. Zhu, *Adv. Energy Mater.* 2018, ***8*****(14)**, 1702884.

23. T. Murakami, H. Nakatsuji, M. Inada, Y. Matoba, T. Umeyama, M.Tsujimoto, S. Isoda M. Hashida H. Imahori, *J. Am. Chem. Soc.* 2012, ***134*(43)**, 17862-17865.

24. M. L. Brongersma, N. J. Halas, P. Nordlander, *Nat. Nanotechnol.* 2015, ***10*(1)**, 25-34.

25. T., Liu, Y. Li, *Nat. Photonics* 2016, ***10*(6)**, 361-362.

26. M. Gao, P. K. N. Connor, G. W. Ho, *Energy Environ. Sci.* 2016, ***9*(10)**, 3151-3160.

27. D. P. Almond, P. Patel, Springer Science & Business Media. 1996**, 10**.

28. J. Wang, Y. Li, L. Deng, N. Wei, Y. Weng, S.Dong, T. Wu, *Adv. Mater.* 2017, ***29*(3)**, 1603730.

29. G. Zhu, J. Xu, W. Zhao, F. Huang, *ACS Appl. Mater. Interfaces,* 2016, ***8*(46)**, 31716-31721.

30. H. He, Z. Song, Y. Lan, M.Huang, S. Wu, C. Ben, Y. Zhang, ACS Appl. Mater. Interfaces, 2023, ***15*(14)**, 17947-17956.

31. L. Zhang, B. Tang, J. Wu, R. Li, P. Wang, Adv. Mater. 2015, **27**, 4889-4894.

32. D. Hao, Y. Yang, B. Xu, Z. Cai, *Appl. Therm. Eng.* 2018, **141**, 406-412.

33. Q. Jiang, H. G. Derami, D. Ghim, S. Cao, Y. S. Jun, S. Singamaneni, *J. Mater. Chem. A,* 2017, ***5*(35)**, 18397-18402.

34. Q. Chen, Z. Pei, Y. Xu, Z. Li, Y. Yang, Y. Wei, Y. Ji, *Chem. Sci.* 2018, ***9*(3)**, 623-628.

35. F. Zhao, X. Zhou, Y. Shi, X. Qian, M. Alexander, X. Zhao,.. & G. Yu, *Nat. Nanotechnol.* 2018, ***13*(6)**, 489-495.

36. X. Li, R. Lin, G., G.Ni, N. Xu, X. Hu, B. Zhu,... & J. Zhu, *Nat. Sci. Rev.* 2018 ,***5*(1)**, 70-77.

37. Y. Liu, S. Yu, R.Feng, A. Bernard, Y. Liu, Y. Zhang,... & T. Deng, *Adv. Mater.* 2015, ***27*(17)**, 2768-2774.

38. H. Ghasemi, G. Ni, A. M. Marconnet, J. Loomis, S. Yerci, N. Miljkovic, G. Chen, *Nat. commun*. 2014, ***5*(1)**, 4449.

39. Y. Yang, X. Yang, L. Fu, M. Zou, A. Cao, Y. Du, Q. Yuan, C. H. Yan, *ACS Energy Lett.* 2018, ***3*(5)**, 1165-1171.

40. N. Sen, N. Chakraborty, B. Das, K. K. Chattopadhyay, *Nanoscale* 2023, ***15*(48)**, 19671-19680.

41. Y. Zhou, M. Leng, Z. Xia, J. Zhong, H. Song, X. Liu, & J. Tang, *Adv. Energy Mater.* 2014, ***4*(8)**, 1301846.

42. T. Y. Ko, M. Shellaiah, K. W. Sun, *Sci. Rep.* 2016, ***6*(1)**, 35086.

43. Y. Ma, Z. Deng, H. Liang, X. Guan, Z. Zheng, J. Yao, G. Yang, *Laser & Photonics Reviews* 2024, 2400669.

44. G. Chen, J. Zhou, J.Zuo, Q. Yang, *ACS Applied Materials & Interfaces* 2016 ***8*(4)**, 2819-2825.

45. Y. Zhou, W. Feng, X. Qian, L. Yu, X. Han, G. Fan, J. Zhu, *ACS applied materials & interfaces* 2019**, *11*(22)**, 19712-19723.

46. N. Sen, A. Das, S. Maity, S. Ghosh, M. Samanta, K. K. Chattopadhyay, *ACS Appl. Energy Mater.* 2022,***6*(1)**, 58-67.

47. S.J. Clark, M.D. Segall, C.J.Pickard, P.J. Hasnip, M.I.Probert, K. Refson, M.C. Payne, Crystalline Materials 2005, **220(5-6)**, 567-570.

48. M.D. Segall, P.J. Lindan, M.A. Probert, C.J. Pickard, P.J. Hasnip, S.J. Clark M.C. Payne, J. phys. Condens. Matter. 2002, **14(11)**, 2717.

49. A.D. Becke, J. Chem. Phys. 2014, **140(18)**, 18A301.

50. J.P. Perdew, K. Burke, M. Ernzerhof, Phys. Rev. Lett. 1996, **77(18)**, 3865.

51. A.H. MacDonald, W.E. Picket, D.D. Koelling, J. Phys. C: Solid State Phys. 1980,**13(14)**, 2675.

52. G. Kresse, J. Hafner, Phys. Rev. B 1993, **47**, 558−561.

53. G. Kresse, J. Hafner, Phys. Rev. B 1994, **49**, 14251−14269.

54. G. Kresse, J. Furthmuller, Mater. Sci. 1996, **6**, 15–50.

55. P.E. Blochi, Phys. Rev. B 1994**, 50**, 17953.

56. J.P. Perdew, K. Burke, M. Ernzerhof, Phys. Rev. Lett. 1996, **77**, 3865.

57. S. Grimme, J. Antony, S. Ehrlich, H. Krieg, J. chem. Phys. 2010**, 132**, (15).

58. P. Vidal-fuentes, M. Guc, X. Alcobe, T. Jawhari, M. Placidi, 2D Mater. 2019, **6**, 045054-045066

59. P. P. Kong, F. Sun, L. Y. Xing, J. Zhu, S. J. Zhang, W. M. Li, Q. Q. Liu, X. C. Wang, S. M. Feng, X. H. Yu, J. L. Zhu, R. C. Yu, W. G. Yang, G. Y. Shen, Y. S. Zhao, R. Ahuja, H. K. Mao, C. Q. Jin, Sci. Rep. 2014, **4**, 6679-6703.

60. J. Tao, X. Hu, J. Xue, Y. Wang, G. Weng, S. Chen, Z. Zhu, J. Chu, Sol. Energy Mater. Sol. Cells 2019, **197**, 1-6.

61. A. Shongalova, M. R. Correia, B. Vermang, J. M. V. Cunha, P. M. P. Salome, P. A. Fernandes, MRS Commun. 2018, **8**, 865-870

62. N. Fleck, T. D. C. Hobson, C. N. Savory, J. Buckeridge, T. D. Veal, M. R. Correia, D. O. Scanlon, K. Durose, F. Jäckel, J. Mater. Chem. A 2020, **8**, 8337-8344.

63. G. Tse, Int. J. Mod. Phys. B 2023, **37(23)**, p.2350223.

64. A.M. Glazer, VIBRATE! J. Appl. Crystallogr. 2009, **42(6)**, 1194-1196.

65. S. Bhattacharjee, A. Banerjee, K.K. Chattopadhyay, J. Phys. Condens. Matter. 2024, **36(26)**, 265701.

66. R. Li, L. Zhang, L. Shi, P. Wang, *ACS Nano*, 2017, ***11*(4)**, 3752-3759.

67. A. J. Nozik, *Annu. Rev. Phys. Chem.* 2001, ***52*(1)**, 193-231.

68. Q. Wang, Q. Guo, F. Jia, Y. Li, S. Song, *ACS Appl. Mater. Interfaces* 2020,***12*(29)**, 32673-32680.

69. H. Fan, A. Gao, G. Zhang, S. Zhao, J. Cui, Y. Yan, *Chem. Eng. J.* 2021, **415**, 128798.

70. D. Ghim, Q. Jiang, S. Cao, S. Singamaneni, Y. S. Jun, *Nano Energy*, 2018, **53**, 949-957.

71. W. Xu, X. Hu, S. Zhuang, Y. Wang, X. Li, L. Zhou, J. Zhu, *Adv. Energy Mater.* 2018, ***8*(14)**, 1702884.

72. C. Liu, P. Wu, RSC *Adv.* 2024,***14*(15)**, 10370-10377.

73. T. Gao, Y. Li, C. Chen, Z. Yang, Y. Kuang, C. Jia, L. Hu, *Small Methods*, 2019, ***3*(2)**, 1800176.

74. B. Zhang, Q. Gu, C. Wang, Q. Gao, J. Guo, P. W. Wong, A. K. An, ACS *Appl Mater. Interfaces*, 2021, ***13*(3)**, 3762-3770.

75. W. Li, X. Tian, X. Li, J. Liu, C. Li, X. Feng, C. Shu, and Z-Z Yu, *J. Colloid Interface Sci.* 2022, **606**, 748-757.

76. X.Wu, T. Gao, C. Han, J. Xu, G. Owens, and H. Xu, *Sci. Bul.,* 2019,**64**, 1625-1633.

Chapter 7 Conclusions

This chapter serves as a comprehensive conclusion to all the work presented, marking the culmination of this dissertation.

7.Grand conclusions and future scopes

Research fields such as renewable energy, electronics and semiconductors, healthcare and medicine, aerospace etc. needs materials with desired attributes and functionalities. With high surface to volume ratio, quantum confinement effects, enhanced mechanical properties and tunable band gaps materials at the lower dimensions are superior to their bulk counterpart. However, nanomaterials with broad applicability remain challenging to develop and implement. This thesis focuses on the application of Sb_2Se_3 nanomaterials in three different specific fields. Prior to this work, literature survey indicated that Sb_2Se_3 materials were mainly used for solar cell research and to some extent in photodetectors and photoelectrochemical systems. However, the potential of Sb_2Se_3 nanostructures in electrocatalysis, desalination and SSPM has been largely overlooked. For HER we successfully synthesized an Sb_2Se_3/rGO hybrid using a one-step solvothermal approach and demonstrated its effectiveness as a hydrogen evolution electrocatalyst. Sb_2Se_3 nanorods were formed simultaneously with the reduction of GO, creating an interconnected conductive rGO network and generating numerous heterointerfaces between the two materials. The hybrid exhibited a significantly reduced onset potential of -0.32 V and a lower Tafel slope of 109 mV/dec compared to pristine samples in acidic media.

The formation of heterointerfaces in the hybrid enhances catalytically active sites and decreases the charge transfer resistance. Theoretical investigations revealed a notable reduction in the Gibbs free energy for H+ adsorption on the active (001) and (230) planes, attributed to diminished coulombic repulsion. The rGO facilitates

charge redistribution at the Sb_2Se_3/rGO heterointerfaces, enhancing H+ adsorption on the Se sites by reducing charges at these locations.

This synergy between theoretical and experimental results underscores the role of heterointerface formation in significantly improving the electrocatalytic HER performance of Sb_2Se_3 nanorods. Consequently, this study highlights the potential of Sb_2Se_3 and other chalcogenide-based heterointerfaces for the development of advanced, site-selective HER catalysts. In desalination Sb_2Se_3 material's light-to-heat conversion efficiency was demonstrated through a unique water droplet experiment, achieving a conversion efficiency of approximately 58%. Building on this, desalination experiments were conducted by fabricating a PVDF membrane loaded with Sb_2Se_3 NRs using a vacuum-assisted process, resulting in a mass loss of ~1.72 kg m^{-2} h^{-1}.

A notable advancement was achieved by imprinting macro-channels on the hybrid membrane, employing a straightforward, cost-effective and scalable method to significantly enhance its desalination performance. The Sb_2Se_3 membrane achieved an evaporation rate of 2.37 kg m^{-2} h^{-1} and an efficiency of 148% under a mercury vapor lamp at 1000 W m^{-2}. Under natural sunlight with an irradiance of 950 W m^{-2}, it maintained an impressive efficiency of 108%. Increasing the mass of Sb_2Se_3 as a light absorber further improved the evaporation rate, especially in high-salinity conditions.

The material demonstrated remarkable sustainability across a wide range of pH levels, making it a promising candidate for light-to-heat conversion applications. Steam generated through the solar thermal process effectively removed heavy metal

ions, meeting the World Health Organization's (WHO) standards for potable water. This study introduces Sb_2Se_3 as an innovative photothermal material and showcases high-performance solar steam generation through a macro-channel strategy, positioning it as a viable solution for seawater desalination and wastewater purification. Sb_2Se_3 nanorods (NRs) have been shown to exhibit a narrow bandgap, enabling strong nonlinear optical responses, particularly a high nonlinear refractive index (n_2) and third-order nonlinear susceptibility $\chi(3)$, as observed using the SSPM technique. The intense interaction between laser light (λ=671 nm, 532 nm, 405 nm) and Sb_2Se_3 NRs generates distinct diffraction ring patterns in the far field. These nonlinear optical properties are strongly influenced by the laser wavelength, the concentration of nanorods and the effective optical path length.

The formation of these diffraction rings was analysed using the 'Wind-Chime' model, while thermal convection through suspended nanorods explained the distortion of the rings. Leveraging the strong optical Kerr effect and reverse saturation absorption properties of Sb_2Se_3 and SnS_2, we successfully demonstrated an all-optical diode for laser sources at 671 and 532 nm. Additionally, a novel all-optical logic function, the OR logic gate, was achieved using SPM, where weak light was modulated by the presence of strong light due to the pronounced nonlinear response of Sb_2Se_3 NRs.

This exploration of the nonlinear optical properties of Sb_2Se_3 NRs, along with the demonstration of all-optical diodes and logic gate applications, represents a significant step toward the development of advanced devices for all-optical signal processing in future technologies.

Future Scope of research:

Potential for Sb_2Se_3 nanostructures as a multifunctional material for diverse area of applications seems huge and remains mostly unexplored. Also modifying the electrical and electronic properties of Sb_2Se_3 for the areas of applications that we have studied are not done. Some of the areas of future research are following:

- Exploring doping possibilities of Sb_2Se_3 to alter its electronic and electrical properties for enhancing its catalytic performance
- Fabrication of quantum dots of Sb_2Se_3 and explore its utilizations in the areas of electrocatalysis, desalination etc.
- Formation of heterointerfaces with other 2D materials and study of their performances for the areas like electrocatalysis, nonlinear optics and desalination